Magnetic nanostructures for advanced technologies: fabrication, metrology and challenges

2011 J. Phys. D: Appl. Phys. 44 303001

(http://iopscience.iop.org/0022-3727/44/30/303001)

IOP PUBLISHING JOURNAL OF PHYSICS D: APPLIED PHYSICS

J. Phys. D: Appl. Phys. **44** (2011) 303001 (43pp) doi:10.1088/0022-3727/44/30/303001

TOPICAL REVIEW

Magnetic nanostructures for advanced technologies: fabrication, metrology and challenges

June W Lau[1] **and Justin M Shaw**[2]

[1] National Institute of Standards and Technology, Gaithersburg, MD 20899, USA
[2] National Institute of Standards and Technology, Boulder, CO 80305, USA

E-mail: june.lau@nist.gov

Received 14 March 2011, in final form 18 May 2011
Published 7 July 2011
Online at stacks.iop.org/JPhysD/44/303001

Abstract
Magnetic nanostructures are an integral part to many state-of-the-art and emerging technologies. However, the complete path from parts (the nanostructures) to the manufacturing of the end products is not always obvious to students of magnetism. The paper follows this path of the magnetic nanostructure, and explains some of the steps along the way: What are the technologies that employ magnetic nanostructures? How are these nanostructures made? What is the physics behind the functional parts? How are the magnetic properties measured? Finally, we present, in our view, a list of challenges hindering progress in these technologies.

(Some figures in this article are in colour only in the electronic version)

Commonly used symbols and acronyms

E_b	energy barrier
f_0	attempt or precession frequency
$h, \hbar$	Planck constant
H, $H_{c,\mathrm{eff},K}$	magnetic field; coercive, effective, anisotropy field
I_c	critical current
k_B	Boltzmann constant
K, $K_{\mathrm{eff,u}}$	anisotropy; effective, uniaxial anisotropy
M, M_s	magnetization, saturation magnetization
T_c	Curie temperature
V	volume
α	Gilbert damping constant
μ_B	Bohr magneton
μ_0	permeability of free space
BPM	bit-pattern media
CPP	current perpendicular to film plane
EBL	electron beam lithography
FMR	ferromagnetic resonance
HDD	hard disk drive
LLG	Landau–Lifshitz–Gilbert
MOKE	magneto-optic Kerr effect
A, G, T MR	anisotropic, giant, tunnelling magnetoresistance
MTJ	magnetic tunnel junction
D, M RAM	dynamic,magnetoresistive random access memory
SFD	switching field distribution
SNR	signal-to-noise ratio
STT	spin-transfer torque
SW	Stoner–Wohlfarth

1. Magnetic nanostructures: established and emerging technologies, and implications of 'nano'

In order to be concise, we specify 'magnetic nanostructures' as individually arranged, sub-100 nm structures throughout this work. In section 1, we give an overview of the relationship between magnetic nanostructures and the technologies at stake, and the implications behind 'nano' as opposed to bulk or film. In section 2, we discuss the fabrication of magnetic nanostructures. In sections 3 and 4, we present static and dynamic measurement methods, respectively. In section 5, different magnetization reversal mechanisms are discussed within the context of micromagnetics and in section 6, we discuss the on-going challenges.

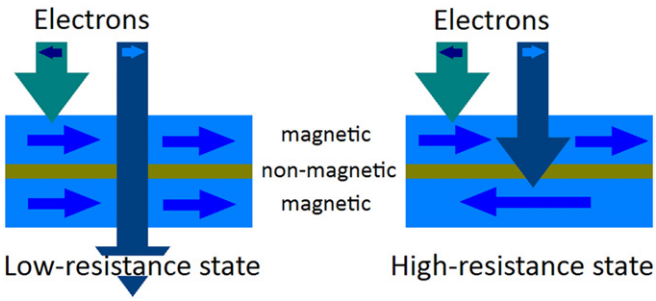

Figure 1. Schematic representation of the TMR effect. When the magnetic layers are magnetically parallel, a portion of the current with spin aligned with the magnetic layers experiences relatively little scattering. This is equivalent to the low-resistance state. When the magnetic layers are magnetized antiparallel to each other, no portion of the current may pass through the stack without significant scattering, which is equivalent to a high-resistance state. In a MTJ, the non-magnetic layer is made of an insulator.

1.1. Relevant technologies

We begin with an overview of the technologies that rely heavily on magnetic nanostructures today. However, in order to appreciate how some of them work, it is important to briefly review the concept of magnetoresistance (MR).

1.1.1. Review of MR. A change in the electrical resistance in ferromagnetic metals when magnetized was observed in 1856 by Lord Kelvin [1]. This MR was anisotropic (AMR), and depended on the angle between the magnetization in the ferromagnetic material and the current flow direction [2]. MR in the modern sense, where the resistance across a multilayer ferromagnetic junction depends on whether the ferromagnetic layers are magnetized parallel or antiparallel to each other, was first observed in 1988 [3, 4]. The two variations on this theme are giant magnetoresistance (GMR) and tunnelling magnetoresistance (TMR). The basic idea behind GMR and TMR are similar: one of the ferromagnetic electrodes has a fixed magnetization and can act as a spin filter. The other ferromagnetic electrode has magnetization that is free to rotate in response to a magnetic field. If the two electrodes are magnetized in parallel, the spin channels are aligned and an easy flow of electrons is enabled, and this is observed as the low-resistance state. If, however, the two electrodes are magnetized antiparallel, the majority spin channel is obstructed, and the flow of electrons becomes more resistive. Figure 1 illustrates the MR principle in magnetic tunnel junctions (MTJs).

Numerically, MR is defined as $(R_{AP} - R_P)/R_P$, where R_{AP} and R_P are the resistance values of the antiparallel and parallel state, respectively. $Ni_{80}Fe_{20}$ (Permalloy), which has very high AMR (which is no more than a few per cent at room temperature), has been used for AMR devices. For GMR, the two ferromagnetic layers are separated by a non-magnetic metal such as Cu, in a configuration called spin-valve. Typical GMR values achieved at room temperature with one spin-valve is about 8% to 10%; however, GMR values up to 21% have been demonstrated [5]. For TMR devices, however, the two ferromagnetic electrodes are separated instead by a thin insulator, typically Al_2O_3 or MgO, in a configuration called MTJ. Here, a MgO tunnel barrier can act as an additional spin filter [6] and because the electrons must tunnel through the insulator, TMR values of over 1000% have been demonstrated [7]. While devices based on TMR have higher signal-to-noise ratios (SNRs), spin-valve devices based on GMR have faster responses because, unlike the MTJ, which is effectively a capacitor, the all-metal GMR stack can have much higher data rates due to the lack of an R–C time constant. In the sections to follow, several technologies dependent on MR will be discussed.

Slonczewski and Berger independently proposed in 1996 that if the current passing through the fixed magnetic layer is large enough, a spin-polarized current exiting the fixed layer can transfer enough momentum to rotate the magnetization in the free layer [8, 9]. In other words, a pulse of spin-polarized current through the device can be used to switch the magnetic state of the device without the use of external magnetic fields. This prediction has since been independently verified [10] and is the focus of intense research.

1.1.2. Hard disk drives. The hard disk drive (HDD) in today's computers uses GMR/TMR to read, a strong magnetic field to write and a spinning disk coated with perpendicularly magnetized material to store the data. While solid-state drives are gaining popularity as a mobile storage platform, the HDD is still the more competitive product in bytes per unit cost. This is because the HDD is a mature technology that has enjoyed several decades of improvements in areal density. At present, the highest areal density achievable in a laboratory setting is likely to be around $1.4\,\mathrm{Pb\,m^{-2}}$ ($900\,\mathrm{Gb\,inch^{-2}}$), with the most recent public announcement of $1.24\,\mathrm{Pb\,m^{-2}}$ ($803\,\mathrm{Gb\,inch^{-2}}$) in October of 2008 [11]. Areal densities have improved about 40% every year since 1957 [12]. Even so, without some major innovation, it would be difficult to continue this trajectory of growth based on down-scaling of the heads and bits alone. Some contenders to go significantly beyond $1.55\,\mathrm{Pb\,m^{-2}}$ ($1\,\mathrm{Tb\,inch^{-2}}$) include energy-assisted recording, TDMR or 'shingle writing' and bit-pattern media (BPM). Magnetic nanostructures are essential components of the modern HDD. In this section, we consider the roles of these nanostructures, first in the read and write heads, then in the recording media.

Recording heads. Before 1991, reading and writing operations were performed by the same head, which consisted of a ferrite pole or thin film, wound up in coils of wire. After 1991, a series of MR-based read heads came into the marketplace, starting with AMR, GMR and finally TMR heads in 1991, 1998 and 2003, respectively. As the head (which consists of either a spin-valve or a MTJ stack) glides over a recorded bit on the platter, it senses the magnetization direction of the bit from its stray field. The stray field rotates the free layer within the stack, and this rotation is registered by a sense current as a change in MR. So for instance, if the read sensor detects a low or high resistance, corresponding to a parallel or antiparallel alignment of the ferromagnetic electrode, it can infer from the MR measurement whether a magnetic transition has occurred. The presence or absence of a magnetic transition then translates to the state of the bit.

The direction of current flow with respect to the plane of the junction is designated either as CIP or CPP for current applied in the plane of, or perpendicular to, the substrate, respectively. A GMR head with sense current flowing perpendicular to the spin-valve spacer is therefore called CPP-GMR. Most HDDs today ship with a TMR read head, but there is momentum to migrate back to CPP-GMR (and in particular, all-metal CPP-GMR) with improved materials and engineering designs suitable for higher data rates. The reason is that the best MTJ has a resistance–area product ($RA = 1\,\Omega\,\mu\text{m}^2$) that is two orders of magnitude higher than the RA for the typical spin-valves ($\sim 0.05\,\Omega\,\mu\text{m}^2$), and this RA puts a hard limit on data transfer rates and SNR that will soon be insufficient to accommodate the concurrent growth in areal density. Today a typical desktop HDD can achieve gigahertz data transfer rates.

Data are written by the write pole, which is a strong electromagnet producing magnetic fields of up to 2 T at the air bearing surface (ABS). The ABS puts a ~3 nm gap between the head and the media in current state-of-the-art HDDs. The write pole and small ABS provide a high magnetic field to a very localized region on the surface of the media. As such, data are written in the media as the head moves across the surface causing local regions (bits) to change their magnetic orientation.

Media. Data are written to, and stored on, spinning platters that are typically between 6 to 9 cm (2.5 to 3.5 inch) in diameter. The storage layer on the platters consists of a uniform layer of high-anisotropy, perpendicularly (with respect to the platter) magnetized material with grains on the order of 5 nm. In conventional media, bits have a nominally rectangular aspect ratio defined by the size of the recording head, and all of the grains within this rectangular region are ideally magnetized in the same direction. An important property of media is that the grains are exchange decoupled, that is, the grains are separated by a thin oxide layer that minimizes the interaction of neighbouring grains. This is necessary so that the grains can switch independently from their neighbours. Figure 2 shows a magnetic force micrograph of a track in longitudinally magnetized media where such rectangular bits were written into the media. In a HDD with areal density of 775 Tb m^{-2} (500 Gb inch^{-2}), the enclosed rectangle would have an area of 1225 nm^2 (or an area of 35 nm × 35 nm), and a bit aspect ratio (BAR) of about 4. The optimal BAR simultaneously maximizes areal density, SNR and thermal stability. Much is available in the literature on this subject.

HDDs made with strong perpendicular anisotropy material is an innovation that is less than 10 years old. Before 2003, the bits were magnetized in the plane of the platter. The reason for the switch from in-plane to perpendicular magnetic recording has to do with improving thermal stability while simultaneously reducing the volume of the bit (see discussion in section 6.1), which ultimately increases areal density. The areal density of HDD using perpendicular anisotropy material is expected to reach a limit at about 1.55 Pb m^{-2} (1 Tb inch^{-2}) due to the superparamagnetic effect (see section 6.1). Beyond this, the head and the media would require something different from what is being done today.

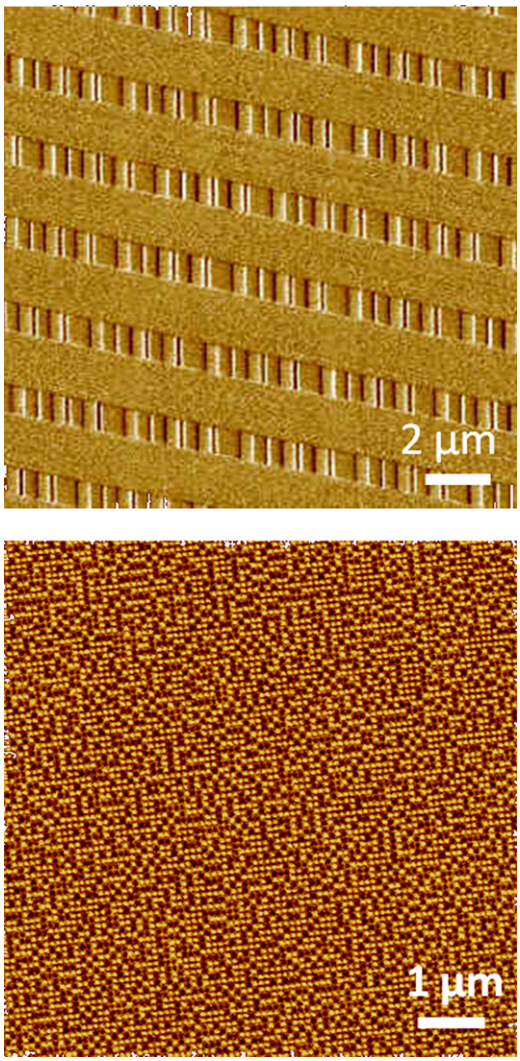

Figure 2. (Top) MFM image of track written in conventional media, and (bottom) 50 nm bits in BPM.

Beyond 1 Tb inch^{-2}. One technology being explored to overcome the superparamagnetic limit of conventional media is BPM. Here, instead of a continuous magnetic film consisting of exchange decoupled grains, BPM makes use of lithographically defined, well-separated nano-island bits made from exchange-*coupled* materials. Since the grains are exchange coupled and the bits are physically isolated, each island behaves like a Stoner–Wohlfarth (SW) volume, which is far more stable against thermal fluctuations. BPM have a significant increase in SW volume compared with conventional media, where the individual grains are independent SW volumes due to exchange decoupling. However, BPM will place great demands on lithography: to achieve an areal density of 1 Tb inch^{-2} using BPM, the islands will have to be patterned with a 25 nm pitch (centre-to-centre spacing) with a BAR of 1. Many challenges are associated with commercializing BPM: tight tolerances for switching field distribution (SFD) both intrinsic and extrinsic (section 6.2), time and cost of lithographically defining 10^{12} bits on every drive, and tribology problems associated with uneven surfaces created by the islands. However, a lot was learned in the last 10 years, such

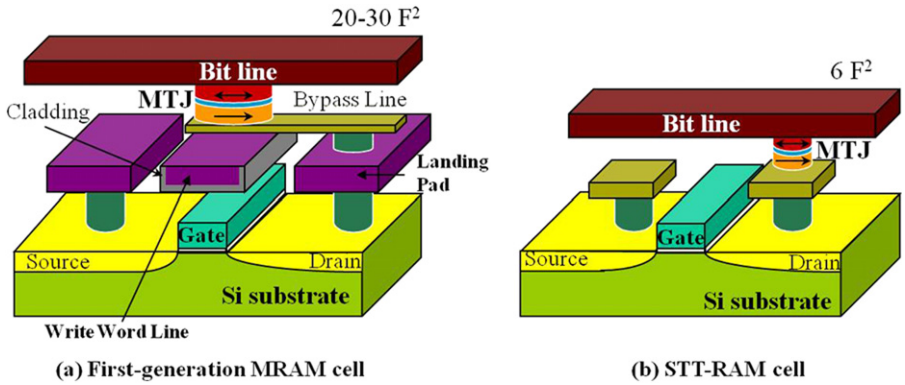

Figure 3. Schematic of (*a*) conventional MRAM and (*b*) spin transfer torque (STT)-RAM. In conventional MRAM, the MTJ free layer is switched by Oersted fields generated by the bit and word lines. In STT-RAM, the free layer is switched, instead, with a spin-polarized current. Note the simplicity in architecture for a STT-RAM cell in comparison with the structures that come with a single MRAM cell. Figure reprinted with permission from Grandis Inc.

that this technology may have enough momentum to move forwards. Another way to circumvent the superparamagnetic effect is to use very-high anisotropy material for the storage media. However, as we shall see in section 6.1, high-anisotropy material, though more thermally stable, is also more difficult to write. Several schemes may solve this problem. One, known as heat-assisted magnetic recording (HAMR) [13] involves mounting a highly focused laser beam on the write head to bring a small, selected region of the media close to the Curie temperature (T_c) during the write cycle. Another scheme, microwave assisted magnetic recording (MAMR), involves mounting a spin-torque oscillator (STO) on the write head in order to induce ferromagnetic resonance in the media during the write cycle [14, 15]. This idea of writing to a bit under non-equilibrium conditions is more generally known as energy-assisted recording.

The concept of two-dimensional magnetic recording (TDMR) [16], does not involve fabrication of nanostructures as in BPM, or operating under non-equilibrium conditions as in MAMR, but can potentially improve areal density beyond $1\,\mathrm{Tb\,inch^{-2}}$ and so it deserves brief mention. TDMR or 'shingle writing' involves writing bits that are staggered like shingles on a roof. In theory, the bit size can be one grain wide. The challenge is in devising efficient algorithms to reconstruct the orientations of previously written shingles.

Racetrack memory [17] has attracted some attention in recent years. In this concept, data are stored as domain wall patterns on U-shaped nano-wire tracks. Data are written by the application of spin-polarized current, which moves the domain walls along the wire. Every domain wall produces some stray field, which then can be read by MR sensors positioned along the U in the track. Racetrack memory is projected to have similar cost as HDDs; it can have faster access times, and can potentially have much larger storage densities than HDDs because data are stored in all three dimensions. This idea is still under development.

1.1.3. Magnetoresistive random access memory. Ever since the discovery of GMR and TMR, companies have tried to develop a non-volatile, magnetic memory chip based on MR. In comparison with conventional dynamic random access memory (DRAM) found in computers, MRAM is non-volatile in that it does not require steady power input for data retention, which means it has lower overall power consumption. Flash memory, on the other hand, although also non-volatile, uses relatively large programming voltages and current pulses to overwrite data, which cause the device to degrade over time. MRAM has virtually a limitless number of write cycles by comparison. The prospect of a MRAM universal memory in the not-too-distant future has been a major driving force behind its development. Figure 3(*a*) shows the basic architecture for the MRAM. Parallel bit lines and parallel word lines are laid down perpendicular to each other with one MTJ occupying each intersection. During the write cycle, current runs only through the lines that intersect the bit of interest. The Oersted fields generated by those lines are large enough to toggle the MTJ between the parallel and the antiparallel state, which registers as a difference in MR when it is measured with a much lower current during read-back.

Even though GMR was first discovered in 1988, a commercial MRAM product did not appear on the market for almost 20 years. The primary obstacle was the half-select problem due to the SFD among the bits. To appreciate this problem, imagine the 4 Mb memory, that is, 4 million bits on a chip. These bits have some average switching field H_{sf}, but because of small physical or material variations from processing or intrinsic variations, the switching fields are normally distributed with some width σ_s. To guarantee that each of these 4 million bits switch, a minimum applied field H_{min} greater than $6\sigma_s$ from H_{sf} is required. In principle, only the bit intersected by the two active lines is exposed to enough magnetic field for it to be overwritten. In practice, all elements under an active line experience magnetic field generated by that line. Therefore, all bits that reside on an active line, i.e. the neighbouring half-selected bits, can be unintentionally overwritten if they happen to have switching fields that are a couple of σ_s on the low side; that is 200 000 bits out of a 4 Mb chip! Thus, the maximum applied field H_{max} is defined by a narrow region where this field is small enough such that none of the half-selected bits switch, yet large enough to overcome the switching field on the selected bit.

A solution to the half-select problem came in 2006. Freescale Semiconductors (now Everspin) became the first company to mass manufacture a 4 Mb toggle-MRAM [18]. While the basic architecture is illustrated by figure 3(*a*), each of the single-layer ferromagnetic electrodes ('free' and 'pinned' layers) in the earlier design was replaced by a synthetic antiferromagnet (SAF) in the toggle-MRAM. A SAF consists of two antiferromagnetically coupled ferromagnetic layers separated by a Ru spacer layer. The antiferromagnetic exchange coupling between the two ferromagnetic layers can be tuned by the thickness of the Ru layer. The memory bit is elliptical in shape; its long (easy) axis is set at a 45° angle between the two write lines, which are orthogonal to each other. Focusing our discussion only on the SAF 'free layer', a pair of sequenced write pulses is sent through the two write lines to 'toggle' each layer within the SAF in steps. During the write sequence, the coordinated pulses guide the magnetization in both ferromagnetic layers of the SAF to rotate through the ellipses' hard axes, but always in such a way that they remain antiferromagnetically aligned for the most part. At the end of a write cycle, even though each of the ferromagnetic layers is magnetized oppositely to its initial direction, the net magnetization of the SAF has not changed. Because current from one write line alone is incapable of completing the successive sequence of toggles required to switch the free layer, the half-select problem is all but eliminated in this design.

Nonetheless, in order to accomplish the toggle, the toggle-MRAM requires a lot of area on the chip. The fact that it is relatively low-density and requires large input currents during the write cycle means that it would be very difficult to scale down this architecture. Hence, there is much motivation to find a simpler and more scalable platform. Conceptually, the STT RAM can solve both the energy efficiency and bit-density problem. It is illustrated in figure 3(*b*). Like the toggle-MRAM, the STT-RAM is also based on the MTJ. However, the free layer in STT-RAM is switched by spin-polarized current instead of Oersted fields. Clearly if a single current-carrying line can read and write a bit, this is a significant improvement over the toggle-MRAM from an energy and lithography point of view. If F is the feature size of the memory cell, the toggle-MRAM requires an area of $25F^2$ for all of the support structure for each cell, whereas the STT-RAM requires only $6F^2$. Despite the attractiveness of this concept, many outstanding problems exist (see section 6.3). Several successful lab demonstration of STT-RAM have been made [19–21]; a commercial product may be 2 to 3 years away.

1.1.4. Spin-torque oscillators. In addition to STT-RAM, the spin-torque effect in nanostructures can be exploited for a very different purpose: the generation of microwave fields and currents. Here, the torque exerted by the spin-polarized current is used to excite the magnetization in the magnetic free layer to precess at gigahertz frequencies. The power of this phenomenon is that a dc current can produce microwaves in a nanoscale spin-torque device. In addition, since the precession frequency is a function of the magnetic field applied to the device as well as the dc current, such devices are frequency-tunable.

The first reports of STOs were in nanopillar GMR devices, which produce picowatts to nanowatts of microwave power [22, 23]. The use of TMR devices was more recently shown to generate orders of magnitude higher microwave power, generating microwatts from a single 100 nm device [24]. However, these approaches suffer from rather broad linewidths, on the order of a gigahertz. As an alternative, STO nano-contacts have been reported to produce tens of megahertz linewidths in both in-plane [25] and out-of-plane anisotropic materials [26]. The overall power can be significantly increased by phase-locking several devices together [27].

One of the primary applications for STOs is in communications. Most communication technologies, such as mobile telephones, rely on microwave signal generation and sensing. STOs are many orders of magnitude smaller than conventional oscillators. Thus, STOs are an attractive alternative to embed microwave sources in electronic devices. STOs are also being explored as the microwave field source for MAMR technology [14]. Due to their small size and power consumption, such devices may be the microwave source on the write heads in MAMR technology. Finally, it was more recently suggested that STOs can be used for magnetic sensor applications that require dimensions or resolution below 30 nm. The high resolution is largely a result of the physical size of the STO and the sensitivity of the oscillation frequencies to external fields [28]. This latter idea is being explored as an alternative technology to be used in HDD read heads.

1.1.5. Spin logic. Spin logic is being explored as a replacement for complementary metal–oxide–semiconductor (CMOS) technology. But why does CMOS need replacement? The current trajectory for CMOS growth, based on Moore's law [29], will reach two fundamental limits: scaling (lithography and high-dielectric materials challenges) and heat removal. According to the International Technology Road map for Semiconductors (ITRS), significant challenges beyond the 22 nm node are anticipated beyond 2016 [30]. Additionally, if each transistor operation dissipates 2000 eV of energy [30], Bandyopadhyay and Cahay anticipate that by 2025, the power density on a computer processor will reach $2\,\mathrm{MW\,cm^{-2}}$, similar to that of a 'rocket nozzle' [31], which would be cost-ineffective to cool. Therefore, much of the language seen in the literature like 'post-CMOS' or 'beyond CMOS' refers to novel devices that can continue to scale according to Moore's law when CMOS reaches the scaling limit. Clearly, the same lithography and heat dissipation challenges must also be addressed when assessing a possible CMOS replacement.

In spin logic, the individual switches that perform the binary operations are made with magnetic nanostructures (e.g. MTJ, spin transistors), and the universal logic operators (e.g. AND, NOR, XOR) are either aggregates of a combination of switches, or a stand-alone structure (e.g. magnetic quantum cellular automata (MQCA) network, domain wall logic, etc). The four criteria laid out by Nikonov and Bourianoff [32] that define whether or not a particular spin-logic device is feasible for the post-CMOS world are scalability, cascadability, CMOS platform compatibility and sufficient SNR. Implicit in the last criterion is that the device should have some signal

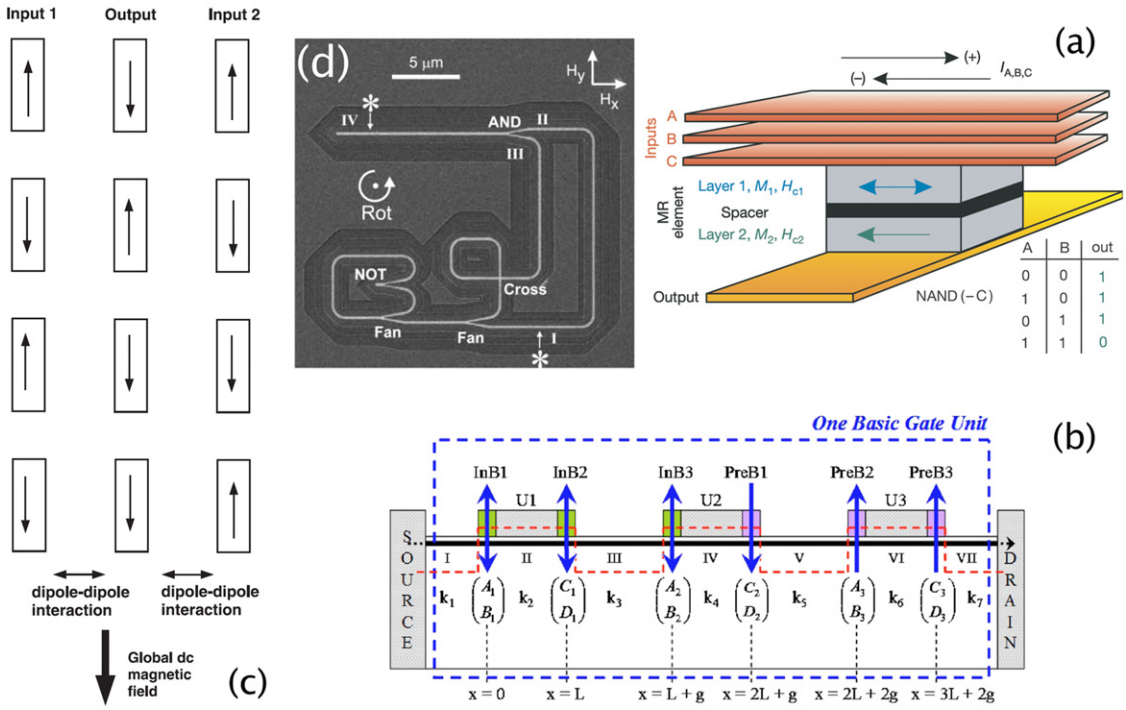

Figure 4. Several proposed ways to build a NAND gate using magnetic nanostructures. (*a*) MTJ with three-current input [35]. (Reprinted with permission from Macmillan Publishers Ltd (*Nature* [35]), copyright 2003.) (*b*) Spin-transistor [47]. (Reprinted with permission from [47], copyright 2008 by the American Institute of Physics.) (*c*) MQCA with global bias field [31]. (Reprinted with permission from Institute of Physics.) (*d*) Magnetic nano-wire AND and NOT gates connected in tandem (From [48], reprinted with permission from AAAS.). Although the output as shown is not a NAND gate, one can be made with the AND and NOT elements reconnected differently.

gain, otherwise energy dissipation will remain a problem. For brevity, we will not go into the relative merit of each of these technologies; however, thorough analysis of their challenges and limitations can be found in the references.

From the previous discussion on MRAM, it is not difficult to imagine that MTJs and spin-valves (particularly the STT variety) can also operate as switches. Indeed, various groups have showed that programmable MR-based spin logic is feasible [33–39]. Figure 4(*a*) is an example of an MTJ-based device, showing how a NAND gate can be programmed with three-current inputs [35]. Spin-based switches can also be made from the many transistor variants, but primarily, there are two families that are analogous to existing technologies: spin field-effect transistors (FETs) and spin bipolar tunnelling transistors (BJTs), both of which are CMOS compatible. Spin FETs control unipolar spin-filtered current flow via the gate bias voltage. The spin BJTs use ferromagnetic material as base. Magnetization in the base produces a difference in energy barrier for the carriers that are aligned either parallel or antiparallel to its field due to Zeeman splitting. Gain is theoretically possible in these devices. The different implementations are given in [40–44] for the spin FET, and [45, 46] for the spin BTJ. In both the spin FET and spin BJT, the logic state 0 or 1 is determined by current flow from one terminal of the device to another. Building a NAND gate, for example, would require a specific arrangement of spin transistors as shown in figure 4(*b*) [47]. However, spin transistor technology is still quite far from the production stage due to intrinsic challenges associated with spin injection and detection.

In the previous examples, the toggle between logic states 0 and 1 involves moving spin carriers and so they do not address the fundamental energy dissipation associated with moving charges around. Suppose an alternate logic scheme where each bit can occupy one of two degenerate energy minima such as a single-domain elliptical nanostructure, magnetized along the long axis. Cowburn and Welland first demonstrated that controlled switching of a linear chain of magnetic nanodots can be achieved by a combination of shape anisotropy and exchange coupling interaction [49]. Building a NAND structure, for example, would require a specific arrangement of single-domain exchange-coupled bits (figure 4(*c*)). In this scheme, a small bias field is always applied in the *down* direction. The two inputs are the elliptical dots at the ends and the output is the dot in the middle. If both inputs are magnetized *up*, exchange interaction forces the output dot to be *down*. Similarly, if both inputs are *down*, the output would be *up*. In the two cases where the two input dots are antiparallel to each other, the small bias field breaks the tie and produces an output of *down*. In general, particular logic operators are defined by a specific spatial arrangement of lithographically placed bits. An OR operation would have a different pattern of spatially arranged bits. The total energy of this system therefore consists of Zeeman energy (from the magnetized dots' interaction with the small external bias field) anisotropy energy (required for switching the inputs and outputs) and the energy required to read the output, which is method dependent. At an estimated 800 meV per operation, it is significantly more energy efficient than CMOS [31]. However, the central issue that is shared with down-scaling of magnetic nanostructure is the superparamagnetic effect and thermal stability.

It was demonstrated that universal gates can also be built from a network of soft magnetic nanowires [48]. Like the MQCA, a particular logic operation is pre-determined by the nano-wire template. Unlike the MQCA, it is the presence of domain walls that is essential for the function of nano-wire logic. Conceptually similar to a 'Rube Goldberg machine', the domain walls, once generated, can be propagated, multiplied and annihilated throughout the nano-wire network with an in-plane bias magnetic field. A base logic unit consists of a unique nano-wire pattern: these units can, in turn, be interconnected in specific ways to perform more complex operations. Figure 4(*d*) shows a NOT and AND gate in tandem. Although structurally not a NAND gate like the other examples, components of this network can be reconfigured for such an operation.

1.2. Measurement considerations

Suppose we have a magnetic film as represented in figure 5(*a*). The dots represent the location of unusual magnetic properties, as in a region of lower anisotropy due to a defect. If this film is patterned into micrometre-sized elements as shown in figure 5(*b*), each patterned element has four defect sites on average. If the magnetic properties of each element are measured, we can expect them to have similar properties. However, imagine instead of the micrometre-size elements, we patterned the original film down to nano-islands as shown in figure 5(*c*). It is not hard to see that some structures have defects centred on the island, others have defects sitting on the edge or corners, while others are defect-free. We would not expect the islands with centred defects to behave in the same way as islands with edge defects. Furthermore, edge defects introduced by patterning processes consist of a larger fraction of the nano-island volume than the micro-island volume. Certainly, one should expect there to be a difference in behaviour between islands that have defects and those that do not. Compared with the bulk, edges and defects are expected to play a larger role in magnetic properties as structures become smaller. For example, it was shown that edge roughness significantly alters the reversal field in sub-micrometre $Ni_{80}Fe_{20}$ structures [50, 51], and we would expect it to matter even more so in nanostructures. The role of intrinsic and extrinsic defects will be examined further in section 6.2.

Generally, if there is a random distribution of defects, one would expect the magnetic property of interest to vary, and those variations to fall within a distribution. The previous schematic helps illustrate that when nanostructures have dimensions commensurate with those of defects, the variations in magnetic properties will become more pronounced and that the distribution will widen. This phenomenon is a conundrum of magnetic nanostructures and it has been problematic for the development of technologies like BPM where tight switching tolerances are required. The quest to directly correlate physical defects with magnetic properties distribution is at present an active area of research [52–56].

Indeed, when considering a magnetic response like the coercive field, H_c, for example, one would expect not only that individual magnetic nano-islands behave differently, but also

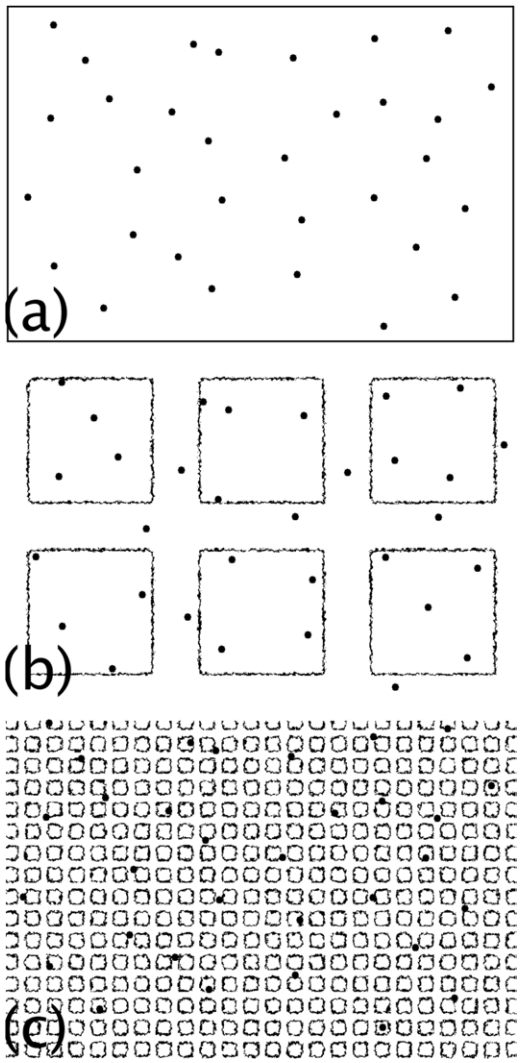

Figure 5. Schematic shows the relationship between intrinsic and extrinsic (represented by the black dots, and the edges, respectively) distribution of defects and the down-scaling of material. (*a*) Defects randomly distributed on a thin film. (*b*) Patterning down this film into isolated micrometre-sized blocks still preserves four intrinsic defects per block. (*c*) Further down-scaling into length scales similar to the defects demonstrate that the blocks are clearly very different from one another, particularly at the edges.

that the average H_c of islands of a certain size is very different from the average H_c of islands of another size. In their Co/Pd multilayer nano-island work, Thomson *et al* showed that not only does average H_c increase with decreasing island diameter, but the spread in H_c actually increases when island diameter decreases due to a distribution of defects.

Because of the need to pinpoint the origin of magnetic property distributions, it is becoming increasingly important to make measurements on individual nanostructures in addition to the traditional volume average measurement techniques (e.g. vibrating sample magnetometer (VSM), superconducting quantum interference device (SQUID)). Developing techniques to characterize nanostructures has become just as important as finding root causes of aberrant magnetic behaviour.

The continual miniaturization and density improvements of technology today is driving much of the development into

the deep nanometre scale. A natural consequence of this development is the impressive data transfer rates that we have come to expect. Not including ultra-fast precession switching, the magnetization reversal of a single-domain nanostructure is typically complete after a few nanoseconds, which would correspond to a data transfer rate of up to 1 GHz. However, magnetic properties differ very much between the GHz regime and the static regime, and certainly very different from the data storage time scale (10^9 s). Therefore, it is necessary to understand and to measure, where possible, switching physics through 18 orders of magnitude in time. Sharrock and KcKinney, for example, found that H_c of a ferromagnet can change by a factor of two depending on the reversal field application rate [57]. Using a thermal model, it was later understood that H_c is time and temperature dependent. Further discussion is given in section 5.1.

The thermal model generally breaks down on the 10^{-9} s scale because there is no longer adequate time for the system to have a significant probability of receiving a thermally assisted event. As a result, the reversal process is guided by spins directly responding and rotating to an external stimulus (e.g. an external field or a torque exerted by a spin-polarized current) in what is commonly called precessional switching. Switching on the 10^9 s scale, on the other hand, given fixed external influences are governed solely by thermal excitation, follows the Arrhenius–Néel law [58] and the mechanism is therefore one of barrier hopping based on number of attempts per unit time. The energy landscape of a given magnetic system often has more than one energy minimum, hence more than one energy barrier and therefore multiple competing processes to get across those barriers to a lower energy state. The energy landscape itself is a changing function of the external field. Switching on the intermediate time scales, where the energy of barriers is lowered sufficiently to allow thermally activated barrier crossings, has been known to produce stochastic results [59–61].

2. Fabrication

As we discussed in the previous section, when the dimensions of a magnetic structure are reduced to the nanometre regime, small variations in shape, size and edge properties become increasingly more influential on the magnetic properties. As a result, the method and process used to fabricate a nanostructure can significantly influence its magnetic properties. This behaviour is further complicated by the fact that nanostructures become increasingly more challenging to fabricate as their dimensions are reduced. There are many approaches to the fabrication of nanostructures; each with its advantage and disadvantage depending on the application. In this section, we provide a brief overview of many common approaches in order to provide a framework and context for many general challenges faced with metallic based magnetic nanostructures. For example, edge properties in many magnetic nanostructures can significantly alter the magnetic properties of the nanostructure and can even dominate the magnetic behaviour. Thus, considerable attention may be needed to minimize damage to the edge region during patterning. Several reviews of fabrication techniques can be found in [62–66], which provide more depth to the general concepts we cover in this section. However, our goal is to provide some extra attention to a handful of practical techniques that are of use in the research laboratory.

2.1. Deposition

Regardless of the fabrication technique used to achieve lateral confinement, the magnetic material must be created in a very controlled manner. For most applications in spintronics and recording technologies, the magnetic material is typically created via a physical vapour deposition (PVD) process, which include sputtering, evaporation, ion beam deposition (IBD) and molecular beam epitaxy (MBE). However, other methods such as atomic layer deposition (ALD), chemical vapour deposition (CVD) and electrochemical deposition can also be used. For many applications in the bio-sciences, chemical and electrochemical synthesis of magnetic nanoparticles are used.

When a material is patterned, any inhomogeneity or lateral variation of microstructure will lead to a distribution of magnetic properties from nanostructure to nanostructure. This is due to the fact that smaller features will contain a smaller sampling of the material, and thus, the magnetic properties are less averaged. As a result, optimization of deposition parameters becomes increasingly more important to achieve predictable magnetic behaviour of nanostructures.

2.2. Pattern transfer

Precise control of the layer thickness (out-of-plane dimension) is relatively straightforward to achieve through the various deposition techniques. In fact, MBE is routinely demonstrated to be able to control the thickness and growth on a monolayer by monolayer basis. Even in sputtered films, control of the layer coverage to below 0.1 nm is common as demonstrated in many multilayer samples. However, such control over the lateral dimensions of a nanostructure becomes significantly more difficult to achieve. A common point of distinction among fabrication approaches is whether the pattern transfer from a mask is performed via an additive method or a subtractive one.

2.2.1. Additive approach. An additive approach is typically referred to as a ‘lift-off’ process when a PVD deposition process is used to deposit the material. Here, a mask is initially formed on the substrate and the magnetic material is deposited everywhere on the surface. When the mask is removed, only the magnetic material deposited into the exposed ‘holes’ of the mask remains on the substrate surface. This process proves useful in fabricating simple or single-layer structures. A major limitation of lift-off processes resides in the fact that some amount of shadowing occurs at the edges of the structure. This is a result of the fact that the ‘holes’ in mask material have a finite aspect ratio and there is always a spread in the direction of the incident atoms as they approach the surface. As a result, some of the material deposited near the edges coats the sidewalls of the masking material, resulting in ‘fencing’ or can gradually taper off in

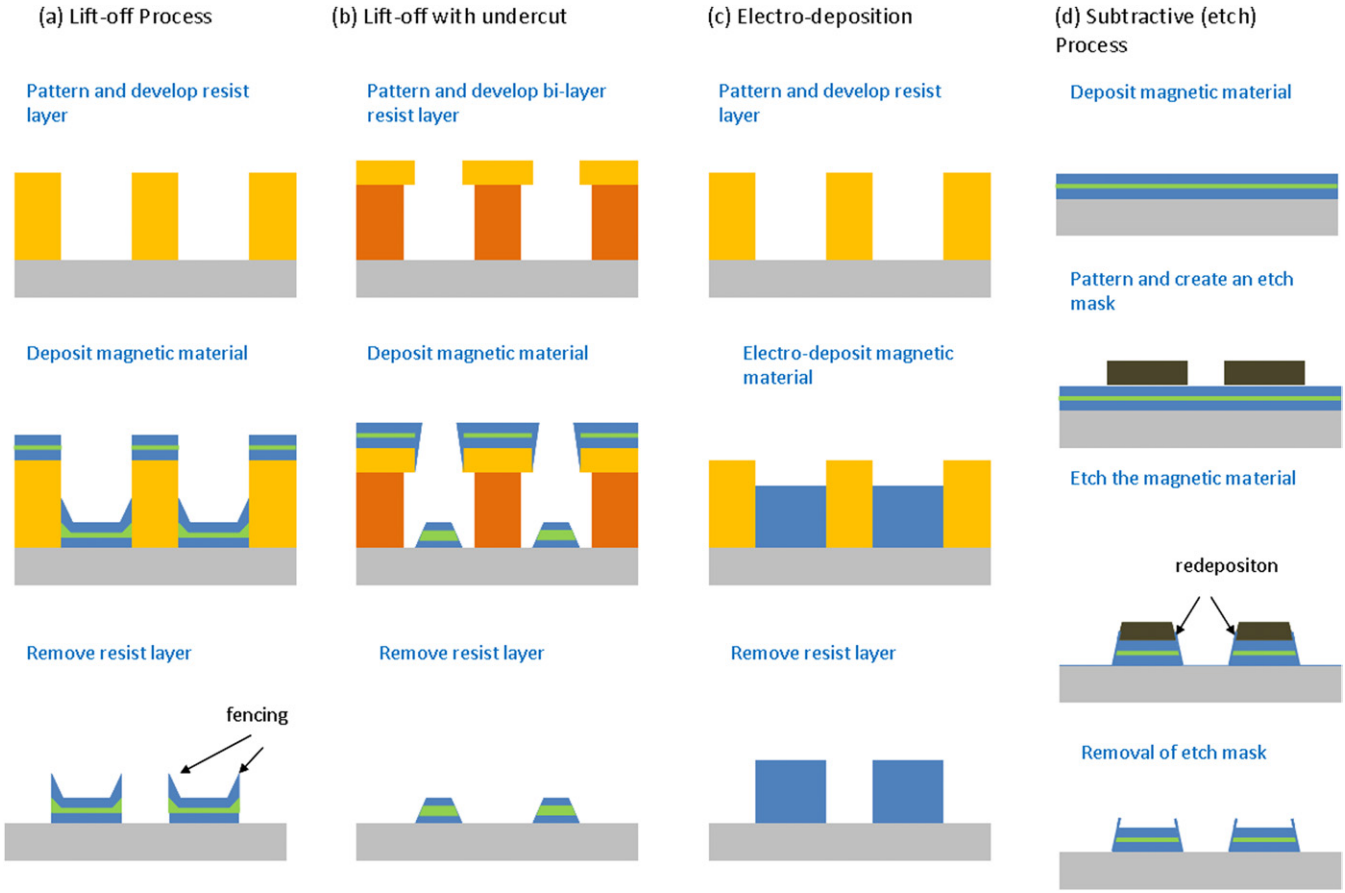

Figure 6. (*a*) Lift-off process, (*b*) Lift-off with undercut, (*c*) electro-deposition and (*d*) subtractive (etch) process.

thickness at the edges. Figure 6(*a*) shows a diagram of the lift-off process and how it can result in fencing at the edges. Such effects can lead to significant variation of the material thickness across the structure. Therefore, better results can generally be achieved with a deposition configuration that has a much more unidirectional, well-collimated source that is incident normal to the surface. In addition, fencing problems can be improved or eliminated using a bi-layer resist scheme as shown in figure 6(*b*). Here, a co-polymer or lift-off resist (LOR) is used underneath the mask to provide undercut to the exposed regions. However, it is common to form some tapering of the material near the edges from shadowing of the incident atoms. The use of undercut in closely spaced or dense arrays can result in mechanical failure of the resist since the undercut can overlap between features.

If more than one deposition target is used to make an alloy or a multilayer, the degree of shadowing that occurs will depend on the location of each target, and therefore will vary for each material unless the sample is repositioned for each material. Such inhomogeneity is a critical factor in multilayers such as Co/Pd, Co/Pt and Co/Ni, where the interfaces and layer thicknesses profoundly affect the anisotropy, as well as GMR and TMR devices where electronic shunting can occur at the edges due to a change in the electrical resistance or the tunnel barrier quality.

An alternative additive process has been shown to produce large-area dense arrays of nanostructures which makes use of electro-deposition through the mask material. Many of the fencing and shadowing issues associated with lift-off are not present in this scheme since the material does not grow/deposit on the mask and the material does not strictly coat the surface in a line-of-sight manner. As a result, high aspect ratio structures can be produced. However, most magnetic structures produced with electro-deposition do not consist of complex multilayers [67].

2.2.2. Subtractive approach. In a subtractive approach, the deposition of the magnetic material is performed prior to the pattern transfer. The mask plays the opposite role; protecting regions of the film from the etching process, as shown in figure 6(*d*). A benefit of this approach is that precise control of the layer thicknesses can be achieved since the material is deposited prior to patterning. As a result, this approach is almost exclusively used for technologies that rely on multilayers and superlattices, as well as GMR and TMR devices. However, considerable attention must be placed on the etching technique and parameters. The most common problems introduced during the etching process are that of etch induced damage at the edges and re-deposition of material. Both of these parasitic effects can change the magnetic properties of the edge material [68].

Where reactive-ion etch based processes are common for the CMOS process, ion beam milling is an extremely useful etch process for magnetic materials because the etch

rates are less selective to most transition metals and alloys. Thus, a complicated spin-valve structure that consists of many different material layers can be etched entirely without having to change the etch conditions or chemistry for each layer. In addition, since the etch process is line-of-sight with respect to the incident ions, the etch is very anisotropic allowing for direct pattern transfer from the mask. While the lack of elemental selectivity is beneficial when etching through complicated multilayer samples, it also poses a challenge in the choice of mask material. In other words, the mask material will also be simultaneously etched during the ion-milling process. Some materials such diamond-like carbon (DLC), Al_2O_3, TaC and Ti have exceptionally low mill rates and therefore provide an excellent mask material to use when possible. The remaining mask material may be left on the structures after ion milling. In a self-aligned process, the trenches are back-filled with an insulator, followed by the lift-off of the mask material.

As previously stated, the challenge to a subtractive method resides in mitigating the ion damage that can occur in the edge region and the possible re-deposition of the etched material along the edges. Many perpendicular multilayer systems, such as Co/Pd, are especially sensitive to ion induced damage and can transition from having a strong perpendicular anisotropy to an in-plane one with only a small amount of ion dose [69–71]. As a result, the magnetic anisotropy of the edge material can be modified significantly, resulting in a change in the reversal process of a nanostructure [68]. Re-deposition of material is a serious problem for MTJs since it can provide a conductive path across the insulating barrier. Extreme oxidation with a reagent such as ozone has been used to render redeposited materials non-conductive in MTJs [72].

For some applications, the effects of ion damage can be mitigated by a 'pre-pattern' process [73]. Here, the *substrate* is first patterned prior to the deposition of the magnetic material. The isolated magnetic nanostructures are then formed at the top of the pillars (and at the bottom down in the trenches patterned into the substrate), circumventing many of the problems encountered with both lift-off and etching. However, one artefact of pre-patterning is the presence of material in the trenches. Recently, this effect was mitigated in Co/Pd by reacting the trench material after deposition to a form a non-magnetic compound [74]. Another artefact of this process is deposition of magnetic material on the sides of the pillars, which can be partially mitigated by consideration of the location of deposition targets [73, 75].

Another subtractive method often used in the research environment is direct patterning using a focused ion beam (FIB). Here, an energetic beam of Ga ions (other ions can be used as well) is focused onto the sample surface where it directly removes the material. By rastering the beam across the surface, an arbitrary pattern can be directly etched out of the material. The advantage of a FIB is that no mask or lithography step is needed since only the material where the beam is directed is removed. One disadvantage is low throughput. Another is that the effects of ion damage are still present. Particularly in MTJ work, Ga ion implantation is known to cause problems for the delicate oxide barriers. A recent study showed quantitatively, the inverse relationship between Ga dose and TMR [76].

Finally, it is worth mentioning that semi-isolated magnetic regions can be fabricated through ion irradiation [77]. In many multilayer materials such as Co/Ni, Co/Pd and Co/Pt, the perpendicular anisotropy can be destroyed by exposing the material to small doses of ion radiation [78, 79]. Thus, if this material is selectively irradiated through a mask, then regions of high and low anisotropy can be created. Alternatively, a material can be implanted that further modifies the magnetic properties. For example, Cr can be implanted into Permalloy to create regions of lower magnetic moment [80]. These regions are not strictly isolated since there is still a significant amount of exchange coupling between the high and low anisotropy regions, but the magnetic behaviour can be well controlled and laterally defined.

2.3. Pattern creation

Regardless of the method used for the pattern transfer, a mask needs to be formed. There are many methods used to create masks and more variations emerge everyday. Here, we focus on some of the common approaches useful in research laboratories.

2.3.1. Photolithography. One of the most common forms of creating patterns in materials is photolithography. A reticle is first made that contains the desired patterned features or image, which is typically a transparent glass substrate material with a thin Cr layer on one side that has been etched to form the image. The sample or wafer is coated with photoresist; a material that is highly sensitive to ultraviolet (UV) light. When the photoresist is exposed to a developer (typically a basic solution) the regions that are exposed to UV light either dissolve more easily (positive resist) or become more resistant (negative resist) to the developer. The pattern on the reticle can then be transferred to the photoresist on the sample by directing UV light through the reticle. Usually, this is achieved in one of two ways: a contact aligner or stepper. In a contact aligner, the reticle is held in direct contact with the sample/photoresist (or at least within several micrometres) and the UV illumination from the back side of the reticle exposes the photoresist. The pattern transfer from the reticle to the photoresist is strictly 1 : 1 (i.e. the image on the reticle is not focused) and the reticle usually includes the pattern over the entire sample. In a stepper, the UV light passing through the reticle is usually optically focused further on the sample reducing the size of the image of the reticle on the sample. This is possible since the reticle is separated from the sample and may contain optical elements in between. Unlike a contact aligner, the image on the reticle is typically that of a single die on the sample or wafer. Thus, the images from the reticle can be 'stepped' or sequentially exposed across the sample or wafer.

One major limitation of photolithography is that the minimum feature size is fundamentally set by the wavelength of the UV light and the numerical aperture of the optical system. For most standard UV photolithography systems at research institutions, the practical minimum feature size is typically around 500 nm. In order to achieve optical lithography below 100 nm, extreme ultraviolet (EUV) systems

must be used, and when used in combination with immersion lithography, even smaller features can be achieved. The shorter wavelength of EUV combined with the high effective numerical aperture of the immersion lithography scheme can provide feature sizes below 40 nm [81]. Because of the limitations in feature sizes, photolithography is generally not useful in creating nanostructures directly. However, this process is still very useful in patterning larger features in waveguides and devices (i.e. conductive contact leads to provide electrical contact to the device.)

2.3.2. Electron beam lithography. One of the most used and versatile direct write lithography methods used in magnetic nanostructure research is electron beam lithography (EBL). Here, an electron beam is scanned across the sample surface and exposes an electron beam resist, such as PMMA and HSQ. As with photolithography, the resist can be either positive or negative and is developed after exposure to form the pattern on the surface. Since the deBroglie wavelength of 30–100 keV electrons is much smaller than inter-atomic distances (<0.1 nm), the minimum feature size is not fundamentally set by the electron beam wavelength as it is with photolithography. In fact, feature sizes below 10 nm are now routinely demonstrated with EBL. The resolution in EBL, however, is not necessarily set by the electron beam spot size. As the electrons penetrate the resist and sample, they will scatter causing the generation of secondary electrons and a collision cascade (forward and back-scattered events). Both the secondary electrons and scattered electrons will contribute to the exposure of the resist, causing a region much larger than the electron spot size to receive a significant exposure. These parasitic effects can generally be minimized using higher energy electron energies. Since scattering events and secondary electron generation are material dependent, adjustments to the dose may be needed depending on the sample composition. In other words, the optimal dose for a Si sample may be different from the optimal dose on a metallic sample. Another parasitic effect of the secondary electron generation and scattering events is that of proximity effects. This is most problematic when writing two closely spaced features since a region that separates the two features (and the features themselves) will be partially exposed from the secondary electrons and scattered electrons. Many modern EBL tools have the ability to correct for proximity effects by adjusting the written dose across the pattern to compensate.

While EBL is of great value in the research environment, it is impractical for large area or high throughput applications. This is largely a result of the fact that it is a slow, serial writing process. However, having the ability to write feature sizes down to and below 10 nm in the research environment is invaluable. In addition, the advantage to EBL is in the ability to write almost arbitrary shapes and patterns without having to make a mask. In other words, it is possible to take patterns created in a computer aided design (CAD) program and directly write them to the sample without any intermediate steps.

2.3.3. Interference lithography. Interference lithography makes use of UV laser sources to create large-area periodic patterns that are directly exposed to the resist without the use of a mask [82]. Essentially, the beam from the laser is first split and then recombined on the surface of the sample that is coated with a UV sensitive resist. As the beams recombine, they interfere forming a periodic 'fringe' pattern on the surface. This process is analogous to the fringe patterns that form in wave physics when a plane wave encounters a double slit and interferes with itself on the other side of the double slit. However, in this case, the split lasers maintain a coherent plane wave characteristic and therefore the fringe pattern is of constant period defined by $\lambda/(2\sin\theta)$, where λ is the wavelength of light and θ is the half angle between the two beams. From this equation, we see that the minimum feature size is fundamentally limited to $\lambda/2$. Interference lithography is very useful in patterning dense arrays that cover large areas; limited solely by the diameter of the spot size of the laser on the surface. This technique has been successfully used to pattern arrays of nano-stripes [83–85] (see also [62, 65] and references cited therein). Another advantage to this technique is that it can be inexpensively constructed in a laboratory. The obvious disadvantage resides in the fact that the lithographic features are limited to arrays of identical and symmetric structures.

2.3.4. Self-assembly. The self-assembly of block co-polymers [86] as well as other nanoparticles [87, 88] is being explored as a template to create dense arrays of nanostructures. Close-packed patterns with strong short range order generally result from this process with periodicities already demonstrated below 28 nm in magnetic systems [88, 89].

While self-assembly possesses strong short range order, the lack of long range order prevents it from being directly used for applications such as BPM. However, this limitation can be overcome using another lithographic technique to provide the long range order. This guided self-assembly can take the form of fabricating physical patterns such as trenches that the particles can assemble in [90], or by providing arrays of chemically functional sites on the surface that guide the natural pattern formation on the surface [89, 91]. If these guides are carefully engineered such that they occur at integer multiples of the natural self-assembly spacing, then high quality long range order can be formed over larger ares while simultaneously maintaining the short range order of the self-assembly process.

2.3.5. Nano-imprint. As the name suggests, nano-imprint lithography (NIL) makes use of a rigid mould consisting of a pre-defined pattern that is used to physically imprint or stamp the pattern into the resist. The mould itself is typically fabricated by EBL or interference lithography methods. When the mould is held in contact with the resist, the resist is either heated to soften the resist and then cooled before removing the mould (thermoplastic method), or the resist is cured with UV light before removing the mould (photo-imprint method). This technology shows promise in overcoming throughput limitations of BPM since it can pattern large areas quickly and is also currently being explored as the lithography step for guided self-assembly. NIL is not as generally advantageous in the research laboratory since patterns are limited to those

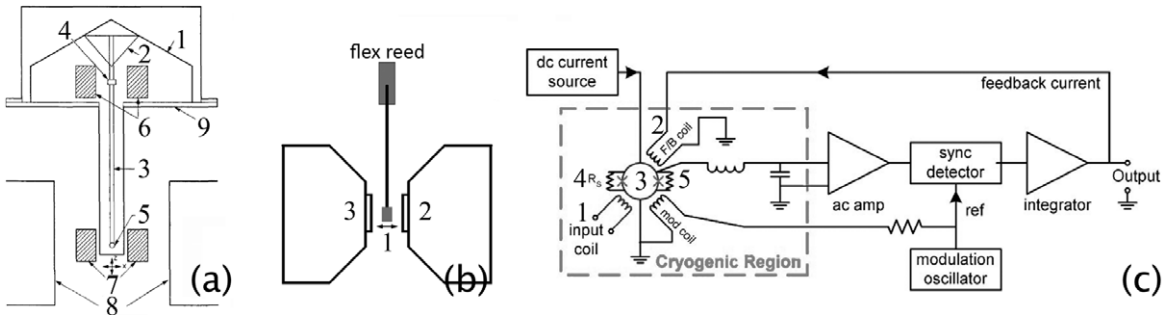

Figure 7. Schematics of (*a*) VSM (Reprinted with permission from [92], copyright 1959 by the American Institute of Physics.). (*b*) AGM adapted from [93] and (*c*) dc-SQUID (Reprinted with permission from [94], copyright 2006 by the American Institute of Physics.).

pre-defined on a mould. Also, while simple in principle, the process can in reality be rather complicated with special attention needed in optimizing the force exerted between the mould and resist, flatness of mould as it is brought into contact, proper release of the mould from the resist, removal of residue on the mould and mould fabrication.

3. Static measurements

Ways to measure magnetic properties (e.g. magnetic field strength, magnetization, magnetic anisotropy) are numerous and take varied forms. Measurement of magnetic properties of nanostructures in particular presents new and unresolved challenges in achieving adequate SNR and spatial resolution. Not only is the measurement of magnetic properties vital for all of the technologies previously discussed, metrology development is an important area of research in and of itself. We will therefore spend a large portion of this paper discussing the method used for nanostructures. We focus on the measurement of magnetization and magnetic anisotropy, as they are the most sought-after quantities. In this part, we discuss the common measurement methods for the low-frequency (1 Hz to 1 MHz) magnetization response as a function of applied field in nanostructures. We will reserve the discussion of high-frequency measurements (above 1 GHz) for section 4.

3.1. Magnetometry

3.1.1. Magnetometers. Magnetometers measure the net magnetic moment of a sample as a function of an externally applied magnetic field. The benefit of traditional bulk magnetometers, and also magneto-optic Kerr effect (MOKE) measurements, lies in the relative ease in sample preparation. Automated measurements can be made as long as the sample fits into the measurement cavity, and enough magnetic material is present to produce acceptable SNR. The most important point to remember when interpreting magnetometry data is that the measurement represents a volume average magnetic response. It is not possible to pinpoint specific nanostructures or locations of defects that may have caused observed magnetic behaviour. Responses due to shape anisotropy or magnetostatic interaction due to arraying must be understood and dealt with beforehand, for these effects are generally lumped together in magnetometer measurements.

Vibrating sample magnetometer. Foner, in 1959, described the original design of a vibrating sample magnetometer (VSM) based on a lock-in amplifier [92]. The VSM is so named because the sample physically vibrates (typically at frequencies between 50 to 100 Hz). Figure 7(*a*) is a schematic of the VSM. Its essential parts are labelled from 1 through 9. The sample itself is located at position 5, and it is vibrated by a loudspeaker assembly (positions 1, 2 and 4) along the axis of a non-magnetic sample mounting rod (position 3). A reference magnet is secured to the opposite end of this rod (position 4). A pair of coils (position 7) senses the oscillatory magnetic field produced by the moving sample and produces a voltage signal. A second pair of reference coils (position 6) senses the oscillatory magnetic field produced by the moving reference magnet and likewise produces a reference voltage signal. Since the reference magnet and the actual sample should always move with the same velocity, the reference can provide feedback to maintain vibration consistency. The magnetic moment of the sample is proportional to the signals processed from coils at positions 6 and 7. This output is measured with a lock-in amplifier so that the signals at the other frequencies can be eliminated. An electromagnet used to produce the external field for hysteresis measurements is located at position 8; field output is typically below 3 T unless superconducting magnets are used. Field is typically stepped on the order of 1 s.

Only two factors limit the acceptable physical specimen weight and dimension. It has to fit in the air gap defined by the coils at position 7, and the mass of the sample should not unduly inhibit the vibration. For most magnetometers, this implies a sample of approximately 10 mm diameter and 1 g mass. A large range of measurement temperature, from that of liquid He to 1200 K, is possible depending on the specific magnetometer and the available hardware adaptations.

The VSM noise floor is typically about 1×10^{-9} A m^2 (1×10^{-6} emu) at 1 Hz. If we were to measure a 20 nm thick nickel film, assuming a magnetic moment of 58 A m^2 kg^{-1}, a square piece, 0.5 mm on a side, would be required for SNR of 10. Clearly, to attain a reasonable signal from the VSM, an ensemble of magnetic nanostructures covering an area far greater than 0.25 mm^2 will be required.

Alternating gradient magnetometer. The alternating gradient magnetometer (AGM) was first described by Zijlstra in 1970 [95] and later by Flanders in 1988 [96]. Figure 7(*b*) is

a schematic of the basic concept. The sample (position 1 in figure 7(*b*)) is mounted on a non-magnetic flexible reed and is suspended in the gap between a pair of coupled ac field coils (positions 2 and 3). Due to the presence of the magnetic sample, an alternating field causes the reed to deflect. When this field is tuned to the mechanical resonant frequency of the reed and sample assembly, the deflection of the reed is amplified, and this deflection magnitude is directly proportional to the moment of the sample. In the modern instrument, the deflection of the reed is measured by a piezoelectric sensor. Specimen mass and size requirements and magnetic fields attainable are similar to those for the VSM. Temperature range from that of liquid He to 473 K is possible with the appropriate hardware. Compared with the VSM, the AGM can be up to 100 times more sensitive, 1×10^{-11} A m^2 (1×10^{-8} emu). Using this figure and assuming again that we wished to measure a 20 nm thick nickel film, we will now only need a square piece that is 55 μm on a side in order to obtain SNR of 10, a significant improvement, but again, a significantly larger patterned area would be required for measuring nanostructures.

Superconducting quantum interference device. Magnetometers based on superconducting quantum interference devices (SQUIDs) are considered the most sensitive of all magnetometers. A SQUID consists of a closed loop made of a low temperature superconductor like NbTi or Nb_3Sn, with one or two Josephson junctions. The operation of a SQUID magnetometer is based on two fundamental physics principles: (1) the use of Josephson junctions as a means to create path differences (interference) in an otherwise coherent supercurrent persisting around the superconducting loop and (2) the fact that the magnetic flux trapped inside the area enclosed by the superconducting loop must be in integer units of a flux quantum, $\Phi_0 \equiv h/2e$. The supercurrent within the loop self-compensates to ensure that the flux through the loop is an integer multiple of Φ_0. For the detailed physics and design variations of the SQUID, refer to the review by Fagaly [94] and the references therein.

The fact that the SQUID is superconducting makes liquid He a requirement for operation. Figure 7(*c*) is a schematic diagram of the SQUID magnetometer. The cryogenic region (dashed rectangle) contains the magnetic signal input coil (position 1), the feedback coil (position 2), the SQUID itself (position 3, with the locations of the Josephson junctions labelled as 'X's around the ring) and two resistors (positions 4 and 5) that shunt the junctions for the purpose of preventing hysteretic losses in the measurement.

The magnetic signal from the sample is inductively coupled to the SQUID by a set of pick-up coils located in the cryogenic region. The sample itself is situated outside the cryogenic region, and therefore, temperature-dependent measurements in the range 1.8–1000 K can be made independent of the cryogenic operation of the SQUID. The feedback coil detects a voltage, effectively correlated with the oscillations in the self-compensating critical current in the SQUID as a direct result of the magnetization of the sample. These oscillations are quantized, with an oscillation period of Φ_0. Using superconducting magnets, SQUID magnetometers can produce very large static fields; most commercial tools can generate up to 7 T. Sample dimensions are similar to the ones discussed for the other techniques. Quoted sensitivity for commercial instruments is equal to or better than 1×10^{-11} A m^2, making it the most sensitive of the bulk magnetometry techniques. However, recent developments have proposed to make single particle magnetometry possible on a SQUID by applying clever engineering and materials science to the Josephson junction. In one design, the junctions consist of a single, single-wall carbon nanotube [97]. Here, a test sample of Mn_{12} molecular magnet is situated directly on top of the nanotube, thus significantly improving the coupling efficiency, achieving sensitivity on the order of $10^{-4}\Phi_0$. Others have made nano-SQUIDs with the idea that they can be integrated into a scanning probe microscope (such as a scanning SQUID microscope) for magnetic imaging on the nanoscale [97–99]. Scanning SQUID microscopy has been successful at imaging current in integrated circuits [100], and should in principle be able to map magnetization of magnetic nanostructures.

3.1.2. Magneto-optic Kerr effect. When polarized light is reflected from a magnetic surface, the polarization of the reflected light can undergo a change in polarization state that is dependent on the relative orientation of the magnetization and the scattering geometry. This process is referred to as the MOKE [101, 102]. MOKE results from phase shifts between left- and right-circularly polarized light that is scattered from a magnetic surface. From a classical perspective, the magneto-optic effect can be explained from the Lorentz force providing anti-symmetric, off-diagonal elements in the dielectric tensor that is a function of the sample magnetization. Since linear polarized light is a superposition of left- and right-circularly polarized light, linear polarized light can be used for MOKE, and is in fact the most common experimental approach. Since MOKE is highly dependent on the optical properties of a specific sample [103], it is not amenable to quantitative determination of the saturation magnetization (M_s), but is very useful in determining the coercivity or saturation fields.

The three typical MOKE geometries are polar (P-MOKE), longitudinal (L-MOKE) and transverse (T-MOKE). In P-MOKE and L-MOKE, the applied field is, respectively, either perpendicular or parallel to the sample surface, in the scattering plane. The polarization of the reflected light undergoes a rotation and/or change in ellipticity that is a function of the magnetization of the sample. Thus, for P-MOKE and L-MOKE, the polarization state can be related to the magnetization. In T-MOKE, the magnetic field is applied perpendicular to the scattering plane. Unlike P-MOKE and L-MOKE, the polarization state of the reflected light is not affected in T-MOKE, but rather, the reflected light *intensity* undergoes a change in response to the magnetization.

One advantage of MOKE over bulk magnetometers is that the light can be focused down to a small spot size, and thus, the magnetic properties of a sample can be locally probed. The size of the spot is solely determined by the diffraction limit set by the wavelength of light used and the numerical aperture

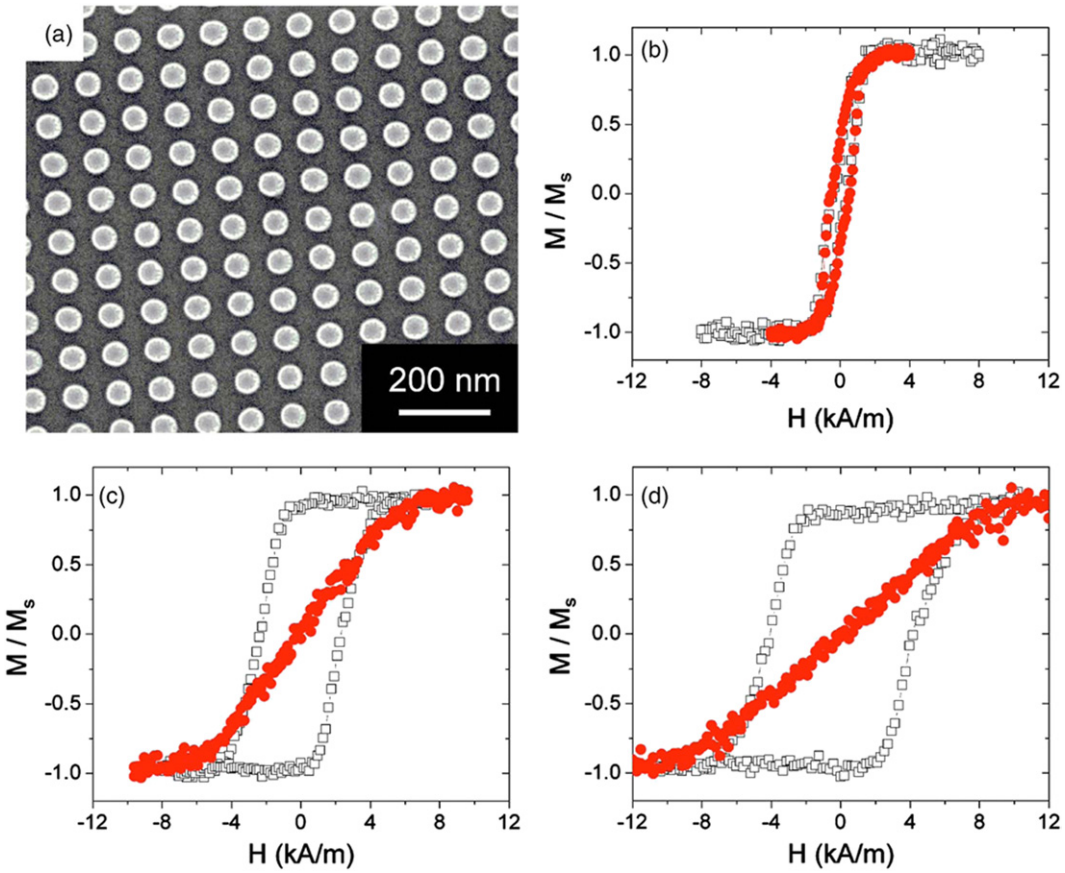

Figure 8. (*a*) SEM image of 65 nm × 71 nm elliptical $Ni_{80}Fe_{20}$ dots. (*b*) Easy axis open squares and hard axis closed circles hysteresis loops for an array of circular $Ni_{80}Fe_{20}$ dots, 65 nm × 65 nm. (*c*) Easy axis open squares and hard axis closed circles loops for an array of 5% elliptical $Ni_{80}Fe_{20}$ dots, 65 nm × 68 nm. (*d*) Easy axis open squares and hard axis closed circles loops for an array of 10% elliptical $Ni_{80}Fe_{20}$ dots 65 nm × 71 nm. (Reprinted with permission from [104], copyright 2007 by the American Institute of Physics.)

of the optics. Although some effort is needed, a diffraction-limited spot size (300–500 nm for optical wavelengths) can be used to measure individual nanostructures. However, spot sizes of a few micrometres are easily achieved, and can still be used to measure the properties of individual or ensembles of nanostructures [104]. Figure 8 shows the magnetization curves obtained from L-MOKE taken on arrays of 65 nm $Ni_{80}Fe_{20}$ nanostructures with varying amounts of ellipticity. The variation of the hysteresis on the ellipticity of the nanostructures is clearly measured.

Optical measurements on arrays of nanostructures also creates an interesting effect: the magnetic nanostructure arrays act as a diffraction grating to the light. The reflected light is therefore split into several diffracted beams. By analysing the MOKE signal of each diffracted beam individually, it was recently shown that additional information can be deduced about the magnetic configuration and/or reversal process of nanostructures [105].

3.1.3. Anomalous Hall effect. The Hall effect, discovered in 1879 [106], is a direct result of the Lorentz force $F = q\vec{v} \times \vec{B}$ acting on a charged particle q moving through a magnetic field B. Spatial accumulation of charges produces a voltage difference (Hall voltage) across a surface in the direction of $\vec{v} \times \vec{B}$. In the case of non-magnetic metals and semiconductors, the Hall voltage is linearly proportional to the applied field. For magnetic metals however, in addition to the ordinary Lorentz contribution, there is an additional contribution to the Hall voltage that is proportional to the magnetization M. Since magnetic materials will eventually reach saturation with increasing magnetic field H, the measured Hall voltage is a linear function of H up until saturation. This non-linear Hall effect in magnetic metals is known as the anomalous (AHE) or extraordinary Hall effect (EHE) and was first observed experimentally in 1910 [107].

The Hall resistivity ρ_H in the direction of $\vec{v} \times \vec{H}$ is given by

$$\rho_H = R_0 B + R_s \mu_0 M = R_0 \mu_0 (H + M) + R_s \mu_0 M. \quad (1)$$

Equation (1) can be rewritten so that the H contribution is separated from the magnetization of the sample as shown in equation (2).

$$\rho_H = \mu_0 R_0 H + \mu_0 (R_0 + R_s) M(H) = \mu_0 R_0 H + \mu_0 R_1 M(H). \quad (2)$$

The first term in equation (2) is the ordinary Hall resistivity due to the Lorentz force on the applied current; it contains the ordinary Hall coefficient R_0 and the resistivity depends only on the applied field H. The second term is the anomalous

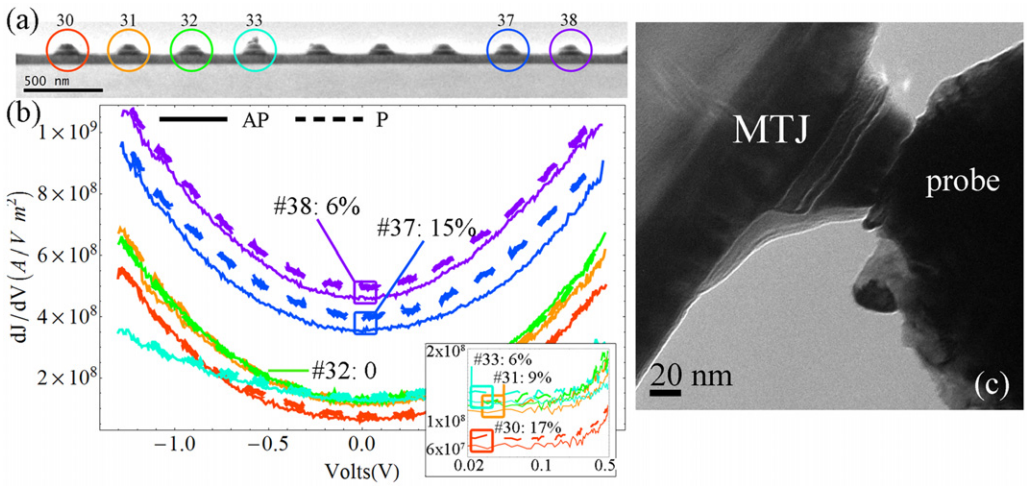

Figure 9. *In situ* TMR measurements on nano-MTJs [55]. (*a*) TEM image of a row of nano-MTJs. (*b*) Conductivity measurements of corresponding devices in parallel and antiparallel states. (*c*) Contact being made to a MTJ.

Hall resistivity; it contains the anomalous Hall coefficient (AHC $= R_1 = R_0 + R_s$) and the resistivity depends only on M. Both R_0 and R_1 have units of $m^3\,C^{-1}$. It is worthwhile to point out that two main conflicts exist in the definition of the extraordinary Hall coefficient, and this conflict came about through the expression of ρ_H as a function of H (the field) or B (the induction). Early literature explicitly defined AHC as R_1, which is the result of defining ρ_H as written in equation (2) [108–110]. However, Berger [111] defined ρ_H as written in equation (1), which results in AHC being defined instead as R_s, and some have since followed this convention [112], while others continue to use the older one [113]. Since $R_s \gg R_0$ in ferromagnets, the precise definition of AHC may have been inconsequential. Nonetheless, it is important to be mindful of the difference.

The fact that ρ_H is proportional to the magnetization in ferromagnets means that AHE may be exploited as a form of magnetometry. In ferromagnets, R_1 is typically at least an order of magnitude larger than R_0 [110, 114]. However, R_1 or R_s is highly dependent on temperature [114], sample impurities [111, 115] and thickness [116–118]. Over the last century, lively debates have erupted over the controversy surrounding the origin and mechanisms behind the various R_1 dependences [109–111, 119, 120], and much effort has been devoted to find a unified theory [113, 117, 121]. Nonetheless, as long as temperature and the physical attributes of a ferromagnetic sample such as impurity concentration and geometry remain unchanged for the duration of the measurement, ρ_H depends only on the magnetization of the sample. AHE can be a good candidate for nanostructure magnetometry, because unlike conventional magnetometry where the signal is proportional to the magnetic volume measured, ρ_H increases with decreasing film thickness. Already groups have made progress using AHE as a form of magnetometry to study switching in individual magnetic nanostructures. Kikuchi *et al* have demonstrated that AHE is sensitive to a single 60 nm FePt nanodot at temperatures between 10 and 300 K [122]. Belmeguenai *et al* [123] have observed dynamic oscillations in Pt/Co multilayer sub-micrometre structures following a microwave pulse. More recently, Alexandrou *et al* [124] have shown that the individual switching events in several Co/Pt multilayer nanodots can be simultaneously captured in one AHE loop. Indeed AHE is showing enough magnetic sensitivity in nanostructures that it is a promising technique for single nano-particle magnetometry in both the static and dynamic domains.

3.1.4. Dc transport measurements. In GMR and TMR devices, the resistance across the device depends on the relative angle between the magnetization of the magnetic layers. Thus, in such a device, the relative magnetization state of the two nanostructured layers can be measured by monitoring the electrical resistance of the device as a function of the applied magnetic field. The magnetization of a single layer can be measured if the second magnetic layer is either pinned to an antiferromagnetic layer and/or has a significantly larger coercivity relative to the first magnetic layer, thereby acting as a reference layer. In this case, the magnetization curves for the softer layer can be independently determined by measuring the resistance across the device as a function of the applied magnetic field. This is commonly referred to as an MR curve and is extremely useful in characterizing the static magnetic properties in individual nanopatterned devices.

For example, in order to achieve high density in MRAM arrays, it is important not only to control TMR values, but also the uniformity of TMR values across a chip so that reading and writing currents may be optimized. Of course, during manufacturing, various processes can produce defects such as pinholes and hot spots that fundamentally change the tunnelling barrier characteristics and therefore, the TMR distribution. *In situ* dc transport measurements were recently performed in a TEM to measure the TMR distribution in a row of fully operational, well-isolated nano-MTJs [55] (figure 9). Because the nano-MTJs had electron-transparent dimensions, such an experiment made it feasible to quantitatively compare transport characteristics, in addition to MR curves (not shown), with the corresponding device morphology and defect profile in adjacent devices.

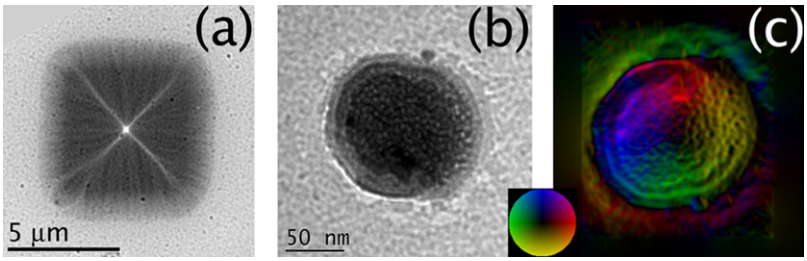

Figure 10. (*a*) Fresnel image of a 6 μm × 6 μm $Ni_{80}Fe_{20}$ structure. (*b*) Fresnel image of a 100 nm CoFeB dot [128]. Note defocus (Δz) not sufficient in this image to reveal vortex core. (*c*) Transport of intensity equation (TIE) reconstruction of (*b*) revealing flux-closure domain in false colour [128]. Colour wheel gives the direction of magnetization.

3.2. Imaging

The capability to view the spatial profile of the magnetization with nanometre resolution is invaluable in understanding a sample's remanent state and its response to externally applied fields. Implicit in the time required to generate these images (whether with CCD cameras typical of electron microscopy, or through rastering of sequentially generated voltage signals as in probe microscopy), magnetically sensitive images are generally static measurements, with rare exceptions.

3.2.1. Electron imaging. Despite the complexity and cost of electron optics, two advantages to an electron-based magnetic imaging system are improved spatial resolution due to small electron wavelengths, and the inherently rich physics from the interaction of moving, charged particles with a magnetic specimen. In this section, we cover some of the more well-established magnetic imaging techniques based on the electron as a probe, with the most common electron sources being the transmission/scanning electron microscopes (T/SEM). This section is subdivided into Lorentz force and non-Lorentz force based techniques. The Lorentz-based techniques discussed here are all performed in transmission electron microscopes (TEM).

Lorentz transmission electron microscopy. A locally varying magnetization in a magnetic sample will exert a spatially varying Lorentz force in the electron probe trajectory. This is the basis of Lorentz transmission electron microscopy. There are several variants of Lorentz microscopy that we will now individually address.

Fresnel mode. Perhaps the most straightforward way to obtain magnetic information is through Fresnel contrast generated by defocusing (Δz) the imaging lens. This way of imaging is often simply referred to as Lorentz microscopy even through strictly speaking, the Fresnel defocus technique is only one of many forms of Lorentz microscopy. In the classical picture, incident electrons, typically between 100 to 300 keV, travel through a magnetic sample and are deflected due to the Lorentz force. As a result, at the locations where the magnetostatic potential of the specimen changes abruptly, e.g. at domain walls and edges of a structure, the transmitted electrons are not projected with uniform intensity at the image plane. Contrast variations, which can be thought of as a local pile up or deficit of electrons at the image plane due to the Lorentz deflections, are projections of the position of the magnetic boundaries such as domain walls or the edge of a magnetic structure. Regions of uniform magnetization (e.g. within domains or single-domain nanostructures) do not contribute to the contrast. In practice, intra-domain ripples are frequently observed in a polycrystalline magnetic sample using the Fresnel contrast technique. These ripples are caused by a superposition of magnetic contrast generated from randomly oriented grains and therefore randomly oriented magnetocrystalline easy axes with respect to the mean magnetization of the domain [125–127] and it is understood that the magnetization within a domain generally runs perpendicular to the ripple rows [125]. Additionally, contrast is a function of the defocus, that is, larger Δz produces greater Fresnel contrast. Figure 10(*a*) is an image of a 6 μm × 6 μm $Ni_{80}Fe_{20}$ structure taken in the Fresnel mode. Clearly present is the vortex state and the ripple contrast in each quadrant.

Based on the equation for the Lorentz force, it is possible to determine unambiguously the exact magnetization direction (but not magnitude) in any domain provided that we know whether the image is an over-focused or an under-focused image (sign of Δz). Examining the Lorentz force equation it is evident that magnetic contrast can result only from magnetization components perpendicular to the beam direction as the Lorentz force on the transmitted electrons is zero for magnetization parallel to the beam.

The sample geometry requirement is that of a TEM sample, that is, 3 mm disc and thickness of about 100 nm for a 300 kV microscope in order to ensure electron transparency. The primary objective lens of a typical TEM produces a few teslas of magnetic field at the specimen position. Therefore, Lorentz microscopy is usually performed with the primary objective lens off in order to prevent magnetic saturation of the sample. Instead, some combination of a Lorentz lens (i.e. a lens with a long focal length) set far from the specimen location or a specially designed field-canceling assembly or a shielded specimen region is usually required for imaging in a magnetic field-free environment. Nevertheless, precautions must be taken during specimen insertion because the sample will traverse the microscope column, which can contain strong ferromagnetic structural components and various electromagnetic lenses in remanent state. Accidental magnetization of the sample during sample insertion is always possible unless the specimen insertion fields are well-characterized [129].

For a field emission electron source, the limiting factor on resolution in the Lorentz mode is the coefficient of spherical aberration (C_s) of the imaging lens. Image delocalization (i.e., features in the image are displaced with respect to their true location in the specimen) is particularly problematic and it is directly related to Δz and C_s [130]. The resolution in Fresnel mode using a lens with long focal length (C_s, typically a few metres) is about 100 nm. However, with a modern C_s-corrected microscope, resolution on the order of 1 nm is possible with this technique.

It is possible to image the in-plane magnetic response of a specimen with an applied magnetic field in several ways: either along the optic axis by exciting the objective lens (perpendicular to specimen plane only), provide an in-plane component to the applied field by tilting the sample, or within the plane of the specimen by Helmholtz coils built onto the specimen holder [131]. Sometimes, authors mention 'imaging the magnetization reversal dynamics with Lorentz microscopy' and it is worthwhile to point out a misconception. Changes such as domain wall movements, when recorded on CCDs or video rate cameras are, strictly speaking, not dynamic. Magnetization dynamics refers to processes on timescales of precession frequencies, which span at most a few nanoseconds. Frames on CCD and video rate cameras are recorded from milliseconds to seconds and the observations are therefore mostly in magnetic equilibrium. With the recent demonstration of pump–probe TEM techniques [132, 133], however, true sub-nanosecond magnetization dynamic measurements with nanometre spatial resolution are very possible in the near future.

Foucault mode. The same physical principle behind the Fresnel contrast mode can produce contrast in the actual domains (not domain walls) in the Foucault mode. When imaging a 180° domain wall, for example, the electron beam at the back focal plane (BFP) of the imaging lens is actually split into two distinct spots perpendicular to the domain wall as a result of the Lorentz force. Using an aperture, one of the spots may be selected or excluded from image formation. This is similar to the process used to form a dark-field image. At the image plane, the bright or dark domain was formed by the spot included or excluded by the objective aperture at the BFP, and the direction of magnetization of the bright domain is perpendicular to the direction of beam split, in accordance with the Lorentz force. Unlike in Fresnel mode, the image is taken at focus, i.e. $\Delta z = 0$. Since contrast comes not from the abrupt change in magnetization as in the case of Fresnel mode, the direction of magnetization in mono-domain magnetic nanoparticles would not be evident from the Foucault images. Therefore, Foucault images are not particularly useful for imaging magnetic nanostructures unless domains are present. Like the Fresnel mode, the magnetization direction is readily available. However, estimation of the magnitude of magnetization is a significantly more involved process, and so it is typically not done. The spatial resolution for the Foucault technique is better than that of the Fresnel technique because images are acquired close to focus.

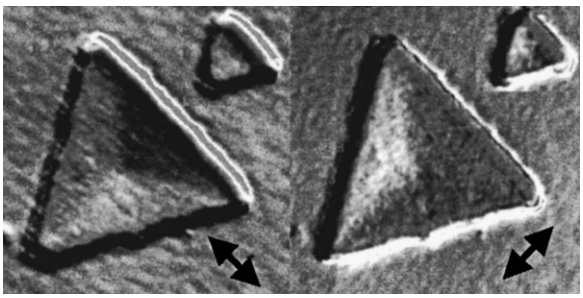

Figure 11. Flux-closure domain structures in Co elements 36 nm thick, obtained using the DPC mode TEM. The small and large elements are ≈100 nm and ≈300 nm in lateral dimensions respectively. The arrows indicate the direction of sensitivity of the magnetic induction. (Reprinted with permission from [143], copyright 2001 by the American Institute of Physics.)

Differential phase contrast. Both Fresnel and Foucault images formed with parallel illumination in TEM mode can also be formed with a convergent beam in STEM mode [134–137]. Differential phase contrast (DPC) method is a form of Lorentz microscopy in STEM mode. Developed by Chapman *et al* [138], the necessary requirement is a circular quadrant detector located below the projector lens [139, 140]. Revisiting the 180° domain wall example, when the convergent electron beam probes two adjacent domains, the divergent beam on the exit surface of the specimen is deflected according to the Lorentz force, as in the Fresnel mode. However, because the beam is divergent, different numbers of electrons fall on opposing quadrants of the detector. One can derive quantitative magnetic contrast by subtracting signals between any two opposing quadrants [140]. The optimum magnetic contrast comes from the two opposite quadrants whose conjoining axis lies perpendicular to the direction of magnetization [138, 141]. Unlike Fresnel mode or Foucault mode, DPC is a semi-quantitative technique in that contrast is directly proportional to the in-plane component of the magnetization.

The temporal resolution of DPC is the rastering time required for acquiring STEM image, which is comparable to TEM images. The advantage of DPC over Fresnel mode is in the spatial resolution. Where Fresnel mode suffers from significant resolution degradation due to the mandatory defocusing requirements, DEC does not, and its resolution is about 20 nm in uncorrected microscopes [142]. Kirk *et al* (figure 11), was able to show 100 nm Co structures in the vortex state (figure 11) [143].

Electron holography. In electron holography, interference of electron waves generates a hologram at the image plane. While there are at least 20 varieties of electron holography [144], the most common is the off-axis method. The original electron interference work using a charged biprism wire was done in 1956 [145].

The phase of the electron at the exit face of the sample can be described by the Aharonov–Bohm effect [146], as a sum of the electrostatic and magnetostatic potential of the specimen. Assuming that there is an effective way of dealing with the electrostatic component (by flipping over the sample, for instance), the phase shift of the electron due to magnetostatic

potential in a magnetic sample can be directly measured from the hologram. Hence, we can obtain a quantitative map of the sample's magnetic induction [147].

To generate an off-axis electron hologram, a dc-biased biprism wire is first inserted at the selected area aperture position. Next, one searches for a hole in the sample such that the electron beam can pass undeterred, and then with some prior planning or luck, the magnetic region of interest would be located right next to the hole. The charged biprism causes two waves, the reference wave which travelled through the hole, and the wave through the sample, to overlap at the image plane, which results in an interference pattern (chapter by D Smith in [148]). Holography in magnetic materials is considered a form of Lorentz microscopy because the electron phase shift is due partly to Lorentz deflections. A phase shift of $\pi/50$ is thought to be the typical phase (and therefore magnetic) sensitivity of this technique. This is equivalent to being able to sense the presence of a 20 nm diameter nickel structure that is 3 nm thick. The use of a C_s corrected microscope was shown to further improve phase sensitivity [149] and a recent publication examines ways to improve this sensitivity to $\pi/500$ and beyond [150]. The spatial resolution of off-axis electron holography is about 0.5 nm at best, without aberration correction [151], but with the availability of aberration corrected and monochromated microscopes today, ultimately the resolution is given by the information limit of the microscope which is on the order of 0.1 nm [152, 153]. Many groups have used electron holography to study remanent magnetization of nanostructures. For example, the interaction fields of 8 nm diameter Co nanoparticles were resolved using off-axis holography [154]. Gao *et al* showed with electron holography that stacks of self-assembled Co nanodiscs (18 nm diameter and 5 nm tall) are magnetized within the plane of the disc diameter, but that the magnetization spirals along the stack axis with a periodicity of about 45 nm [155]. Snoeck *et al*, were able to show from their holography data (figure 12) that 30 nm Fe nanocubes, when placed in proximity, strongly interacted with one and can form a collective flux-closure state [156]. The temporal resolution for electron holography, however, is no different from any other TEM method.

Transport of intensity. The transport of intensity equation (TIE) was first proposed for light optics [157] and was later adapted to electron optics [158]. This formalism describes how the intensity of a propagating electron wave is altered by the phase gradient in the plane normal to the electron trajectory. In practice, mathematical phase reconstruction is carried out using a minimum of two images, one under-, and the other over-focused, recorded in Fresnel mode. The TIE method is a linear approximation of a non-linear system and therefore, defocus values must be kept sufficiently small in order for TIE to be valid. Since the phase sensitivity increases with defocus, however, there exists an optimal defocus value that is highly sample specific. Figure 10(*b*) is a Fresnel image of a 30 nm thick, 100 nm CoFeB dot in the vortex state. The vortex is not visible in this image because of the small Δz used to keep the TIE within the valid regime. Figure 10(*c*) is the TIE reconstruction of the magnetic phase shift; the false

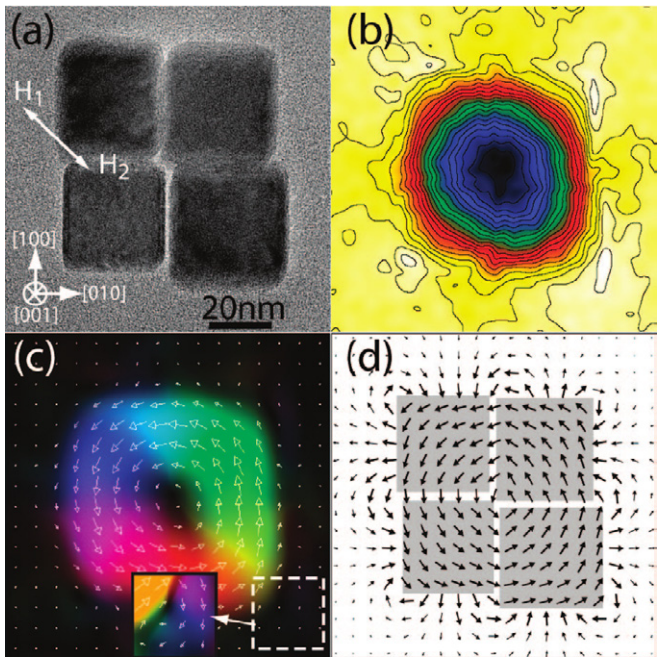

Figure 12. Electron holography and micromagnetic simulations for a square arrangement of four Fe nanocubes. (*a*) TEM micrograph of four 30 nm Fe cubes in a square arrangement. (*b*) Phase image reconstructed from hologram (not shown) corresponding to the magnetic contribution to the phase shift with 0.1 rad contours. (*c*) Vectorial map of the in-plane components of the magnetic induction. (*d*) Micromagnetic simulation of the in-plane induction. (Reprinted with permission from [156], copyright 2008 by American Chemical Society.)

colour gives the magnitude and direction of the magnetization within the film plane. A quasi-interferometric technique, TIE was capable of reproducing electron holography results in non-magnetic test cases [159–161]. As the reconstruction algorithm grows more sophisticated, we expect to see more induction maps of magnetic nanostructures based on the TIE method due to its relative experimental simplicity.

Electron energy-loss magnetic chiral dichroism. Although this is not a Lorentz-based technique, we include this topic in this section due to similarities in hardware requirements. In x-ray magnetic circular dichroism or XMCD (see 4.7.1), left circularly polarized light is absorbed differently from right circularly polarized light by a ferromagnetic specimen. This difference in absorption is the dichroism. In 2006, electron energy-loss magnetic chiral dichroism (EMCD) was demonstrated in an Fe single crystal with unpolarized electrons in a TEM [162]. EMCD simulates the different circular polarizations in x-rays by detector placement (i.e., electron energy-loss spectrometer) at locations where the electron wave functions are de-phased by the specimen due to a specific Bragg condition. EMCD has since been used as a probe for the chemically (and ferromagnetically) ordered L_{21} phase in Co_2MnSi Heusler alloys, and also to study individual magnetic properties of Fe_3O_4 nanoparticles [163]. While this technique is still very new and has seen limited use, it is promising for studying magnetism in epitaxial multilayers. The potentially powerful aspect lies in combining this with high-resolution

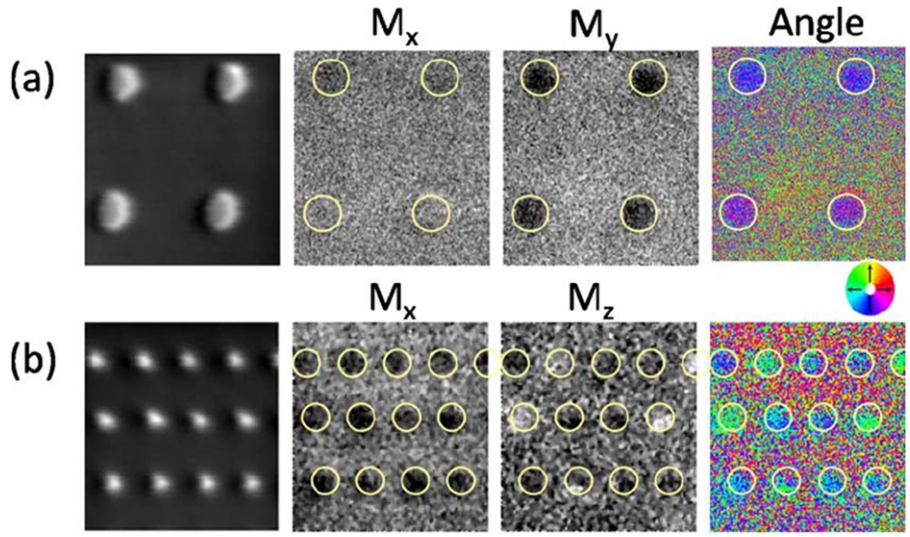

Figure 13. SEMPA images of (*a*) in-plane magnetic states in 90 nm diameter × 10 nm thick discs and (*b*) out-of-plane magnetic states in 35 nm diameter × 65 nm thick discs. Simultaneously measured topography and either two in-plane, or one in-plane and the out-of-plane magnetization components are shown. From these components, (*a*) the in-plane magnetization angle and (*b*) the out-of-plane magnetization tilt angle in the M_x and M_z planes were derived. Note that the out-of-plane magnetic structure has a significant in-plane component which may indicate curling of magnetization near the top surface. (Reprinted with permission from [169], copyright 2010 by the American Physical Society.)

scanning TEM (STEM), where in principle, the d-electrons in transition metals may be probed on the atomic scale.

Non-Lorentz electron microscopy. Non-Lorentz based magnetic microscopy generally relies on the asymmetry between the majority and minority spins at the Fermi energy in the magnetic material to generate contrast. Depending on the technique, the probe consists of unpolarized electrons (as seen in EMCD) or spin-polarized electrons as we will see in spin-polarized low energy electron microscopy SP-LEEM.

Scanning electron microscopy using polarized electrons. Because incident electrons can eject secondary electrons near the Fermi level of a ferromagnetic sample, the magnetization at the surface can be inferred from the relative polarization of the ejected secondary electrons [164–166]. Scanning electron microscopy with polarization analysis (SEMPA), also called spin-SEM, is an SEM technique that images surface magnetization directly by collecting the ejected secondary electrons and measuring their spin polarization with a Mott detector [167, 168]. Any two components of the electron polarization vector may be determined in a single scan by measuring the electrons' asymmetric angular distribution. Thus, each scan simultaneously provides one secondary electron image and two vector component images of the surface magnetization. The spatial resolution of SEMPA is typically about 20 nm, whereas the temporal resolution is on the order of a second. In a recent publication, SEMPA clearly resolved magnetization in sub-100 nm discs (figure 13) of various heights and diameters, confirming the calculations from their phase diagram of magnetic nanodiscs [169].

Spin-polarized low-energy electron microscopy. In SP-LEEM, the sample is excited by electrons and the magnetic information is imparted by the ejected electrons. Unlike SEMPA, however, the incident electron energies are much lower (between 1 and 100 eV). As a result, primarily back-scattered electrons are ejected, and of those electrons ejected, the inelastic mean-free-path is spin dependent [170]. In addition, the incident electrons are spin polarized, usually with a GaAs cathode. The magnetic contrast comes from local differences in the interaction between the incident polarized electrons and the spin-polarized electrons in the various regions of the magnetic sample [171]. Because the images in LEEM are formed by diffracted beams selected at the microscope's BFP, crystallinity directly correlates with image contrast. The lateral resolution of SP-LEEM is on the order of 10 nm, while the temporal resolution is no different from all the others mentioned so far.

SP-LEEM is a proven tool for studying *in situ* spin-reorientation as during layer-by-layer growth on single crystal substrates. For example, it was demonstrated in the growth of Ni film on Cu (0 0 1) substrate, that the magnetization remains primarily in-plane during the first seven monolayers of Ni deposition, but switches to perpendicular magnetization between the seventh and the tenth monolayer, as shown in figure 14 [172]. Spin-reorientation transition was also studied extensively in Co films grown on various substrates (see [173] and the references therein).

Photo-emission electron microscopy. Using many of the same electron optics as SP-LEEM, photo-emission electron microscopy (PEEM) was developed by the same group at Lawrence Berkeley National Laboratory in the 1980s. Instead of an electron source, however, the incident radiation is circularly polarized x-rays, and the outcome is the photo-emission of secondary electrons from the sample. Detailed discussion on PEEM may be found in [174, 175], but briefly, contrast comes from the asymmetric absorption of circularly polarized x-ray by spin-up and spin-down

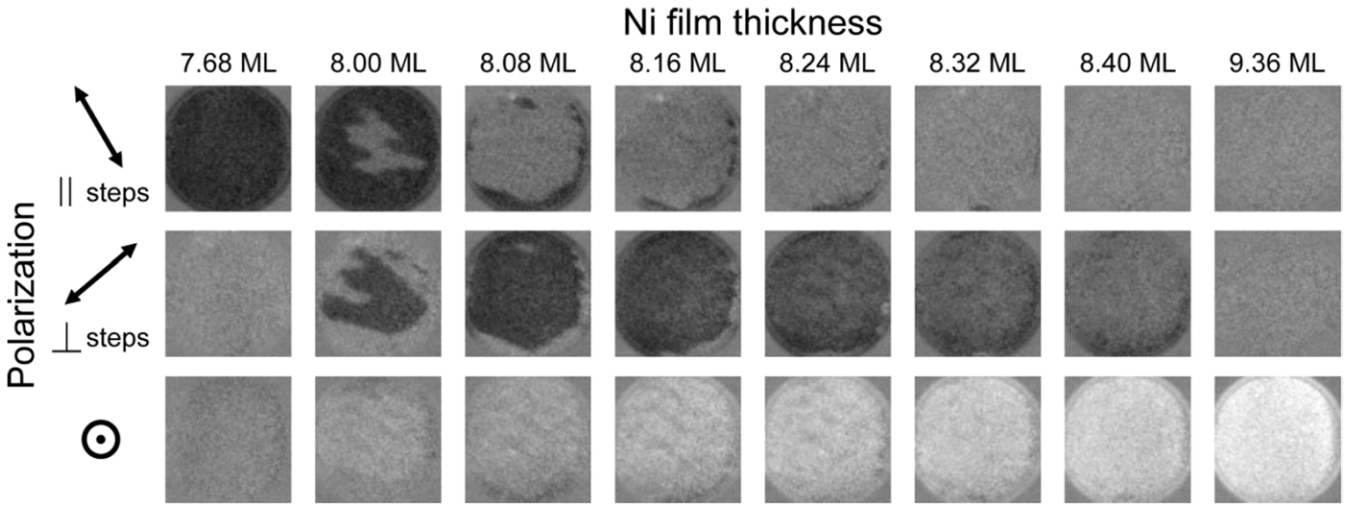

Figure 14. SP-LEEM images showing the thickness-dependent spin-reorientation transition in Ni films grown on a stepped Cu(1 0 0) crystal; grey level in the corners corresponds to zero magnetic contrast, whereas lighter or darker areas represent non-vanishing magnetic signals. Polarization direction of the illuminating beam is indicated along the left side of the figure. Magnetization is found to be in-plane and parallel to substrate steps up to 7.7 ML. At 8 ML, nucleation of domains with in-plane component perpendicular to Cu steps is observed, together with the appearance of out-of-plane contrast. With increasing thickness, out-of-plane contrast increases continuously until the film is completely magnetized perpendicular to the surface at 9.4 ML. The field of view is 7 μm and electron energy is 9.5 eV [172].

electrons. At present, PEEM's spatial resolution is about 50 nm. However, since synchrotrons are pulsed sources, pump–probe and therefore time-resolved magnetic imaging may be accomplished in PEEM with temporal resolution below 100 ps. Magnetization dynamics have been recorded with time-resolved PEEM [172, 176–178]. With the eventual improvement of the spatial resolution, we expect that PEEM will have an even more prominent role in magnetic characterization because it would be possible to spatially and temporally resolve the magnetization of individual magnetic nanostructures with relative ease of sample preparation.

3.2.2. Scanning probe. Magnetic force microscopy (MFM) is a variation of conventional non-contact atomic force microscopy (AFM). The cantilevers used in MFM are either coated with a ferromagnetic [179] or a superparamagnetic material [180, 181]. The stray field generated from the sample couples with the magnetic coating of the cantilever via the magnetostatic interaction. When used in tapping mode, this magnetostatic 'force' induces a phase shift of the cantilever resonance if the driving frequency is held constant (the most common mode of operation). By scanning the tip at a fixed height above the surface and measuring the phase of the cantilever, an image of the magnetic domain structure is formed. Several review papers including [179, 182] provide the details of the tip/sample interaction and the specific details of the measurement.

Because of the geometry of the cantilever tip (i.e. the shape favours it to be magnetized perpendicular to the sample surface), conventional cantilever tips are most sensitive to perpendicular fields generated from the sample. As a result, samples with an in-plane magnetic configuration will show only magnetic contrast at a domain wall where the magnetization partially or fully rotates out-of-plane. MFM images of domain walls in patterned $Ni_{80}Fe_{20}$ structures are shown in figure 2(*a*). This limitation can be overcome by the use of specially fabricated cantilevers whereby a magnetically hard sphere is attached to the tip that is magnetized in a manner parallel to the sample surface. Perpendicularly magnetized samples, however, exhibit more direct imaging of the magnetic configuration using conventional MFM tips. A dense array of 50 nm diameter perpendicularly magnetized Co/Pd nanodots with a centre-to-centre spacing of 100 nm is shown in figure 2. The magnetic state of each nanostructure is clearly determined in this case.

The advantage of MFM is that it is relatively easy to perform at a basic level and most commercial AFMs can be used. A magnetic resolution of ≈25 nm in perpendicularly magnetized samples is rather straightforward to achieve using commercially available MFM cantilevers. With this said, however, more quantitative measurement of properties and dipolar fields can quickly become a very challenging task.

One significant artefact of MFM lies in the field generated by the magnetic cantilever tip itself. In magnetically soft materials, this field can be of sufficient amplitude to change the magnetic state of the sample entirely. This effect can be minimized using a tip with a lower magnetic moment. In addition, the use of superparamagnetic tips further decreases the influence of the tip on the sample and has been shown to improve resolution [180, 181]. However, in both these cases, the interaction strength is also significantly reduced which results in decreased SNR. The contrast can be dramatically increased by over an order of magnitude by performing MFM in vacuum. This results from the 2 to 3 order-of-magnitude increase in the quality factor of the cantilever resonance, resulting in increased sensitivity of small forces acting on the tip.

Generally speaking, increased contrast and SNR in MFM come from larger moments of both the tip and the sample, increased amplitude of the cantilever oscillation, and by decreasing the distance between the tip and sample. However,

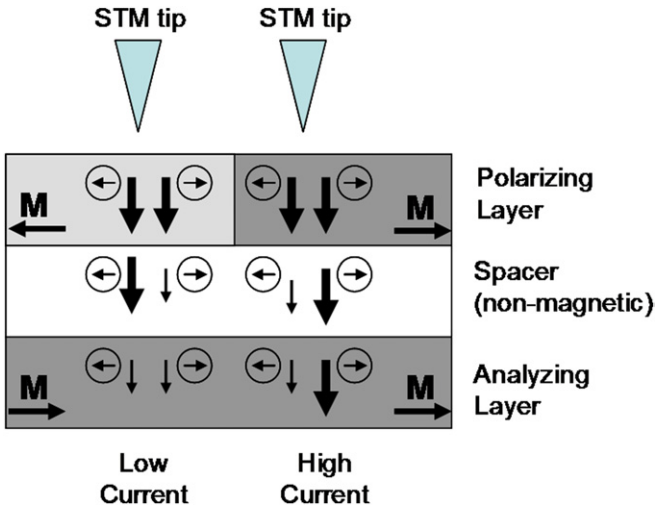

Figure 15. Basic principle of BEMM.

decreasing the distance between the tip and the sample requires a decrease in the amplitude to prevent contact of the tip and the sample surface. Resolution, however, is generally increased by decreasing the size of the magnetic tip (resulting in a lower magnetic moment) [183, 184] and decreasing the distance between the tip and the sample surface (necessitating a decrease in the amplitude of the cantilever oscillation). As a result, there is always a trade-off between contrast and resolution that must be optimized depending on the specific sample and the information needed to be obtained from the measurement.

Another scanning probe technique worth discussing is ballistic electron magnetic microscopy (BEMM), which is a variation of scanning tunnelling microscopy (STM). BEMM, was recently developed to study the magnetic structure of multilayer thin film devices such as GMR or TMR [185–187]. Figure 15 shows a schematic diagram of the basic principles this technique uses to obtain magnetic contrast. A STM tip is brought to within several tenths of nanometres of the surface being imaged. The STM tip is then biased to inject ballistic electrons into the sample. Two magnetic layers separated by a non-magnetic spacer layer (a spin-valve structure, for example) deposited on a semiconductor substrate are required in the sample structure for this technique. The top magnetic layer or 'spin-filtering' layer allows electrons whose spins are parallel to its magnetization to pass through with little scattering. Those electrons with antiparallel alignment undergo increased scattering, and upon scattering, no longer travel at ballistic energies. As a result, a spin-polarized current (all electrons' spins are oriented in a parallel manner) is generated in the spacer layer. As the spin-polarized ballistic electrons enter the analysing layer (lower magnetic layer in figure 15), the electrons undergo the same spin-dependent scattering process. Therefore, parallel alignment of the magnetization will result in a relatively high ballistic electron current and antiparallel alignment will result in reduced ballistic electron current. The current injected into the semiconductor substrate is then measured and relative intensities of this current are proportional to the relative orientation of the magnetization between the two magnetic layers.

A Schottky barrier formed between the analysing layer and the semiconductor substrate ensures that only ballistic electrons reach the semiconductor as lower energy conduction electrons will not have enough energy to overcome the Schottky barrier. It is estimated that approximately 10% of the injected current from the STM tip reaches the semiconductor without undergoing scattering. An image of the surface is then generated by scanning the STM tip across the surface while measuring the current. The advantage of this technique is that resolution is not limited by the long range magnetic interaction, but by the very short range tunnelling current. However, only very specific samples that can be tedious to fabricate can be explored with BEMM.

4. Spin dynamics in nanostructures: high-frequency metrology

In this section we review the current measurement approaches for spin dynamics in sub-100 nm structures. Achieving such capability presents significant challenges and is an active area of research in its own right. This section will largely focus on the problems that need to be addressed for more practical technological applications and how such measurements can be used to study the magnetic properties of nanostructures. In addition, we will show that many properties can be more easily studied with a dynamical approach as opposed to a 'static' measurement. For example, the exchange interaction in many systems prevents small defects (regions of modified magnetic properties) from being isolated from the surrounding material. As such, direct static magnetometry of such defects is extremely difficult. However, a spectroscopic approach offers an alternate means to probe the magnetic properties at small length scales. Several books and papers review in more detail the physics and theory of spin dynamics. As a result, we will only briefly touch upon these concepts as they directly relate to nanostructure metrology. We begin by providing a brief overview of the theory needed in providing a framework to understand spin dynamics in nanostructures. Emphasis will be on more relevant equations and theory needed for more practical experimental work related to the metrology of magnetic nanostructures rather than a more generalized theory.

4.1. Dynamic susceptibility and the equation of motion

Up until this point, we have treated the magnetization as a fixed vector quantity. In reality, in response to a perturbation, the magnetization precesses in time which is typically described by the *classical* Landau–Lifshitz–Gilbert (LLG) equation of motion:

$$\frac{\mathrm{d}\boldsymbol{M}(t)}{\mathrm{d}t} = \gamma\mu_0\left[(\boldsymbol{M}(t)\times\boldsymbol{H}_{\mathrm{eff}}(t)) + \frac{\alpha}{M_{\mathrm{s}}}\left(\boldsymbol{M}(t)\times\frac{\mathrm{d}\boldsymbol{M}(t)}{\mathrm{d}t}\right)\right], \quad (3)$$

where $\gamma = g\mu_{\mathrm{B}}/\hbar$ is the gyromagnetic ratio, g is the spectroscopic splitting factor, μ_{B} is the Bohr magneton, $\mu_0 = 4\pi \times 10^{-7}$ is the permeability of free space, and α is the damping parameter. The effective field H_{eff} includes all the

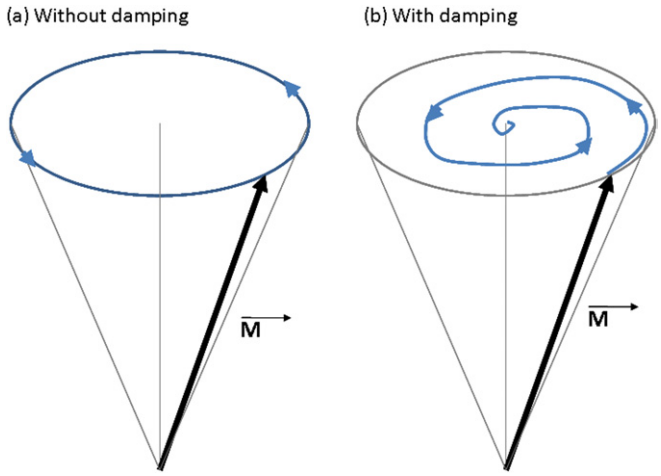

Figure 16. Schematic diagram showing the precession of the magnetization as given by the LLG equation (*a*) without and (*b*) with the damping term.

relevant interaction fields, such as the Zeeman field, exchange field, demagnetization field and anisotropy fields.

The first term on the right describes the precession of the magnetization. With only this term, the magnetization would precess indefinitely as demonstrated in figure 16. The second term on the right describes the damping or energy dissipation of the magnetization. As demonstrated in figure 16, this causes the magnetization to spiral into the applied field axis in the absence of an external driving force. As we will see later, the damping term gives rise to finite linewidths of the resonance.

The susceptibility tensor $\overleftrightarrow{\chi}$ relates the response of the magnetization $\boldsymbol{M}$ to an applied field $\boldsymbol{H}$ by $\boldsymbol{M} = \overleftrightarrow{\chi}\boldsymbol{H}$. The dynamic response of a magnetic system to an externally applied high-frequency field can be described by the Polder susceptibility tensor derived from equation (3) [104, 188] and, the C E Patton chapter in [189]. In many high-frequency measurements of the magnetization, the susceptibility is in fact the physical quantity being measured. The form of the Polder susceptibility tensor is dependent on the measurement geometry, sample and measurement parameters. It is useful to explore the Polder susceptibility by focusing on the experimentally useful case where the RF-field is perpendicular to a static (bias) field H, which is of sufficient strength to saturate the magnetization. We also assume a uniaxial anisotropy field H_k oriented along the static field direction. We define a coordinate system whereby the external static field is along the z-axis and the RF-field is along the y-axis. We assume the sample is an ellipsoid with an intrinsic uniaxial anisotropy field H_k oriented along the z-axis. At small amplitude excitations, the magnetization along the z-axis is approximately equal to M_s, and therefore the magnetization M and the effective field H_{eff} become,

$$\boldsymbol{M}(\boldsymbol{t}) = m_x(t)\hat{x} + m_y(t)\hat{y} + M_s\hat{z} \tag{4}$$

$$\boldsymbol{H}_{\text{eff}}(\boldsymbol{t}) = [h_x(t) - N_{xx}m_x(t)]\hat{x} + [h_y(t) - N_{yy}m_y(t)]\hat{y} + [H + H_k - N_{zz}M_s]\hat{z} \tag{5}$$

where, $m_{x,y}(t)$ and $h_{x,y}(t)$ are the time varying components of the magnetization and RF-field along the x- and y-axes and M_s is the saturation magnetization, $N_{xx,yy,zz}$ are the respective demagnetization factors. The assumption of an ellipsoidal shape and the choice of a symmetric geometry are expressed in equation (5) since the demagnetization tensor of an ellipsoid contains only the diagonal elements, $N_{xx,yy,zz}$, which add to unity (i.e. $N_{xx} + N_{yy} + N_{zz} = 1$).

Assuming that the time varying components have the form $e^{-ift/2\pi}$, the above expressions are inserted into equation (3). Neglecting quadratic and higher order terms in $m_{x,y}(t)$ and $h_{x,y}(t)$, the susceptibility for an ellipsoid becomes [104]

$$\chi(f) = \frac{\left(\frac{\gamma\mu_0 M_s}{2\pi}\right)}{f_0^2 - f^2 - if\Delta f/2} \times \begin{bmatrix} (1+\alpha^2)f_y + i\alpha f & -if \\ if & (1+\alpha^2)f_x + i\alpha f \end{bmatrix} \tag{6}$$

where

$$f_{x,y} = \frac{\gamma\mu_0 H_{x,y}}{2\pi} \tag{7}$$

and stiffness fields,

$$H_{x,y} = H + H_k + (N_{xx,yy} - N_{zz})M_s. \tag{8}$$

The equation for the stiffness fields shows that the demagnetization term $(N_{xx,yy} - N_{zz})M_s$ enters the equation just as the anisotropy does. As a result, the demagnetization term is often referred to as the *shape* anisotropy. In many nanostructures made of soft materials such as $Ni_{80}Fe_{20}$, the intrinsic anisotropy is almost negligible and the shape anisotropy is the dominant term.

The Kittel equation that describes the resonant precession frequency, f_0, is

$$f_0 = \sqrt{(1+\alpha^2)f_x f_y} \approx \sqrt{f_x f_y} \tag{9}$$

with a frequency-swept linewidth of the resonance at full-width half-maximum,

$$\Delta f = \alpha(f_x + f_y). \tag{10}$$

Figure 17 shows an example of a series of frequency-resolved MOKE (FR-MOKE) spectra for an array of 63 nm diameter $Ni_{80}Fe_{20}$ with fits of the susceptibility from (6). A peak in the spectra corresponding to the resonant precession frequency shifts to higher frequency as the applied field is increased as predicted by equation (9).

The approximation shown in equation (9) is almost exclusively used since most often $\alpha \ll 1$. We will see that the resonance frequency and linewidth are some of the most experimentally important and accessible quantities in the study of spin dynamics. Equation (9) shows that the resonance frequency is a strong function of the applied magnetic field H, as well as the sample parameters such as the shape (demagnetization factors), saturation magnetization and anisotropy. In fact, this shows how the sample parameters are typically measured from the field dependence of f_0. In addition, equation (10) shows that linewidth of the resonance is proportional to the damping parameter α, which allows for the determination of the important parameter α.

Two measurement schemes can be used to measure f_0 and the linewidth: (1) the external static magnetic field is held

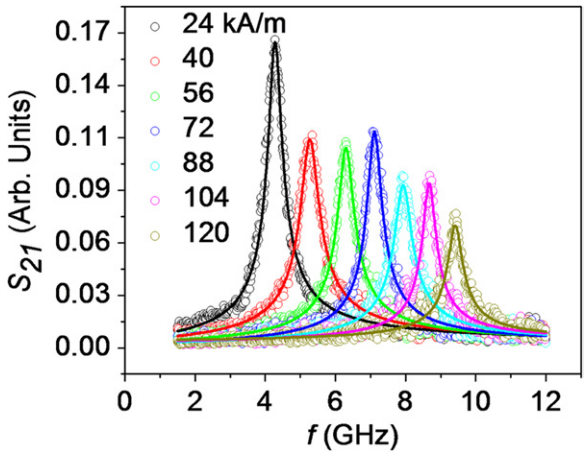

Figure 17. Fits of the Polder susceptibility tensor to FR-MOKE data taken on an array of 65 nm diameter Permalloy nanostructures. (Reprinted with permission from [104], copyright 2007 by the American Institute of Physics.)

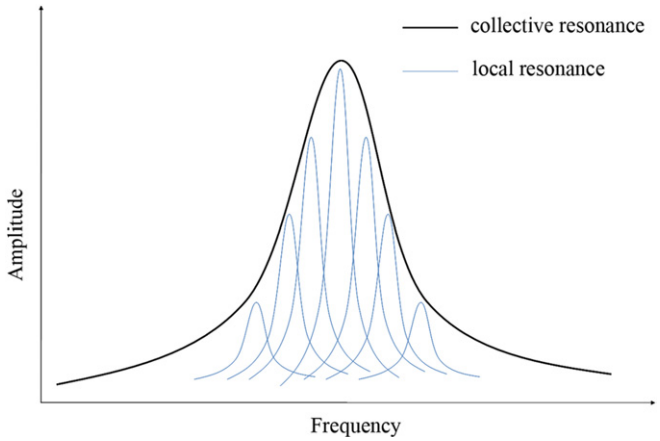

Figure 18. Schematic diagram showing the increased measured collective FMR linewidth due to a distribution of local resonance frequencies.

constant and the frequency is varied, the so-called *frequency-swept* method; or (2) the frequency is held constant and the field is varied, the so-called *field-swept* method. The frequency-swept linewidth Δf can be related to the field-swept linewidth ΔH by (11).

$$\Delta H = \frac{\Delta f}{\left(\frac{\partial f_0}{\partial H}\right)}. \tag{11}$$

The field-swept linewidth becomes

$$\Delta H = \frac{4\pi\alpha}{\gamma\mu_0} f_0. \tag{12}$$

As with Δf, the field-swept linewidth ΔH is also proportional to α when $\alpha \ll 1$ (i.e. when $f_0 \neq f(\alpha)$). Equation (12) assumes that the dissipation of energy (damping) is a strictly intrinsic mechanism. However, inhomogeneity of the sample can also give rise to increased linewidth and energy dissipation. This can be understood by considering a distribution of local resonance frequencies as depicted in figure 18, which collectively result in a larger total linewidth than would be expected for a given value of α. Phenomenologically, it was found that the inhomogeneous linewidth broadening, ΔH_0, could be separated from α from the frequency dependence of ΔH by (13), which more accurately describes the linewidth behaviour in realistic systems [190–192]:

$$\Delta H(f_0) = \Delta H_0 + \frac{4\pi\alpha}{\gamma\mu_0} f_0. \tag{13}$$

Other extrinsic contributions to the linewidth include low-field loss [193] and 2-magnon and 3-magnon scattering [190, 194]. Low-field losses can occur when the applied field is not of sufficient strength to fully align the magnetization everywhere in the sample. For example, ripple domains can cause inhomogeneity in the magnetization at low fields [195]. This effect therefore vanishes as the field is increased to a sufficient strength to fully saturate the sample. The effects of low-field losses should diminish in nanostructures, especially when the size of the structure approaches the exchange length keeping the magnetization uniform.

In order to understand 2- and 3-magnon scattering we first need to be familiar with the concept of a spinwave or magnon. The above discussion focuses on the case of uniform precession (where the wavevector $k = 0$ and/or standing wave modes exist in patterned structures). Spinwaves can also exist as a travelling wave where there is a non-zero phase relationship between neighbouring spins. 2-magnon scattering occurs when a magnon is scattered by a defect in the sample [196–199], 3-magnon scattering occurs when the spinwave bands in the dispersion curve allow for spinwaves to scatter, creating or annihilating spinwaves or modes [200]. Conservation of energy and magnon wavevector (momentum) is required for 3-magnon scattering but not necessarily for 2-magnon scattering where momentum can be transferred to the defect. These processes occur even for the uniform precession $k = 0$ mode as it scatters to create $k \neq 0$ modes. In nanostructures, travelling spinwaves do not occur, but as we will see later, the normal modes have Fourier components that give rise to $k \neq 0$ components of the wavevector. 4-magnon scattering is similar to 3-magnon scattering except that three magnons are created from the scattering process instead of two [201]. However, the effect of 3- and 4-magnon scattering should be almost non-existent in sub-100 nm nanostructures since there is no longer a continuous band of spinwave (magnon) states that are accessible, and thus, the conservation rules exclude most scattering events. Similarly, the probability of a 2-magnon scattering event will be reduced in nanostructures since there are a small number of defects in a nanostructure and a lack of magnon states to scatter into.

For most nanostructures created in the laboratory or of practical use in technology, the shape of the elements will not be a true ellipsoid. However, the above analysis still serves as a useful approximation for many lithographically fabricated nanostructures. In this case, the demagnetization factors are replaced by the *effective* demagnetization factors $N'_{xx,yy,zz}$, which do not necessarily or strictly add to unity. As a test of this analysis, we see that the Kittel equation for an infinite thin film

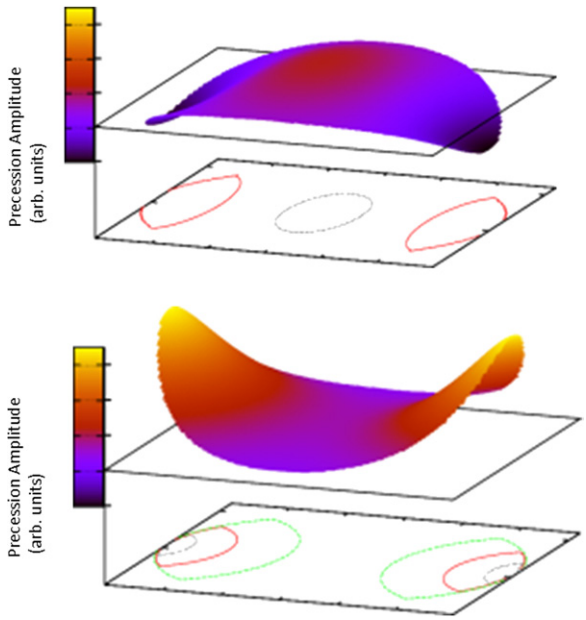

Figure 19. Example of two normal modes in 100 nm diameter elliptical structures [208].

with a surface normal along the x-axis is recovered (i.e. when $N_{xx} = 1$, $N_{yy} = N_{zz} = 0$). Other examples of susceptibility tensors derived for other measurement and sample geometries, and sample anisotropies, can be found in the literature, such as [202].

For uniform precession of the magnetization in an object, the demagnetization factors are determined by the physical shape of magnetic objects. However, in nanostructures, the boundary conditions and confinement of the magnetization result in the precession being described by a series of eigenmodes or *normal modes* of the system [203–207]. Figure 19 shows examples of the normal modes found in 100 nm $Ni_{80}Fe_{20}$ nanostructures obtained from micromagnetic simulations. The effective demagnetization factors in equation (8) will therefore vary for each normal mode of the system since the confinement or 'shape' of the normal mode does not encompass the entire structure. In other words, the demagnetization factors for the normal modes are not determined solely by the shape of nanostructure, but also have to take into account the 'shape' of the eigenmode within the nanostructure. As a result, numerical methods, such as micromagnetic simulations, can be used to determine the demagnetization factors for each mode. Experimentally, they can be determined by fitting the field dependence of f_0 to equation (9).

Now that we have established a foundation for understanding some of the physics of spin dynamics in nanostructures, we address the question of how such measurements can be achieved. New techniques and approaches must be implemented for the study of nanostructures since their small size (and volume) severely decreases the SNR relative to bulk or thin film techniques. Several measurement approaches are currently in use and are being explored for studying magnetic nanostructures; metrology of magnetic nanostructures is in itself an active area of research.

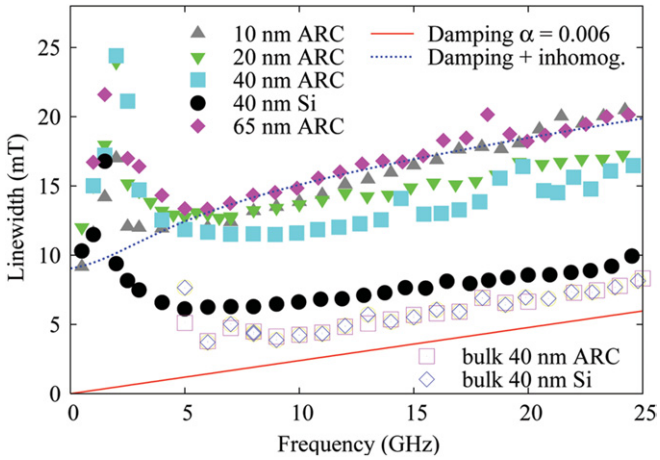

Figure 20. Edge mode resonance linewidths (filled symbols) as a function of frequency. Edge mode linewidth is significantly lower for the stripes on Si versus those deposited on an anti-reflective coating (ARC). Bulk mode linewidths (open symbols) for the 40 nm thick films are shown for comparison. The solid line is the intrinsic linewidth predicted for a Gilbert damping parameter $\alpha = 0.006$; the dotted line includes an inhomogeneous broadening expected for a 3.7 T standard deviation of H_{sat}. (Reprinted with permission from [212], copyright 2008 by the American Institute of Physics.)

4.2. Ferromagnetic resonance

The first FMR experiments were performed using a microwave resonant cavity placed inside a magnet [209]. The microwave absorption of the sample is measured as the magnetic field is swept through the FMR resonance. Cavity based FMR does not lend itself well to the study of nanostructures since the cavity is of macroscopic dimensions providing significant challenges in obtaining sufficient SNR and the inability to isolate signals from different nanostructures on a particular sample. However, cavity based FMR has been demonstrated in dense arrays of nanostructures [210, 211].

Inductive FMR techniques rely on delivering microwaves from either a stripline or a co-planar waveguide (CPW) and measuring the absorption of the sample either by the transmitted or reflected power. In these cases the magnetic response of the material is inductively coupled to the stripline or CPW. One advantage of such a technique is that the frequency can be varied over a large range, facilitating linewidth analysis via (13) with a single microwave source.

Inductive based FMR was applied recently to characterize edge properties in 450–480 nm wide $Ni_{80}Fe_{20}$ stripes [212]. In this example, large arrays of such structures were fabricated and placed face-down on a CPW. A microwave signal generator was used to apply microwaves to the CPW and the transmitted power through the CPW was measured with a diode [213]. One of the normal mode's amplitudes in this system was concentrated at the edge region, which was used to probe the effect various processing conditions had on the edge properties. Figure 20 [212] shows how the linewidth of the edge mode varies considerably depending on the underlayer used during deposition and the thickness of the material. Of importance is the fact that the increase in linewidth corresponds to additional offset, which by equation (13) indicates an increase in the inhomogeneous contribution.

Another inductive FMR technique that has obtained much popularity in recent years is vector network analyser FMR (VNA-FMR) [214, 215]. A stripline or CPW is connected to the ports of the VNA and the transmission (S_{21}) or reflection (S_{11}) parameters are measured. With VNA-FMR, the phase of the inductive coupling is also preserved in addition to the power. As a result, with a well-calibrated VNA-FMR, both the real and imaginary parts of the dynamic susceptibility can be measured.

Most striplines and CPWs used for FMR have a centre conductor that is of macroscopic dimensions ranging from 100 μm to a few millimetres. This allows for arbitrary samples to be placed face down on the waveguide and easily measured. Because of these dimensions, however, large arrays of nanostructure are still needed. Such limitations can be overcome by fabricating individual nanostructures on microscopic CPW which is itself fabricated on the sample. With such an approach, using inductive FMR measurements, individual sub-micrometre features have been measured [216, 217].

4.3. Magneto-optic techniques

MOKE was previously shown for use in static magnetometry of nanostructures where the polarization of the reflected light can be related to the magnetization. This effect is also useful for probing the dynamic properties. With the availability of ultra-fast lasers and photodiodes, MOKE can be used to measure the dynamic response of a small magnetic system. There are generally two approaches to dynamic measurements that exploit MOKE; measurements in the time-domain, and measurements in the frequency-domain. Both of these approaches have advantages and disadvantages depending on the particular measurement of interest and the sample of interest. Since the experimental setup is different for these two approaches, we will provide an overview to each of them individually.

4.3.1. Time-resolved MOKE. While there are many variations of time-resolved MOKE (TR-MOKE), the basic principle of these techniques is that of exciting the sample with a pulse of energy, and measuring the magnetic response of the system as a function of the time following the initial excitation via MOKE. With the availability of femtosecond pulsed lasers, optical time-domain dynamic measurements have gained popularity in the study of magnetodynamics. The ability to focus light to a sub-micrometre spot also allows TR-MOKE to be applied to structured materials.

The excitation of the sample is typically generated either by an ultra-fast field pulse delivered by a waveguide structure (CPW or stripline) [218, 219], or optically by the use of a high-intensity ultra-fast pulse of light generated by a femtosecond laser, the so-called pump–probe method [220, 221]. The most common approach delivers an excitation pulse through a waveguide structure. In the first of these excitation schemes, the pulse is typically delivered by means of a pulse generator that is electronically synchronized to the laser pulse or by the use of a photo-conductive Auston switch fabricated on the sample or a photodiode, which is activated by the laser pulse itself [222–225]. In the all optical pump–probe excitation method, a focused high-intensity laser pulse is used to heat the sample at the time scale of the pulse width (typically < 1 ps). Because of the temperature dependence of the magnetic properties, the demagnetization field causes the magnetic moment to experience an ultra-fast 'kick' or a change in magnetic configuration, which sets the magnetization precession in motion as it recovers to its room temperature equilibrium state.

The magnetic response of the system is then detected by a pulsed probe beam via the MOKE. An ultra-fast optical pulsed beam from the laser is used to probe the magnetic state at an instant in time following the excitation. Regardless of the excitation scheme used, a delay line is needed to separate the excitation pulse in time from the probe beam. This is achieved either electronically or by varying the optical path length in the pump–probe method. By synchronizing the excitation pulse to a delayed probe pulse, a snapshot of the magnetization is measured at a specific delay time after the excitation. In the case of the pump–probe method, the probe beam is sufficiently low in intensity (compared with the pump beam) to prevent it from changing the magnetic state of the system. This process can then be repeated for a series of delay times. Figure 21 shows plots of the MOKE signal as a function of the delay time for 150 nm thick Ni pillars. The magnetization undergoes a rapid decrease following the application of the excitation pulse followed by oscillations that damp out at higher delay times. The initial decrease in magnetic signal is due to the ultra-fast demagnetization effects [226]. The damped oscillations following this initial decrease, however, are related to the precession frequency and the damping term in equations (9) and (10). Typically, this time trace is Fourier transformed to generate a quasi-FMR spectrum, an example of which is shown in the right-hand side of figure 21.

TR-MOKE has been successfully demonstrated in measuring individual 50 nm magnetic structures [220, 227]. In this case, ARCs of the sample were needed to increase the SNR [228, 229]. Ultimately, spatial resolution is limited by the diffraction limit of optical light, which is significantly larger than the nanostructure being measured. Thus, sub-structure cannot be directly resolved with this technique. However, a more recent and novel approach to studying the magnetic sub-structure (such as pinning sites) makes use of a vortex core to detect magnetic structure within the material. Here, the vortex gyrotropic motion is measured with conventional TR-MOKE [230]. The vortex can be moved, and therefore scanned, by the application of external static fields. When the vortex interacts with, or becomes pinned by, a defect, the low-amplitude gyrotropic motion and frequency will vary in response. This technique has not yet been demonstrated on nanostructures, but may prove to be a useful technique to probe the nanoscopic magnetic properties in the near future.

An advantage to time-domain measurements is that the evolution of the magnetization in time can be directly studied. Such measurements may be of great importance in studying the fundamentals in ultra-fast demagnetization processes [231] or the dynamic switching [232] and stochastic events.

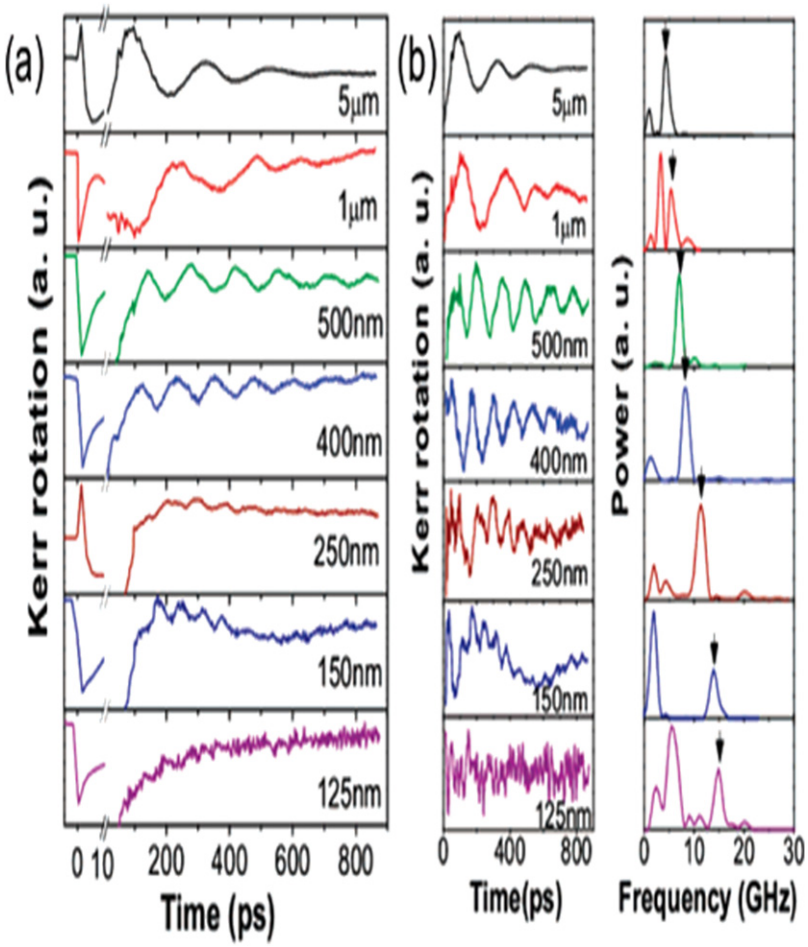

Figure 21. Measurements of the time-resolved Kerr rotation and the corresponding fast Fourier transform (FFT) spectra: (*a*) time-resolved Kerr rotations (raw data) for single magnets of varying diameter at H_{bias} of 13.4 kA m^{-1}. The horizontal scale is broken between 10 and 15 ps to show the three different regions clearly; (*b*) time-resolved Kerr rotations after subtracting a double exponential background (left panels) and FFT spectra (right panels) at H_{bias} of 13.4 kA m^{-1}) with arrows indicating the uniform precession frequencies. (Reprinted with permission from [220], copyright 2006 by the American Chemical Society.)

4.3.2. Frequency resolved-MOKE. A more recently demonstrated technique exploits the MOKE effect in the frequency domain, and is referred to as FR-MOKE. A schematic of the FR-MOKE setup is shown in figure 22 [208]. The sample is placed on a CPW and excited with amplified continuous-wave (CW) microwaves generated from a vector network analyser (VNA). A low noise CW laser is linearly polarized and focused on the sample. Reflected light is collected by a collimating lens, passed through an analyser (linear polarizer) and focused on a broadband photodiode. The precession of the magnetization in response to the applied microwave field results in a modulation of the polarization state of the reflected light via the MOKE. Upon passing the reflected light through an analyser, the modulation in the polarization state becomes an intensity modulation which is measured by the photodiode. The amplified signal from the photodiode is then directed to the input port of the VNA. An S_{21} measurement is then performed by the VNA to measure the response of the magnetic system to the applied microwaves.

Figure 23 shows FR-MOKE spectra taken from a 5 nm $Ni_{80}Fe_{20}$ thin film along with arrays of 50, 100 and 200 nm diameter. The uniform FMR peak is present in the thin film spectra. However, in the 100 and 200 nm patterned structures, two peaks are clearly visible, which correspond to two of the normal modes of the structures. An advantage of FR-MOKE lies in its sufficient SNR allowing for careful evaluation of linewidths in arrays of nanostructures. As an example, figure 24 shows plots of the linewidth ΔH versus f_0 for a 5 nm thick $Ni_{80}Fe_{20}$ thin film as well as 75 and 200 nm diameter nanostructures made from the same material [208]. Fits to (13) are included, which are used to separate ΔH_0 and α. The thin films have a measured $\alpha = 0.1$ and a very small value of $\mu_0 \Delta H_0 = 0.6$ mT, indicative of a high quality and homogeneous film since almost all of the linewidth results from the intrinsic damping. However, when the film is patterned into an array of 75 nm diameter structures, the linewidth increases. Fits to (13) yield an identical value of α to the thin film, but show a large increase in ΔH_0. This data set shows how FR-MOKE reveals that patterning the thin film introduces inhomogeneity into the system. The situation becomes more interesting when slightly larger 200 nm diameter structures are measured. In this case, two of the normal modes are within the frequency range of the system and both have very different linewidth behaviour. One normal mode's precession is confined to the centre of the nanostructure (centre mode,

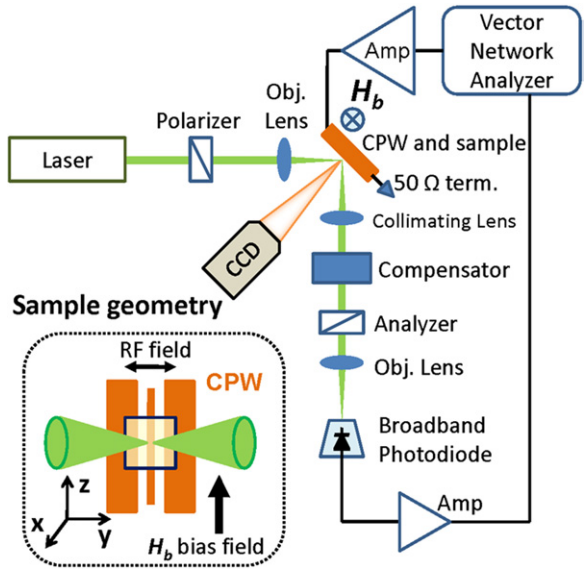

Figure 22. Schematic diagram of the FR-MOKE experimental setup [208].

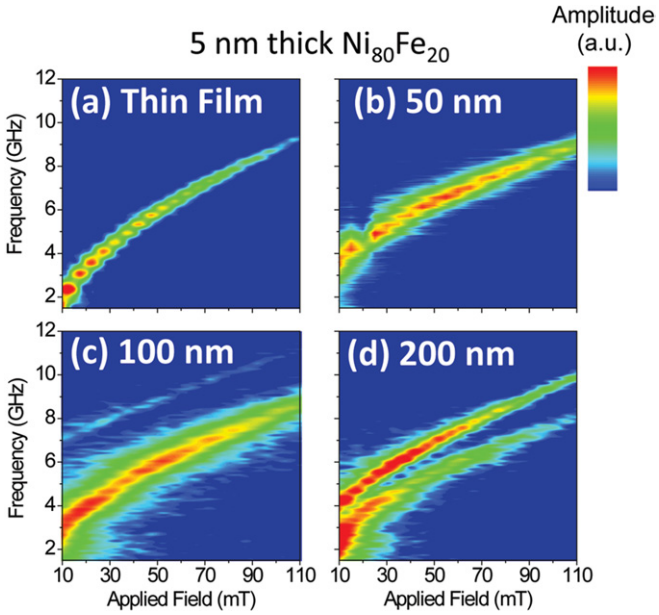

Figure 23. Colour contour plots of spectra for 5 nm thick $Ni_{80}Fe_{20}$ for (*a*) thin film, (*b*) 50 nm diameter, (*c*) 100 nm diameter and (*d*) 200 nm diameter nanomagnet arrays. The colour scale represents the normalized amplitude [208].

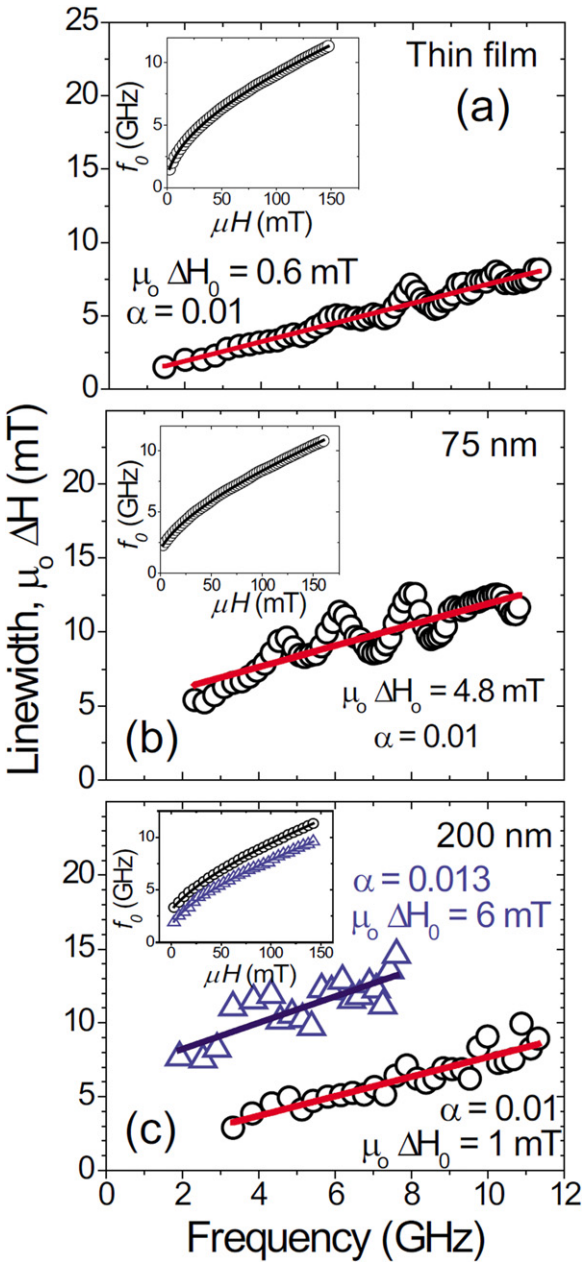

Figure 24. ΔH_0 versus f_0 for the 5 nm thick $Ni_{80}Fe_{20}$ with (*a*) the thin film, (*b*) 75 nm diameter and (*c*) 200 nm diameter arrays. Both the end (△) and centre (○) modes are observed in the 200 nm diameter sample. Fits to (13) are included that were used to separate the contribution of α and ΔH_0 to the total mode linewidth. The insets show the respective Kittel plots used to convert from Δf to ΔH [208].

in black) and the other to the edges of the nanostructure (end mode, in blue). The linewidth behaviour of the centre mode is not so different from that of the thin film. However, the end mode shows a substantial increase in ΔH_0 with little to no effect on the intrinsic damping. This data set indicates that the inhomogeneity introduced during patterning occurs at the edge region of the nanostructures. Through micromagnetic simulations, this increased inhomogeneity at the edges can largely be accounted for by considering small size and shape fluctuations from nanostructure to nanostructure [104, 208].

This discussion serves as more than just an example of the application of FR-MOKE; this demonstrates that by analysing the data from the various normal modes, the magnetic properties at different locations within a nanostructure can be separately evaluated. Thus, despite direct spatial resolution being limited by the optical diffraction limit, to some degree, sub-structure of the magnetic properties can still be resolved, far below the length scale of the spot size. In addition, these studies show how the lithographic uniformity of an ensemble of nanostructures can be assessed spectroscopically while at the same time the material properties can be assessed by separately analysing the different normal modes of the system.

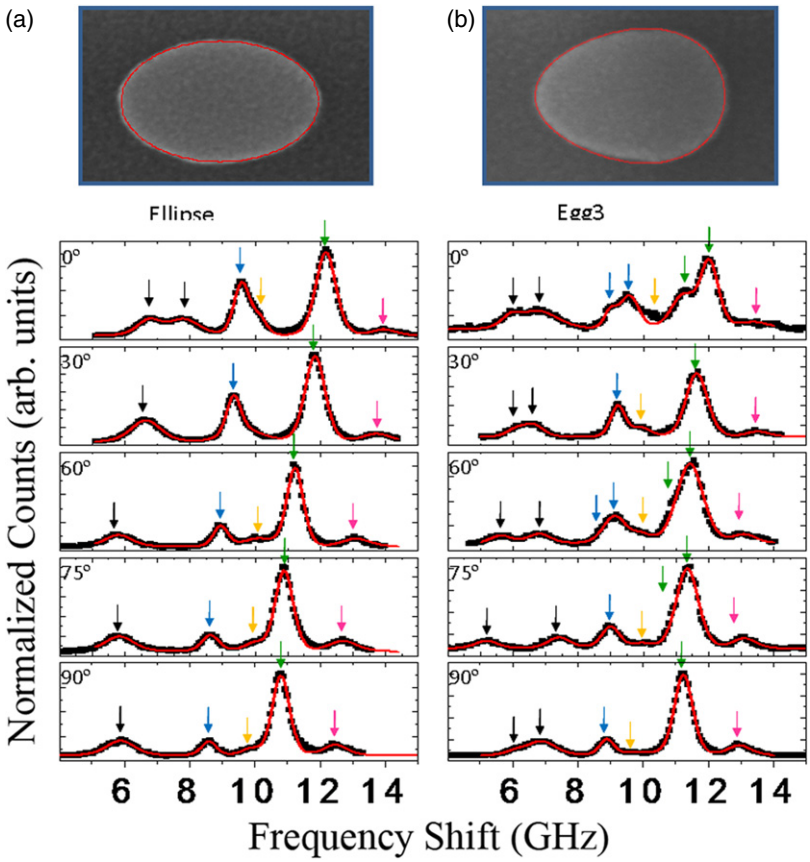

Figure 25. SEM images of 200 nm structures of (*a*) an ellipse and (*b*) a slightly egg-shaped structure. Bottom: BLS spectra taken at various in-plane angles. The different normal modes of the system are indicated by the arrows [241].

4.4. Brillouin light scattering

Brillouin light scattering (BLS) is an optical technique based on the inelastic scattering of mono-energetic photons from spinwaves in a magnetic sample. Analogous to phonons and plasmons, spinwaves (or magnons) are quasi-particles that have both quantum units of energy, $\hbar\omega$, and a wavevector (momentum) k. As a result, a photon can interact with (create or annihilate) a spinwave. Conservation of energy and momentum results in the scattered photon undergoing a change in wavevector and a change in energy (or frequency shift). BLS takes advantage of this phenomenon by interferometrically measuring the frequency shift of the photons that undergo an inelastic scattering event with a spinwave.

BLS makes use of a single frequency laser that is focused onto the sample. The scattered photons are then collected and analysed by a Fabry–Perot interferometer. The scattered photons can either be forward scattered or back-scattered depending on the measurement geometry. However, back-scattering is more common since, in that case, the samples do not have to be transparent. Outside of magnetism, BLS is also very useful in measuring acoustic phonon modes, which can also appear in BLS spectra of magnetic samples. However, by careful consideration of the polarization of the incident laser light and scattered light before it enters the interferometer, the signal obtained by scattering from phonon modes can be suppressed. By varying the scattering geometry (angles of the incident and scattered photons) spinwaves with certain values of k can be selected. The uniform FMR mode (or $k = 0$ spinwave mode) for example, can be measured with BLS with a direct back-scattering geometry [233]. Several more detailed overviews of BLS are to be found in [234–236].

BLS has been successfully used to measure the mode structure in arrays of nanostructures [237–240] As a recent example, figure 25 shows BLS spectra for different applied field directions for an array of 200 nm ideal elliptical structures as well as distorted elliptical structures. The distortion from the ideal elliptical shape comes from introducing a small 'egg-like' shape into the structure [241]. Unlike the thin film, several peaks are present in the spectrum which correspond to the various normal modes of the nanostructure. In fact, the two lowest frequency modes in the spectra are the same end mode (black arrows) and centre mode (blue arrows) measured in figure 24 with FR-MOKE. The end mode for the egg-shape labelled by green arrows splits into two well-separated frequencies, which exceed 2 GHz at some applied field angles. The ideal elliptical arrays, however, do not exhibit such a strong splitting of the mode frequencies.

In this example, BLS with a spot size of approximately 20 μm was used to measure an *array* of nanostructures. However, in order to measure individual structures, a much smaller spot size is needed. Incorporating a high quality objective lens has been shown to produce diffraction-limited spot size approaching 400 nm in micro-BLS systems, similar to what is used in MOKE systems [242–244]. Micro-BLS can be

used in scanning mode to spatially resolve the mode structure within a patterned feature. As with all optical techniques, the direct spatial resolution is dictated by the diffraction limit of light used, which prevents direct imaging of nanostructures.

Recently, the combination of micro-BLS and near-field imaging was demonstrated using a micro-BLS in combination with AFM [245]. Here, an AFM cantilever with a nanoscopic sized aperture was scanned across the sample while the micro-BLS was focused on the back side of the aperture. Since the diameter of the aperture through the cantilever is significantly smaller than the wavelength of light, the aperture acts as a waveguide for the evanescent field. With the cantilever tip within a few nanometres of the surface the light interacts with the sample in the near-field regime, effectively limiting the resolution to the size of the aperture. While not demonstrated on nanostructures directly, this work was successful in achieving ≈85 nm spatial resolution, significantly below the diffraction limit of the light used.

Both micro-BLS and near-field BLS present significant SNR challenges. As a result, the sample is usually pumped with an external microwave field to generate a significantly larger density of spinwaves relative to thermally generated spinwaves. This is achieved by placing the sample on a CPW and applying an RF-field during the measurement. This considerably enhances the SNR in BLS. However, as with other techniques that employ applied microwave fields, non-linear effects may be introduced if the RF-field is of sufficient magnitude. Recall the derivation of (3) assumed small amplitude precession of the magnetization. When this amplitude becomes large, then the small angle approximations to the LLG equation are no longer valid and higher order terms may no longer be negligible.

4.5. Spin-torque ferromagnetic resonance

In many GMR and TMR spin-torque devices, the precession of the magnetization can result from spin-polarized current being driven from one magnetic layer to another, the so-called spin-torque effect. This phenomenon is exploited in spin-torque ferromagnetic resonance (ST-FMR) as a means to directly measure the ferromagnetic resonance properties of the nanopillar through the measurement of the resistance across the device. ST-FMR of course requires fabrication of fully functional GMR or TMR device structures [26, 246–249]. An advantage of ST-FMR is the ability to achieve good SNR on measurements of *individual* nanostructures. In addition, both the device properties and the fundamental properties of the individual magnetic layers of *the same* device can be separately studied.

The typical experimental setup consists of applying a microwave frequency current on top of a small dc current. The microwave frequency current is used to excite the high-frequency response of the system, which when near the resonance frequency results in precession of the magnetic layer. Such magnetic precession results in a change in the average dc resistance of the device from the GMR or TMR effects, which is measured from the dc signal applied to the device.

However, while simple in principle, care must be taken to minimize and take into account the additional artefacts and effects that may arise. For example, the spin-torque effect itself can shift the frequency of precession and influence the linewidth since the spin-torque effect acts as negative damping on the system. In addition, the application of currents through the nanopillar can introduce significant Oersted fields, potentially influencing the precession frequency and mode structure. GMR and TMR devices also consist of more than one magnetic layer. This measurement is highly dependent on the relative magnetic orientations of the layers as well as the direction of the applied magnetic field. Thus, careful consideration of the experimental geometry must be taken. The ST-FMR spectrum can also be complicated by the presence of multiple peaks coming from the various layers in the device structure. As a result of these factors, the analysis of ST-FMR data can become more challenging and careful consideration of various artefacts of the measurements must be taken into account in order to obtain accurate values of physical properties. However, with careful consideration of the measurement and analysis, ST-FMR proved a valuable tool in the study of nanostructures and spin-torque phenomena.

4.6. Scanning probe techniques

Magnetic resonance force microscopy (MRFM), or more specifically ferromagnetic resonance force microscopy (FMRFM) when applied to ferromagnets, shows much promise to image individual nanostructures and even sub-structure within a nanostructure [250–252]. FMRFM takes advantage of the same principles used in MFM whereby a magnetic cantilever tip experiences and responds to the magnetic force exerted by the stray field of the sample. In FMRFM, however, the samples are excited by a microwave field (generated, for example, by a stripline or CPW). In addition, a static field is applied to the sample, which comprises both the field generated by an external magnet and the stray field of the magnetic cantilever. Generally, the external static field is strong enough to saturate the sample in an out-of-plane orientation. When the static field is at a ferromagnetic resonance condition, the time averaged out-of-plane magnetization will be slightly reduced relative to the non-resonance condition as a result of the finite precession angle of the magnetization. This small change of the time averaged magnetization can then be detected by a change in the deflection of the cantilever. The signal can be significantly enhanced by modulating the microwave field amplitude at the cantilever frequency (tens of kilohertz).

The stray field generated by the tip, however, induces a non-uniform magnetic field on the nanostructure. Since the total external applied field includes the field from both the magnetic cantilever and the applied static field, a field gradient caused by the tip will cause only a small volume of the sample to be at the resonance condition. Thus, the dynamics of the nanostructure itself (how it would behave in a device or a bit in BPM) cannot be directly measured since the normal modes of the system will be distorted by

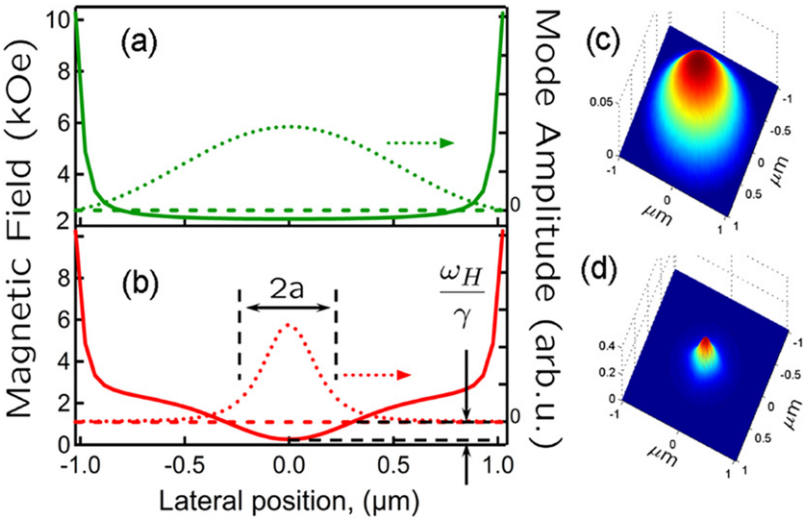

Figure 26. Numerically calculated spatial profile of transverse precession magnetization for the first order FMR mode excited in a 2 m diameter, 50 nm thick $Ni_{80}Fe_{20}$ disc ($4\pi M_s = 1.1$ T, $B_{ext} = 1.3$ T) in (*a*) a uniform external field and (*b*) in the presence of the field from a 1 m diameter spherical magnet ($4\pi M_s = 1.1$ T) located 250 nm above the centre of the disk. The magnetic moment of the probe magnet *m* is antiparallel to H_{ext}. The mode is confined to the region of reduced field beneath the probe. The dotted line shows the mode amplitude along a line through the centre of the dot; the corresponding magnitude of the total magnetic field H_{tot} is shown with a solid line; the dashed line indicates the resonance field H_{res} of the mode. (*c*) and (*d*) are the corresponding 2D maps of the transverse precession magnetization. (Reprinted with permission from [251], copyright 2008 by the American Physical Society.)

the non-uniform field. Figure 26 shows simulated data of the internal field and resonance amplitude in a 50 nm thick, 2 μm diameter $Ni_{80}Fe_{20}$ structure [251]. The excited mode profile is significantly different in the presence of the field gradient induced by the tip versus the simulation in a uniform field.

However, the field gradient induced by the tip and the increased confinement of the resonating volume can be extremely useful in increasing spatial resolution. This effect is analogous to magnetic resonance imaging (MRI) whereby magnetic field gradients are used to provide spatial images. As a result of this effect, the spatial resolution in FMRFM is determined by FMR linewidth and field gradient, and *not* the tip radius. This is an important consequence since the physical size of the probe does not determine the spatial resolution limit of the technique. Thus, magnetic structure within an individual nanostructure can in principle be resolved.

While not yet applied to ferromagnetic systems, magnetic resonance imaging (MRFM) was used to perform three-dimensional imaging of the nuclear spins with nanometre resolution [253]. Such resolution will not be achieved in ferromagnetic systems since the resonance linewidth is broader; however, this demonstrates the potential for a scanning probe approach.

Finally, it is worth mentioning a new alternative scanning probe technique that makes use of a conductive coaxial tip instead of a magnetic tip [254, 255]. Here, microwaves are applied to the tip from a VNA which induce a near-field excitation of the sample. The reflection parameter S_{11} or transmission parameter S_{21} (the sample is on a waveguide connected to another VNA port) is then measured by the VNA similar to the VNA-FMR technique. However, since this is a near-field measurement, the excited and measured regions of the sample can potentially be of nanoscopic dimensions. By scanning the probe across the sample, images of the magnetic sub-structure and mode profiles are possible. One advantage to this technique is that the non-magnetic tip does not magnetically disturb the sample.

4.7. X-ray techniques

The use of photons in the extreme-ultraviolet (EUV) and soft x-ray part of the electromagnetic spectrum allows direct access to probe electron transitions in many materials. More specifically, in 3d transition elements such as Fe, Co and Ni, both the M-edge (3p–3d) and L-edge (2p–3d) transitions can be studied as discussed in XMCD and PEEM below. Since these transition energies vary from element to element and the spin-dependent density of states in the 3d electrons is responsible for ferromagnetism in these materials, the element-specific magnetization can be studied. This is a powerful technique since in addition to the static properties, the dynamic properties of the various layers can be independently studied in multilayer systems and/or the magnetic behaviour of different elements can be separately studied in an alloy or compound.

At present, very little x-ray work has been reported on magnetic nanostructures at 100 nm or smaller. However, this topic is of great importance and we include it in this review since sub-100 nm resolution is within reach. A significant advantage in using higher energy photons lies in the fact that these techniques do not have the diffraction-limited barriers in resolution at the length scales of interest relative to optical techniques. (The wavelengths of EUV photons are only a few nanometres and those of x-rays are less than a nanometre.)

Three common approaches are used to generate soft x-ray beams ideal for probing the M- and L-edges of 3d transition metals: (1) synchrotron, (2) free electron lasers (FELs) and (3) high-harmonic generation (HHG) lasers. Each has its advantages and disadvantages.

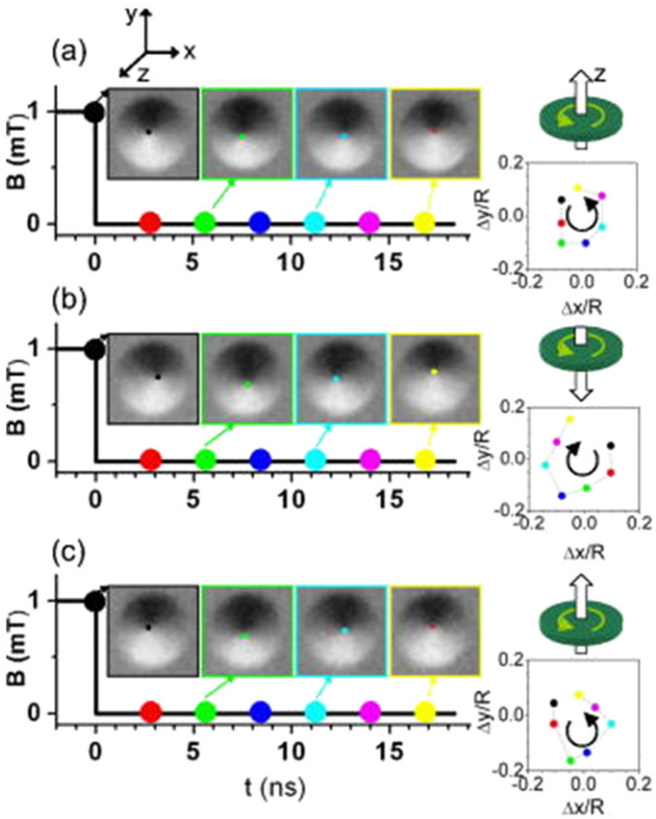

Figure 27. Experimental results of magnetic vortex core polarity reversal. The initial core polarity was up, determined from the sense of the vortex gyration revealed by the TR-PEEM images taken with 1 mT field pulses (*a*). The core polarity was reversed to down polarization after pulsing at 5 mT for 2 s for the second time (*b*). The core polarity was switched back to up polarization after the fourth pulse train (*c*). (Reprinted by permission from [256], copyright 2009 by the American Institute of Physics.)

4.7.1. Synchrotrons. Synchrotrons generate x-rays by accelerating and storing packets of electrons in a large ring at relativistic velocities. X-rays are generated by passing the electron bunches through a bending magnet or undulator which produces bremsstrahlung radiation. The electron bunches typically complete a full revolution in the ring at hundred megahertz frequencies or repetition rates. Repetition rates can be increased by having multiple electron bunches in the ring simultaneously. More importantly, since the electrons traverse in packets, the x-rays generated are not continuous, but are pulses that occur at the repetition rate. Thus, XMCD, x-ray magnetic linear dichroism and PEEM measurements can be performed in the time domain in much the same way that pulsed lasers enable TR-MOKE measurements. The sub-nanometre wavelength of x-rays, however, also allows for spatial resolution of the magnetization as it evolves in time. Figure 27 shows a series of XMCD images of a vortex core as it precesses in time.

To date, most synchrotron based dynamic studies have focused on magnetic reversal [257], domain wall dynamics [258–260] and vortex core dynamics [256], which all occur at frequencies of a few gigahertz or lower. This largely originates from the time resolution of synchrotrons, which is typically limited to >70 ps. Such time resolution excludes measurement of materials with larger anisotropy where the mode frequencies are significantly higher. In order to overcome the time resolution of synchrotrons, the very recent use of femtosecond slicing has been shown to produce a time resolution of $\approx$100 fs, but at a significant cost in the intensity of the x-ray beam [261–263]. To date, the use of femtosecond slicing on nanostructures has not been reported, but it is only a matter of time before it is applied to study the dynamics of nanostructures.

4.7.2. Free electron lasers. The use of FELs is an alternative means to generate femtosecond pulses of x-rays, with several orders of magnitude higher beam intensity relative to femtosecond slicing methods [264]. With FELs, relativistic electrons are sent through an undulator in much the same way x-rays are generated in synchrotrons, but in this case the phase of the electron motion through the undulator matches the wavelength of the emitted x-ray radiation. This phase matching results in self-amplification of the emitted radiation, producing a bright coherent source with tens of femtosecond pulse widths. More importantly, the increased intensity of FELs opens the possibility for ultra-fast imaging of the magnetization with holographic and lensless imaging techniques [265].

4.7.3. High-harmonic generation lasers. While very successful, the use of synchrotrons and FELs require expensive, large facilities with limited access. With the very recent development of HHG laser technology, highly coherent and intense light sources have become available for use in the laboratory [266]. Such HHG sources have already demonstrated a time resolution of 0.1 fs and photon energies as high as 2 keV. Of importance is the fact that easily achievable photon energies of 40–80 eV overlap the M-edge of Fe, Ni and Co (53 eV, 66 eV and 59 eV, respectively). Thus, element-specific femtosecond magnetic process can be studied in the laboratory for such 3d transition metals. While HHG sources have yet to be applied to magnetic nanostructures, these sources are in their infancy, with the first reported work on M-edge detection of magnetic behaviour in 2009 [267]. The high coherence and intensity of HHG sources also open the possibility for ultra-fast imaging of magnetization dynamics via holography and lens-less imaging techniques [268, 269].

To serve as an example, the bottom part of figure 28 shows the energy spectrum of a HHG source that spans the 40 to 75 eV photon energy range. Since the photon energies are spread over a broad range of energies, they must be separated in energy in order to achieve elemental contrast (i.e. to resolve the different M-edges). One approach is to pattern a diffraction grating in the sample such that the scattered photons will diffract at different angles depending on their energy. The change in absorption, and hence magnetic contrast, is a result of the transverse-MOKE (T-MOKE) effect. When two spectra are taken at opposite polarity of the applied magnetic field and subtracted from each other, the asymmetry from the difference in T-MOKE absorption becomes apparent. The upper part of figure 28 shows an example of the asymmetry taken from a $Ni_{80}Fe_{20}$ diffraction grating. The M-edges of

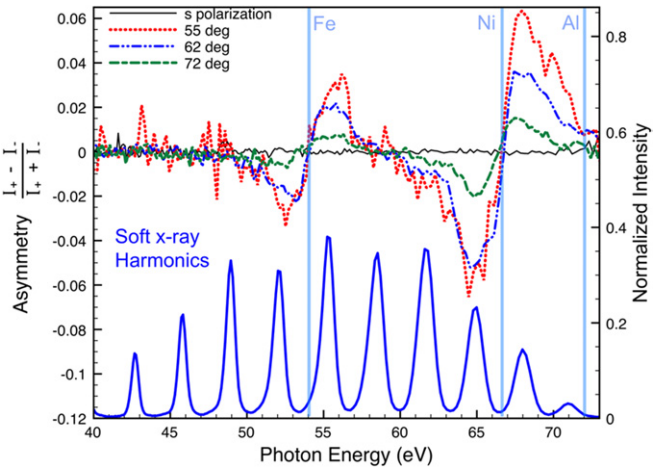

Figure 28. Experimental data showing a HHG spectrum (bottom, right axis) and measured magnetic asymmetry (top, left axis) for different incident angles. The vertical lines denote Fe, Ni and Al absorption edges [267].

both Fe and Ni are well defined and separated. Using a pump–probe scheme, ultra-fast time-resolved element-specific measurements have been demonstrated with ≈55 fs resolution. As with synchrotrons and FELs, HHG sources have yet to measure sub-100 nm nanostructures, but this will soon become an important method for the study of nanostructures.

5. Magnetization reversal

The mechanism for magnetization reversal for magnetic nanostructures depends largely on their sizes and effective anisotropies. We can separate the reversal process into three modes: coherent rotation, curling, and nucleation and domain wall propagation. Below the exchange length L_{ex}, reversal is well described by the SW model of coherent rotation. At dimensions well above the L_{ex}, reversal is accomplished by domain wall nucleation and propagation. Reversal of nanostructures with lateral dimensions in the vicinity of L_{ex} is more complex. We exclude reversal in nanowires from this discussion because the reversal mechanism is not sufficiently different from those found in micrometre-sized structures.

5.1. The macrospin model and SW switching

The exchange length, given by $L_{ex} = \sqrt{2A/(\mu_0 M_s^2)}$ (A is the exchange stiffness constant), is a useful material parameter that describes the spatial extent to which we can treat a ferromagnet as a single exchange-coupled system with a uniform magnetization, or a macrospin. Consider an ellipsoidal magnetic particle with a uniaxial anisotropy and long axis directed along the x-axis as shown in the left-hand side of figure 29. Due to the magnetocrystalline and shape anisotropies, the particle will be uniformly magnetized along the x-axis in the absence of an external field. The energy of the system will be the same whether it is magnetized in the positive or negative x-direction. In fact, since the x-axis is the easy axis of the system, both of these magnetic states will be,

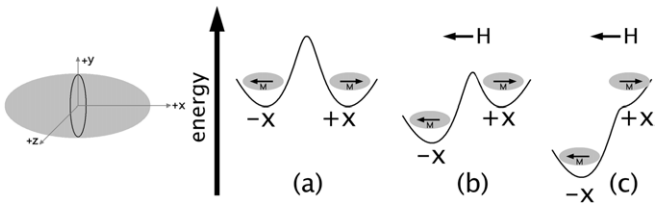

Figure 29. SW switching of a single-domain ellipsoidal particle. (*a*) Two degenerate minimum energy states along the long axis (+ and $-x$ directions). (*b*) External field H lowers the energy barrier and the energy potential for the minimum at $-x$, making it a global minimum. (*c*) Switching occurs when the energy barrier vanishes.

by definition, energy minima (see figure 29(*a*)). However, the system cannot move between these energy minima (i.e. switch) without overcoming an energy barrier. In such an ellipsoid, the energy barrier, E_b, is equal to $K_{eff}V$, where K_{eff} is the effective anisotropy energy density and V is the volume of the ellipsoid. K_{eff} includes the magnetocrystalline anisotropy as well as the shape anisotropy terms.

Consider that this ellipsoid is initially magnetized along the positive x-direction. If an external field H is applied along the negative x-direction, two things happen: (1) the energy barrier will be reduced according to

$$E_b = \frac{K_{eff}V}{k_B T}\left(1 - \frac{\mu_0 H M_s}{2K_{eff}}\right)^m \tag{14}$$

where m is usually taken as 2 [57, 270]; and (2) the Zeeman energy will lower the energy well for the magnetic state in the negative x-direction relative to the positive x-direction (i.e. the degeneracy is lifted and a magnetization along the negative x-direction becomes the global energy minimum as in figure 29(*b*)). As the field is increased, the barrier will continue to decrease until it vanishes when $H = 2K_{eff}/\mu_0 M_s$, at which point the particle's magnetization will reverse or switch (figure 29(*c*)). Thus, this field is the coercive field of the particle. Such a reversal process is referred to as the SW reversal mode or alternatively, coherent rotation.

This description of the reversal process indicates that the coercivity of a particle is equal to $H_c = 2K_{eff}/(\mu_0 M_s)$). In reality, the coercivity changes as a function of temperature and the time for which the external field is applied. This can be understood by consideration of thermal fluctuations in the kinetics of the reversal process. By applying the SW energy barrier to the Arrhenius–Néel equation for relaxation rates [58],

$$f = f_0 e^{-E_b(H, K_{eff}, M_s, V)/k_B T} \tag{15}$$

one can arrive at the well-known Sharrock equation for the coercivity:

$$H_c(T, t) = H_{c0}(1 - [k_B T/(K_{eff}V)\ln(f_0 t)]^n) \tag{16}$$

where H_{c0} is the anisotropy field, which is equal to H_c at $T = 0$, K_{eff} is the effective anisotropy, V is the volume of the nanostructure, f_0 is the thermal attempt frequency, generally taken to be 10^9 s^{-1}, and $n \equiv 1/m$ is equal to 1/2 in the ellipsoid example [57, 270], but was experimentally found to be closer to

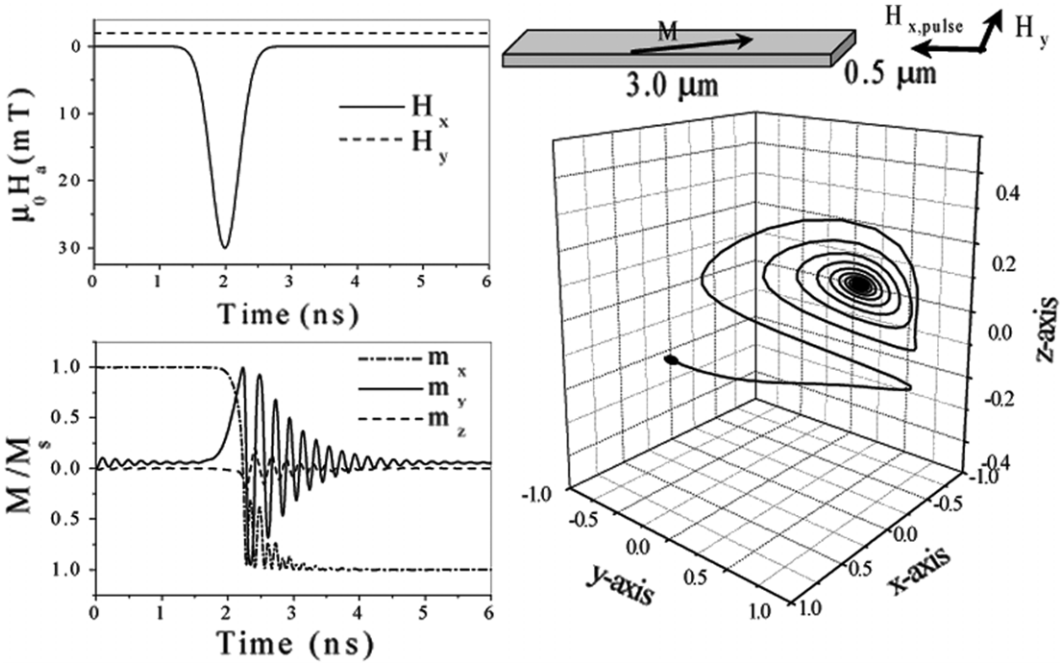

Figure 30. Single-domain simulation of a spinvalve subject to a 30 mT, 200 ps longitudinal field pulse (x-direction) with a static transverse (y-direction) applied field of 2.5 mT. The device switches by precessing around a combination of demagnetizing and applied fields. The trajectory of the magnetization as it switches is plotted on the right [276].

2/3 in granular recording media where some coupling between 'particles' exists [271]. This equation shows that the reversal gains a 'thermal assist' at finite temperatures, reducing the coercivity.

The Sharrock equation describes the thermal model for a single-domain particle, and has been a proven tool in describing the time and temperature dependence of reversal processes in these particles. However, this thermal model ceases to work at fast switching times in the vicinity of a nanosecond. This breakdown was more recently observed in STT-RAM devices [272, 273]. Here, we have entered what is commonly referred to as the precessional switching regime [274–277]. This is a particularly important time regime since most data storage technologies will need to write data at such rates with nanosecond field pulses. In a simplistic description, the thermal model breaks down as the applied field time is no longer $\gg 1/f_0$, and thus, there are very few thermally assisted 'attempts' to overcome the energy barrier. From another point of view, the thermal model describes a quasi-static switching mechanism where the nanostructure simply follows the energy minima of the system with thermal fluctuations providing the means to hop the energy barrier between the energy minima.

In the precessional switching regime, non-equilibrium magnetization dynamics (or precession of the magnetization) dominate the process, which is better described by equation (3). Figure 30 shows a macrospin simulation of precessional switching in a structured spin-valve. The element is initially magnetized in the positive x-direction and a 200 ps field pulse is applied in the negative x-direction. The device switches in less then a nanosecond and the magnetization precesses until the energy is dissipated through the damping.

5.2. Non-uniform magnetization reversal

The SW and macrospin models are very useful for describing the reversal process in nanostructures in the vicinity of, or smaller than, the exchange length. In larger structures, the magnetization throughout the nanostructure may not be uniform during the reversal process. In fact, the remanent magnetic configuration may not necessarily be uniform to begin with, as in for example, a vortex state or onion state ([278] has a collection of calculated images of various domain states along with their common names). In this case, a micromagnetic description is needed to fully understand the reversal process.

Consider a single ferromagnetic atom. It has a time averaged dipole moment in units of μ_B. However, when such an atom is confined to a lattice with other atoms, electron orbitals overlap which generates a variety of macroscopic phenomenon. Micromagnetics is a phenomenological evaluation of the total magnetic energy of a ferromagnetic body based on known material, geometry and initial magnetization configuration [279]. Typically, the total energy in a magnetic body is given by the summation of several types of interactions: exchange, magnetocrystalline anisotropy, magnetostatic energy, Zeeman energy and magnetostriction. The micromagnetic model solves the LLG equation (3) iteratively. The different interaction terms (exchange, anisotropy due to magnetocrystalline and surface contributions, etc) are all included in the effective field term, H_{eff} in equation (3). In this model, any structure larger than L_{ex} may have locally varying magnetization in order to minimize the energy.

We will review three common non-uniform reversal processes: (1) curling, (2) vortex switching and (3) nucleation

and rapid domain wall propagation. In this section we restrict our discussion to nanostructures that have nanoscopic sizes in all three dimensions (i.e. nanodots, nanodiscs, nanopillars, etc). Reversal processes in elongated structures such as nanowires are not as important to the technologies covered in this paper and therefore will not be discussed.

In nanostructures with large aspect ratios, i.e. softer magnetic materials that have large shape anisotropy, curling often occurs during reversal [280]. Curling can be viewed as an extension of the SW switching. Here, magnetization reversal also occurs by rotation, but the direction of magnetization 'curls', particularly at the ends of an elongated nanostructure. As a result, parts of the nanostructure will respond differently to the applied field. This effect is largely a result of minimizing the magnetostatic energy throughout the reversal process, which would be rather large for a coherent rotation process in high aspect ratio structures. Also, if the size of the structure is significantly larger than L_{ex}, the cost in exchange energy may be partially offset by the reduction in magnetostatic energy by having a non-uniform magnetization configuration.

The vortex deserves some mention because it is one of a few types of remanent domain structures that can occur in sub-100 nm structures. In a vortex state, the magnetization follows a clockwise or counterclockwise path. The vortex core itself can be magnetized into or out of the film plane. The idealized vortex is therefore energetically four-fold degenerate. These uniquely stable configurations are of tangential interest for some MRAM applications [281, 282]. Switching from one of these energy minima to another is much more difficult to predictably control and model relative to a bi-stable ellipsoid example. Configurations with different core chirality and polarity, which have very different symmetries, may be independently accessed. Indeed many groups have developed recipes to control the chirality [283–285] or the polarity [286–288] of the vortex.

One common reversal mechanism in nanostructures is that of nucleation and domain wall motion followed by domain wall annihilation. This occurs in structures even if a domain wall is not a stable ground state of the system, and occurs for both in-plane [289] and out-of-plane [68] magnetized nanostructures. A nucleation event typically occurs at a defect site or an edge or surface region. On edges and surfaces, the surface charges lower the demagnetization energy enough to partially offset the increase in energy incurred by nucleation. From a precessional switching perspective, this latter nucleation event can alternatively be described as nucleation from certain normal modes of the structure, which, for example, have their amplitude of precession concentrated at the edges of the structure.

Once the nucleation event occurs, the created domain wall quickly propagates in a nanostructure, since this is a high energy state of the system. However, known pinning sites such as voids and magnetic or non-magnetic inclusions [290], grain boundaries [291, 292] and edges [293] can inhibit further expansion of the reversed domain. In general, the choice of nucleating a new domain or dislodging an existing domain wall from a pinning site comes down to overcoming the lowest of the energy barriers present. However, since domain wall widths are typically 20–50 nm, the domain wall energy is a large fraction of the overall energy and the pinning energy must be significantly large to maintain the presence of the domain wall. The exception to this, of course, is the vortex state. Figure 31 shows an example of micromagnetic simulations of switching of an in-plane elliptical spin-torque device [289]. The reversal is nucleated at the edges of the ellipse before the entire nanostructure reverses several nanoseconds later.

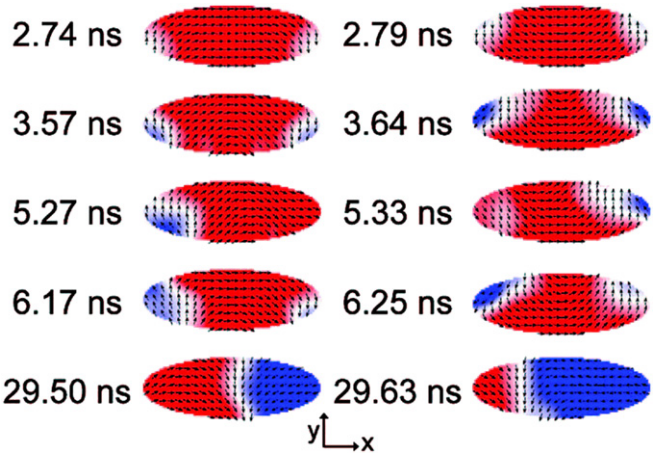

Figure 31. Micromagnetic simulation time sequence of the magnetization distribution for a 170 nm × 60 nm spin-torque device. The colour represents the component of the magnetization along the x-axis (red positive, blue negative). (Reprinted with permission from [289], copyright 2008 by the American Institute of Physics.)

A common means to determine the reversal mechanism is to measure the angular dependence of the reversal field. For the SW coherent rotation reversal mode, the angular dependence will be approximately symmetric with a minimum at 45° between the easy and hard axes with a uniaxial anisotropy [294, 295]. In addition, as we saw earlier, the time and temperature dependence of the reversal field should also obey the Sharrock formalism in the quasi-static regime if the system undergoes a SW reversal mode in the quasi-static regime [57, 296]. Interestingly, such angular and temperature dependence of the reversal field has also been observed in perpendicular nanostructures that are known to reverse by a nucleation and rapid domain wall motion [52, 68]. This discrepancy can be explained since it was discovered that a nucleation volume on the size scale of the exchange length undergoes a quasi-SW reversal process. Thus, the rate-limiting step is the nucleation of the quasi-SW volume, not the subsequent propagation of the domain wall. The strict SW-like behaviour of the nucleation volume is not necessarily universal. In Co/Pd nanostructures that have a modified anisotropy at the edge region (due to fabrication damage, for example), the temperature and angular dependence of the reversal field deviate from the SW mode [68].

6. Current challenges

6.1. Superparamagnetic limit

The 'superparamagnetic limit' has been, and continues to be, a road block for improving areal density in HDD. Over the

years, the HDD industry has managed to postpone this limit with innovations such as perpendicular magnetic recording. The term superparamagnetic limit therefore is a subject of some debate and many believe it is more correct to call it the 'superparamagnetic effect' instead. Regardless, a hard fundamental limit exists. In current HDD technology, the bits are approximately 20 nm in size; however, in the future, information may be written to only a handful of atoms.

A paramagnet (Pt or Pd, for example) exhibits a magnetic moment only in the presence of an external magnetic field, and the magnetization direction is strictly that of the applied magnetic field direction. If a magnetic particle is small enough at a given temperature, the direction of its magnetization will also freely follow the external field, not unlike a paramagnet. Of course, ferromagnets have various interactions and anisotropies that can resist the external field and provide a net magnetic moment in remanence. If the supplied thermal energy exceeds the effective anisotropy, the magnetic ordering vanishes and the object becomes superparamagnetic [297].

One way to appreciate the superparamagnetic effect is to recast equation (15) to give switching probability, $P = f/f_0$. Assuming a single crystal Ni sample shaped into a sphere, 2.4 nm in diameter, with cubic anisotropy, $K_u = 5.7 \times 10^3$ J m^{-3} [298] at 300 K, it is nearly certain that thermal energy alone can switch the magnetization on the timescale of $1/f_0$. Another way to look at the superparamagnetic effect is to invert equation (15) to give $\tau = 1/f$, the average waiting time before a switch occurs. If we want to improve the magnetic stability such that the same sort of Ni specimen can withstand thermal fluctuations at 300 K for 10 years, for example, we would need to increase the Ni sphere diameter to 39 nm. This type of analysis is what people in the HDD industry do to evaluate data retention timescales in magnetic media. While increasing K_{eff} and V improves thermal stability and SNR, in order to keep pace with the HDD road map (double the areal density every 3 years), increases in V are generally not an acceptable option. As a result, thermal stability must come from improving K_{eff} through high-anisotropy materials or shape engineering.

The tyranny of improving anisotropy for thermal stability is that it simultaneously makes magnetization reversal (data recording) more difficult. This is the case for both granular recording media and the BPM. As a result, various strategies are being investigated to mitigate this problem. One is exchange-coupled composite (ECC) media, where the recording will be performed on a magnetically soft layer exchange coupled to a magnetically hard layer, which will store the data. Proposed variations includes bi-layer media or 'exchange springs' with high and low uniaxial anisotropy (K_u) regions [299–301], and K_u that is continuously graded [302]. Another strategy is to use 'energy-assisted recording', where an externally supplied short burst of energy temporarily lowers the energy barrier to switch. In heat-assisted recording [303], the media is heated to near T_c with a laser with a small (<20 nm) spot size so that the irradiated region may be switched at a lower field. In microwave assisted switching [14], the recording head consists of an STO which when brought into the proximity of the media, causes spin precession in the media, thus lowering the energy threshold for switching.

6.2. *Anisotropy distributions*

Another critical challenge in implementing magnetic nanostructures into technologies such as BPM and spintronics is controlling the variation of magnetic properties from nanostructure to nanostructure. In BPM, for example, the write head is optimized to switch the media within a certain narrow range of magnetic field. If a nanostructure has a significantly higher switching field relative to the rest of the media, the write head may be unable to switch it in a predictable manner, resulting in write errors. Likewise, if a nanostructure has a significantly lower value of switching field relative to the rest of the media, it may undergo reversal when an adjacent bit is written, which also results in write errors. As another example, anisotropy variations in spin-torque devices manifest themselves in distributions of the critical current or a device-to-device variation in output frequency of STOs.

The variation in magnetic properties is usually expressed as an anisotropy distribution or SFD, although variation in other properties such as the saturation magnetization can also occur. Such distributions decrease the predictability and reliability of devices. Typically, anisotropy distributions and SFDs are approximated by a Gaussian distribution and are expressed in terms of the standard deviation (σ) or normalized standard deviation. We use the term 'anisotropy distribution' as a general term for the physical intrinsic anisotropy energy variation within the material. SFDs are measured through (and normalized to) the switching or reversal field H_{sf} and are commonly used as a metric to describe the variation since SFDs can be directly measured. Strict control of the SFDs in BPM is essential in making it a viable technology. It is predicted that the SFD (σ/H_{sf}) must be below 7% for BPM to be practical [304]. This value is lower than values reported for practical materials patterned into sub-50 nm features.

The next question is, what causes SFDs and variation in magnetic properties among nanostructures? To answer this question we need to understand what factors influence the magnetic properties in a nanostructure and how such factors vary in realistic systems. The answer is not trivial and can be different depending on the material system. A large distinction between systems of nanostructures is whether they are magnetized in-plane or out-of-plane. The factors that affect anisotropy distributions can be quite different for these two cases.

6.2.1. In-plane magnetized structures. Nanostructures that are magnetized in-plane tend to have a small to moderate magnetocrystalline anisotropy unless they are epitaxially grown or exchange biased. However, due to the demagnetizing fields, in-plane structures can have relatively large contribution from shape anisotropy. As a result, the magnetic properties of in-plane structures are very sensitive to variations in the size and shape of the nanostructure. Figure 8 shows MOKE magnetometry curves on 65 nm diameter $Ni_{80}Fe_{20}$ nanostructures that are circular in shape. The magnetization curves show only a small amount of coercivity with no preferred anisotropy axis. However, when a small amount of ellipticity is introduced, the coercivity and anisotropy increase

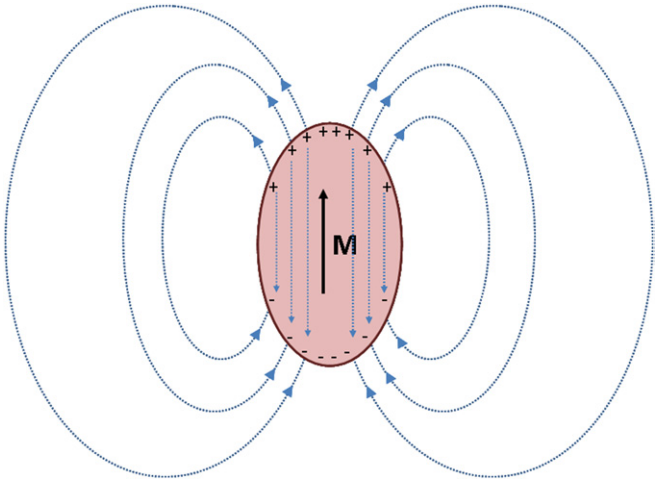

Figure 32. Schematic diagram showing the H-field generated from the edge charges of a uniformly magnetized ellipse.

substantially. These data show how the shape of such structures can dominate the anisotropy.

In section 4, we presented several examples of how small variations in the structure definition can have significant effects on the magnetic properties. Recall that both size and shape fluctuations significantly broadened collective linewidths in arrays of nanostructures. The roughness of the edges and sidewall tapering also influenced the linewidth and reversal fields in stripes. All of these examples come together to show how small changes in the shape, and thus the demagnetization fields, strongly influence the magnetic properties for in-plane magnetized nanostructures.

A useful tool to visualize demagnetization effects is that of magnetic surface charges (figure 32). Magnetic charges are a purely mathematical construct (magnetic monopoles have not been found to exist), but help in the analysis of confined structures. The magnetic surface charge is defined as $\sigma_m = \boldsymbol{m} \cdot \hat{n}$, where $\boldsymbol{m}$ is the local magnetization vector at the surface and $\hat{n}$ is the unit vector normal to the surface. Thus, where the magnetization has a component perpendicular to the edge of a structure, magnetic surface charges will form, resulting in a demagnetization field that opposes the magnetization. Because this is a dot product of the magnetization with the local surface (or edge) normal, it is easy to see why variations in the edge curvature, side wall tapering, edge roughness, surface roughness and shape will change the magnetic charge configuration and distribution. This is also an alternative description of shape anisotropy, since the magnetic charges will vary as $\boldsymbol{m}$ is rotated. The direction that minimizes the magnetic surface charges will become the easy axis.

We have seen that in the absence of a strong in-plane anisotropy, extrinsic factors tend to dominate the anisotropy and reversal properties. In fact, artificial variation of the material properties can be used to intentionally tailor the anisotropy of the material [305]. Therefore, optimizing the lithography and fabrication processes to achieve uniform feature size and shape will be critical to achieving narrow anisotropy distributions.

Other factors in addition to shape can also change the anisotropy in nanostructures. For example, consideration of thin oxide layers at the surface or edges of the nanostructure may also need to be taken into account. In spin-torque devices, sidewall oxidation was shown to form an antiferromagnetic layer that altered the device properties [306]. Also, in GMR and TMR devices, roughness can cause coupling of the two magnetic layers through the non-magnetic layer, in so-called orange-peel coupling [195, 307]. However, as the GMR or TMR devices are reduced in size, the direct dipole coupling between the magnetic layers may overshadow the orange-peel coupling effects. Finally, uniformity of the material and the microstructure can have a large impact on the damping and linewidth, which is of great importance for switching in the fast (nanosecond) regime. In the presence of strong in-plane intrinsic anisotropy (such as antiferromagnetically coupled pinning layers), many of the factors for perpendicular materials may also be applicable and should be considered.

6.2.2. Perpendicular materials. Out-of-plane magnetized nanostructures tend to exhibit much more complicated behaviour. This is largely a result of the fact that the magnetocrystalline anisotropy of the material is relatively large and highly dependent on the crystalline phase and microstructure. Since the reversal process in many perpendicular nanostructures is often controlled by a nucleation event at a defect (localized region of reduced or modified anisotropy), much work recently has been directed at understanding the physical origin of defects and minimizing them. We define a 'defect' as a region with a lower than average energy barrier for reversal. Defects are typically classified into two categories: intrinsic and extrinsic defects.

As a result of the exchange interaction these two categories of defects and inhomogeneity within the material become difficult to separate and study directly. As we will see, quantitative analysis of defect properties are studied indirectly by statistical methods such as size-dependent properties in arrays of nanostructures or FMR.

Intrinsic defects. Intrinsic defects refer to variations of the magnetic properties within the material itself; those that occur during growth or deposition. Such variations can manifest themselves as a distribution of nucleation fields and energy barriers within the material. When such a material is nanopatterned, these distributions affect both the average switching field and the SFDs. To understand why that is the case, we have to understand the reversal mechanism that occurs in perpendicularly magnetized nanostructures. In materials such as Co/Pd multilayers, the reversal mechanism is that of nucleation and rapid domain wall motion [52, 68, 308].

The effect of anisotropy distributions applied to the nucleation and rapid domain wall movement reversal mechanism results in an overall reduction in the average switching field in an array of nanostructures as well as a size dependence of the reversal field as shown in figure 33(*a*). Shape effects are not sufficient to explain such a strong size dependence of the average reversal field in these data. This size dependence occurs as a result of a statistical effect: the larger the structure, the larger the statistical sampling of nucleation fields that are available in each structure (figure 5). Thus,

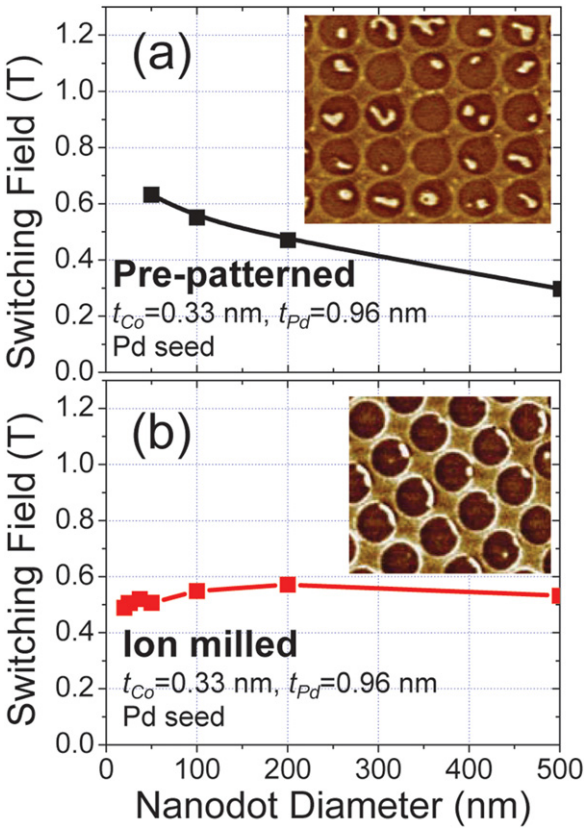

Figure 33. The diameter dependence of H_{sf} for (*a*) pre-patterned and (*b*) ion-milled samples. The insets in (*a*) and (*b*) show the corresponding MFM images of the nucleation sites in $d = 1\mu$m dots induced with an in-plane field [68].

larger structures have a high probability of containing a region with a low nucleation field (e.g. figure 5(*a*)), whereas smaller structures have a low probability of containing such a region (figure 5(*c*)). Since the reversal process in a structure is largely controlled by the region within the structure that has the smallest nucleation field, smaller structures will on average have larger switching fields. In addition to the change in average switching field in nanostructures, an increase in the anisotropy distributions also introduces an increase in SFD. Thomson *et al* showed how the size dependence of H_{sf} and SFD can be fitted to a model in order to obtain quantitative information about the variation in the intrinsic anisotropy and the length scale of the nucleated volume [52].

This model assumes a distribution of nucleation fields and energy barriers from the intrinsic distribution of defects. We recently showed that such intrinsic defects possess more complicated behaviour. The angular dependence of the nucleation fields in Co/Pd indicates that the intrinsic defects consist of a canted anisotropy axis instead of, or in addition to, a reduction in the magnitude of the anisotropy [56]. A consequence of this property is that the intrinsic defect responsible for reversal becomes dependent on the applied field orientation.

While the presence of intrinsic defects is established, the fundamental origin of such defects and how to control them are still areas of intense study. Since there is much evidence that an intrinsic defect is a local variation of the anisotropy, the factors that affect the anisotropy at a fundamental level need to be examined. The anisotropy in perpendicular systems can originate from several sources, including interface effects, magnetocrystalline and magnetoelastic terms. Multilayer materials such as Co/Pd and Co/Pt have large contributions to the anisotropy from the interface [309]. As a result, these materials are intentionally engineered to have a large number of interfaces with very thin layers (typically 0.2–2 nm). The anisotropy in Co/Pd and Co/Ni multilayers also has a significant dependence on the crystalline orientation [310, 311]. In both of these cases, the ⟨1 1 1⟩ directions have the highest anisotropy. The anisotropy in materials such as FePt and FePd is highly dependent on the crystalline phase as well as the orientation. In $L1_0$ materials (such as FePt, FePd and CoPt) for example, the $L1_0$ crystalline phase is responsible for the very large values of anisotropy found in this material. Thus, if some grains are not highly $L1_0$ ordered, there will be a significant reduction of anisotropy within that grain.

From this discussion, it is reasonable to assume that a variation in the structure and microstructure of the material can manifest itself as a variation in anisotropy across the material. In fcc Co/Pd, the SFDs are highly dependent on the quality of the ⟨1 1 1⟩ texture [53, 309, 312]. This indicates that the grain orientation and uniformity of the grain orientation play critical roles in controlling SFDs. TEM analysis of arrays of Co/Pd nanostructures also supports this idea since those nanostructures that had the lowest reversal field had a high probability of containing a grain that was misaligned (i.e. significantly deviated from a ⟨1 1 1⟩ orientation) [54].

There may be other sources of anisotropy distributions in addition to the microstructure. Stacking faults in close-packed structured materials cause a local change between fcc and hcp structures [313–316]. This induces a significant change in the local anisotropy thought to be due to local changes in the spin–orbit interaction.

Roughness is also a significant contributor to SFDs in Co/Ni multilayers, dominating the reversal properties in some cases [317]. As a result, much of the effort needed to reduce intrinsic defects becomes a materials problem. Within a particular materials system, the properties which give rise to fluctuations in the magnetic properties must first be understood. This is not a trivial determination since the magnetic properties of a particular grain, for example, cannot be isolated from the surrounding material due to the exchange interaction or that it is simply too small to measure with current technology. In addition, strict control of the materials properties needed to correlate with the magnetic properties becomes a challenge in itself. For example, in [317], the roughness of a sample was systematically varied to study the effect it had on the inhomogeneity in Co/Ni. However, changing the roughness also changes the grain size and maybe the growth morphology. Thus, while there was a strong correlation of the roughness to the magnetic inhomogeneity, there are still unanswered questions as to the relative contributions of the surface topography, grain size and roughness-induced variation in growth dynamics during deposition. Addressing such questions offers a rich landscape for future work.

Extrinsic defects and other contributions to the SFD. Extrinsic defects refer to defects introduced during the fabrication process. As with in-plane magnetized structures, variations in the nanostructure size and shape can influence the reversal properties. Generally, the shape anisotropy in strongly perpendicular nanostructures is rather small compared with the perpendicular anisotropy unless the nanostructures have large aspect ratios [85, 318, 319]. It is also reasonable to assume that structures with significant sidewall tapering would be more sensitive to shape effects since this geometry will create magnetic charges in the presence of a perpendicular magnetization. A variation in size can affect the switching field as demonstrated in nanopatterned Co/Pd [320, 321]. Recall that there is a size dependence of the average switching field in an array (figure 33). Thus, a size fluctuation in an array can contribute to increased SFDs via this mechanism. However, the size dependence shown in figure 33 is largely a statistical effect on the *average* switching field of an array resulting from the distribution of perpendicular anisotropy, and therefore does not straightforwardly translate into a direct size dependence for an individual nanostructure.

It has yet to be well established how size variations *directly* affect the reversal field in nanostructure. To do so would require an extremely homogeneous material in order to exclude the indirect intrinsic contribution. However, micromagnetic simulations in [68] show negligible size dependence for nanostructures larger than 100 nm. Below 100 nm, the aspect ratio of the 12 nm thick structures becomes large enough such that the shape effects begin to have an influence on the reversal process. This result is consistent with shape anisotropy calculations taken from the demagnetization factors calculated for a prism with similar values for size and thickness [322]. Magnetically softer materials such as Ni have been patterned into elongated nanopillars [319]. In this case, the perpendicular anisotropy is almost entirely due to shape. In these systems, the direct effect of size variations may be more direct.

Extrinsic defects at the edges can significantly alter the reversal process in perpendicularly magnetized nanostructures [68]. Ion induced damage at the edge region from the etching process in Co/Pd alters the anisotropy of the edge material. As a result of the edge properties, reversal of the nanostructure can be nucleated at the edge. Similar behaviour can result from sidewall tapering at the edges [323]. Figure 33(*b*) shows the size dependence of the switching field for an ion-milled sample. In contrast to the nanostructures whose reversal is dominated by intrinsic defects, the size-dependent switching properties show a maximum in the reversal field before beginning to decrease as the size is further reduced. Consider the ratio of edge material to the total volume of a nanostructure; as a structure becomes smaller, this ratio increases, which results in the edge material becoming more influential on the magnetic properties of the entire structure.

Finally, while not a defect, dipolar interactions can cause increased SFDs in dense arrays of nanostructures [324]. Consider two closely spaced perpendicularly magnetized nanostructures. If their magnetic moments are parallel, then the dipole field that one exerts on the other is in the opposite direction, effectively lowering the external field needed to reverse one of the nanostructures. If the neighbouring nanostructure's moment is antiparallel the opposite occurs and the external field required for reversal is increased. Thus, the reversal field of a nanostructure is dependent on the magnetic state of its neighbours. The magnitude of this effect is clearly dependent on the magnetic moment of the structures and the distance between them. As a result, this problem is much more of concern for technologies such as BPM and not device technologies such as MRAM where the device to device distance is much larger.

6.2.3. Approaches to circumvent anisotropy distribution. Various approaches can reduce the magnitude of anisotropy distributions. Reducing the intrinsic distribution will require significant materials science to obtain a homogeneous material. Optimizing the lithography and etch processes can minimize many extrinsic contributions. However, completely eliminating anisotropy distributions would be virtually impossible.

Recent modelling work indicates that SFDs can be lowered by applying the external field at a 45° angle versus a strictly perpendicular field [325]. This suggests that careful consideration of applied field direction can help reduce the effect of anisotropy distributions. Another approach involves using the above mentioned exchange spring concept. Here, a magnetically hard material such as Co/Pd is exchange coupled to another material with a lower anisotropy such as Co/Ni [75]. In addition to the benefit of lowering the overall switching field of the nanostructure while maintaining thermal stability, if the source of anisotropy distributions in the two layers are decoupled, then a narrower overall anisotropy distribution results [326].

Currently there is no clear solution to the anisotropy distribution problem. In order to make technologies such as BPM viable, more work will be needed to bring anisotropy distribution under control. New and creative approaches will likely be needed and this offers many opportunities for future research.

6.3. STT considerations

STT effects can be beneficial or detrimental depending on the application. STT-RAM's function depends on maximizing the efficiency in the transfer of electron spin angular momentum. In read heads, and particularly CPP-GMR read heads, however, STT must be suppressed.

6.3.1. STT-RAM. For STT-RAM to be a viable alternative to DRAM, it must have low switching current density ($\leqslant 10^6\,\mathrm{A\,cm^{-2}}$), sufficient thermal stability ($E_b/kT > 60$) and reasonable TMR (>150%). These requirements are challenging to meet simultaneously. Two geometries: ferromagnetic electrodes magnetized either parallel, or perpendicular, to the tunnel barrier plane have been variously considered. The critical current, I_c, required for switching the free layer from a parallel to an antiparallel state for the in-plane

and perpendicular geometries are given respectively by (17*a*) and (17*b*) [327].

$$I_{c_\parallel} = \frac{2e}{\hbar}\frac{\alpha\mu_0 M_s V}{g(P,\theta=0)}\left\{H - H_{dip} + H_{k\parallel} + \frac{M_s}{2}\right\} \quad (17a)$$

$$I_{c_\perp} = \frac{2e}{\hbar}\frac{\alpha\mu_0 M_s V}{g(P,\theta=0)}\left\{H + H_{dip} + H_{k\perp} - M_s\right\}. \quad (17b)$$

Here the term $g(P,\theta)$ is the spin-transfer efficiency function which is a function of the polarization P and the magnetization angle θ between the fixed and pinned layers [9, 328]. The grouped field terms at the end of (17*a*) and (17*b*) are the sum of the magnetic fields acting on the free layer. Here H is the applied field (with the assumption that the field is applied in the direction that favours the parallel alignment of the fixed and pinned layers), H_{dip} is the dipolar interaction field due to the pinned layer, and $H_{k\parallel}$ and $H_{k\perp}$ are the in-plane and perpendicular anisotropy fields, respectively. Finally, M_s appears in the last field term as the demagnetization field, which is different for the in-plane and out-of-plane configurations. The signs in the field terms will make the free layer easier or more difficult to switch by either decreasing or increasing the switching current. For STT switching, it is very important to reduce I_c, not only from an energy consumption point of view, but because large current densities may cause electromigration problems and/or degrade the oxide barrier over time.

From equations (17*a*) and (17*b*), we can see that I_c is different for in-plane and perpendicular MTJs. When considering the thermal stability criterion, however, the energy barrier improves with the anisotropy field H_k only. In the in-plane geometry (equation (17*a*)) , the current required to switch must overcome $H_{k\parallel}$ (which plays into the thermal stability of the bit) and the demagnetization field $M_s/2$ (which does not). Therefore, if all the parameters M_s, V, α, g, H_k, H_{dip} are equal in the two cases, then in theory, the perpendicular MTJ wins the efficiency argument in terms of satisfying the thermal stability criterion without additional increases to I_c. However, these parameters are typically different for the two systems, making an efficiency comparison non-straightforward.

One strategy for improving I_c in spin-valves and MTJ with in-plane magnetized electrodes is by reducing the $M_s/2$ term in equation (17*a*). By placing a perpendicularly magnetized layer next to the in-plane free layer, the out-of-plane demagnetization $M_s/2$ can be diminished or even eliminated, but at a cost of reducing $g(P,\theta)$ through θ. Some optimization is therefore necessary. Improvements in I_c have been demonstrated separately for both the in-plane magnetized spin-valve [329, 330] and MTJ [331, 332].

Improving the spin-transfer efficiency function g will also reduce I_c for both in-plane and perpendicularly magnetized electrodes according to equations (17*a*) and (17*b*). The polarization, P, in $g(P,\theta)$ is a function of the density-of-states mismatch between the majority and minority carriers at the Fermi level. The greater the disparity, the larger the polarization. Using this definition, half-metals have ideal polarization ($P = 1$). For this reason, there is a large body of interest in half-metallic Heusler alloys within the community [333–340]. While P is material specific, θ can be optimized by spin canting. Conceptually similar to in-plane MTJ described previously, it has been demonstrated for the perpendicular MTJ that g improves when a secondary in-plane fixed layer is inserted next to the free perpendicular layer because this tilts the magnetization in the free layer slightly with respect to the pinned polarizer layer [312, 341]. Using the same scheme, improvements were made to I_c for perpendicular spin-valves as well [341]. In another example, a dual MTJ, where a single free layer is sandwiched by two reference layers pinned in opposite directions, was found to have significantly reduced I_c. Here, g was enhanced through reductions in polarization asymmetry θ between the parallel and antiparallel alignments [342].

Another strategy to reduce I_c is to reduce α. This can be done by selecting materials that have low α to begin with, or designing a MTJ stack to reduce the spin-pumping effect [343]. In the previous dual MTJ example, having geometrically symmetric electrodes was thought to reduce the non-equilibrium α inflation due to spin-pumping.

Looking at equations (17*a*) and (17*b*) again, one might be tempted to reduce M_s or V as ways to reduce I_c. However, since the energy barrier E_b that provides thermal stability is also proportional to M_s and V, reducing M_s and V will simultaneously reduce E_b and can therefore compromise thermal stability. However, the ever present demand for shrinking feature sizes means that reduction in V may be inevitable.

6.3.2. CPP-GMR. In CPP-GMR read heads, the magnetic state of the detected bit rotates the free layer in the spin-valve, and that rotation is interpreted by a sense current going through the stack. The sense current must be large enough to obtain a meaningful signal, yet if it is too large, it can influence the magnetization of the free layer, thus increasing noise. In effect, the strategies discussed above for reducing I_c must now be considered in reverse, i.e. make I_c as large as possible and make sure the sense current is below I_c. The other requirements of thermal stability (though much more relaxed) and that of large GMR are still true, as in the case of the STT-RAM.

The same demagnetization field argument that makes the perpendicular MTJ geometry more sensitive to spin torque means that the in-plane geometry can help increase I_c in CPP read heads. The obvious way to reduce spin-torque effects is to use a smaller sense current, necessitating an increase in GMR. One way to improve GMR is by increasing the resistance–area (RA) product of the spin-valve's active region. For example, it was demonstrated that RA can be improved by alloying Al with CoFe [344, 345]. One idea is a current-confined-path (CCP) CPP-GMR head [346–348], borrowing pinholes, as a concept for failure mode in MTJ, and re-deploying it as a resistance-control device in spin-valves. We mentioned previously that pinholes and metal impurities in the oxide tunnel barrier cause short circuits, and thus severely compromise the performance of an MTJ. In CCP-CPP-GMR heads, a thin oxide layer is embedded in the spin-valve spacer layer. Next, metallic nano-contacts, or nano-current channels, are deliberately placed on the oxide layer, thus a large RA range may be accessible in this way. A familiar problem is in the precision control of the sizes, positions and the distribution of the nano-contacts. Another way to boost GMR is through improved P, for example,

with half-metallic Heusler alloys [349]. However, from equations (17*a*) and (17*b*), one can see that large P also reduces I_c, which reduces the threshold for spin-torque induced instabilities. Therefore, this is a route that must be carefully optimized.

Increasing α is one way to mitigate the effects of spin torque due to the sense current. For example, doping [350, 351] or capping [352] with rare-earth metals significantly increases α and can lead to I_c enhancements. Another way to mitigate spin torque effects is through the dual spin-valve geometry [353]. Geometrically similar to the previously mentioned dual MTJ in construction, mentioned earlier in the STT-RAM section, the two reference layers are pinned parallel to each other, and can ideally cancel the resultant spin-torque effects. In a different design, the free layer is replaced by a synthetic ferrimagnet (two ferromagnetic layers of unequal magnetization, separated by a thin Ru layer). There, each of the ferromagnet/Ru interfaces can independently oscillate, producing a co-resonance condition which can improve spin-torque stability and thus increase I_c [354].

6.3.3. Afterthought. To get at the root causes of magnetic properties distribution, the measurements must be targeted at individual nanostructures with reasonable throughput, i.e. a one second measurement on each of 10^9 structures would consume a prohibitive amount of time.

Acknowledgments

The authors thank Michael Donahue, Ranko Heindl, Xiaoyong Liu, Robert McMichael, Benjamin McMorran, Hans Nembach, Matt Pufall, Stephen Russek, Tom Silva and Mark Stiles. They dedicate this paper to our late colleague, William F Egelhoff Jr, in gratitude for all of his advice, not only on this manuscript, but in the grander scheme of things.

References

[1] Thomson W 1856 *Proc. R. Soc. Lond.* **8** 546
[2] McGuire T R and Potter R I 1975 *IEEE Trans. Magn.* **11** 1018
[3] Baibich M N *et al* 1988 *Phys. Rev. Lett.* **61** 2472
[4] Binasch G, Grunberg P, Saurenbach F and Zinn W 1989 *Phys. Rev.* B **39** 4828
[5] Egelhoff W F *et al* 1995 *J. Appl. Phys.* **78** 273
[6] Butler W, Zhang X, Schulthess T and MacLaren J 2001 *Phys. Rev.* B **63** 054416
[7] Jiang L, Naganuma H, Oogane M and Ando Y 2009 *Appl. Phys. Express* **2** 083002
[8] Berger L 1996 *Phys. Rev.* B **54** 9353
[9] Slonczewski J C 1996 *J. Magn. Magn. Mater.* **159** L1
[10] Katine J A, Albert F J, Buhrman R A, Myers E B and Ralph D C 2000 *Phys. Rev. Lett.* **84** 3149
[11] Mellor C 2008 TDK tunnels through hard drive areal density record - Achieves 803 Gb/in^2
[12] Grochowski E 2003 HDD roadmap
[13] Anonymous 2002 *Int. J. Micrograph. Opt. Technol.* **20** 6
[14] Zhu J, Zhu X and Tang Y 2008 *IEEE Trans. Magn.* **44** 125
[15] Nembach H T, Bauer H, Shaw J M, Schneider M L and Silva T J 2009 *Appl. Phys. Lett.* **95** 062506
[16] Wood R, Williams M, Kavcic A and Miles J 2009 *IEEE Trans. Magn.* **45** 917
[17] Parkin S S P, Hayashi M and Thomas L 2008 *Science* **320** 190
[18] 2006 'Magnetic memory' chip unveiled—BBC world news 10 July
[19] Huai Y, Albert F, Nguyen P, Pakala M and Valet T 2004 *Appl. Phys. Lett.* **84** 3118
[20] Diao Z *et al* 2005 *Appl. Phys. Lett.* **87** 232502
[21] Amiri P *et al* 2011 *Electron Device Lett. IEEE* **32** 57
[22] Kiselev S I *et al* 2003 *Nature* **425** 380
[23] Houssameddine D *et al* 2007 *Nature Mater* **6** 447
[24] Deac A M *et al* 2008 *Nature Phys.* **4** 803
[25] Rippard W H, Pufall M R, Kaka S, Russek S E and Silva T J 2004 *Phys. Rev. Lett.* **92** 027201
[26] Rippard W H *et al* 2010 *Phys. Rev.* B **81** 014426
[27] Kaka S *et al* 2005 *Nature* **437** 389
[28] Braganca P M *et al* 2010 *Nanotechnology* **21** 235202
[29] Moore G 1965 *Electronics* **38** 114–7
[30] http://www.itrs.net/
[31] Bandyopadhyay S and Cahay M 2009 *Nanotechnology* **20** 412001
[32] Nikonov D and Bourianoff G 2008 *J. Supercond. Novel Magn.* **21** 479
[33] Black W and Das B 2000 *J. Appl. Phys.* **87** 6674
[34] Richter R *et al* 2002 *Solid States Electron.* **46** 639
[35] Ney A, Pampuch C, Koch R and Ploog K H 2003 *Nature* **425** 485
[36] Meng H, Wang J and Wang J 2005 *IEEE Electron Device Lett.* **26** 360
[37] Wang J, Meng H and Wang J 2005 *J. Appl. Phys.* **97** 10D509
[38] Lee S *et al* 2007 *IEEE Trans. Magn.* **43** 2677
[39] Hóink V, Lau J W and Egelhoff W F 2010 *Appl. Phys. Lett.* **96** 142508
[40] Datta S and Das B 1990 *Appl. Phys. Lett.* **56** 665
[41] Schliemann J, Egues J C and Loss D 2003 *Phys. Rev. Lett.* **90** 146801
[42] Cartoixà X, Ting D Z-Y and Chang Y 2003 *Appl. Phys. Lett.* **83** 1462
[43] Sugahara S and Tanaka M 2004 *Appl. Phys. Lett.* **84** 2307
[44] Bandyopadhyay S 2005 *Superlatt. Microstruct.* **37** 77
[45] Flatte M E, Yu Z G, Johnston-Halperin E and Awschalom D D 2003 *Appl. Phys. Lett.* **82** 4740
[46] Fabian J, Zutic I and Sarma S D 2004 *Appl. Phys. Lett.* **84** 85
[47] Kumar S B, Tan S G, Jalil M B A, Cheung P Q and Jiang Y 2008 *J. Appl. Phys.* **103** 054310
[48] Allwood D *et al* 2005 *Science* **309** 1688
[49] Cowburn R and Welland M 2000 *Science* **287** 1466
[50] Bryan M T, Atkinson D and Cowburn R P 2004 *Appl. Phys. Lett.* **85** 3510
[51] Lau J W, McMichael R, Schofield M A and Zhu Y 2007 *J. Appl. Phys.* **102** 023916
[52] Thomson T, Hu G and Terris B D 2006 *Phys. Rev. Lett.* **96** 257204
[53] Shaw J M, Rippard W H, Russek S E, Reith T and Falco C M 2007 *J. Appl. Phys.* **101** 023909
[54] Lau J W *et al* 2008 *Appl. Phys. Lett.* **92** 012506
[55] Lau J W *et al* 2010 *Appl. Phys. Lett.* **96** 262508
[56] Shaw J *et al* 2010 *Phys. Rev.* B **82** 144437
[57] Sharrock M P and McKinney J T 1981 *IEEE Trans. Magn.* **17** 3020
[58] Néel L 1949 *Ann. Geophys.* **5** 99
[59] Woodward R C, Lance A M, Street R and Stamps R L 2003 *J. Appl. Phys.* **93** 6567
[60] Lau J W, Bording J K, Beleggia M and Zhu Y 2006 *Appl. Phys. Lett.* **88** 012508
[61] Lau J W, McMichael R, Beleggia M and Zhu Y 2007 *J. Appl. Phys.* **102** 043906
[62] Terris B D and Thomson T 2005 *J. Phys. D: Appl. Phys.* **38** R199
[63] Terris B D 2009 *J. Magn. Magn. Mater.* **321** 512
[64] Lodder J C 2004 *J. Magn. Magn. Mater.* **272–276** 1692
[65] Ross C 2001 *Ann. Rev. Mater. Res.* **31** 203

[66] Martín J I, Nogués J, Liu K, Vicent J L and Schuller I K 2003 *J. Magn. Magn. Mater.* **256** 449
[67] Ross C A *et al* 2002 *Phys. Rev.* B **65** 144417
[68] Shaw J M *et al* 2008 *Phys. Rev.* B **78** 024414
[69] Hyndman R *et al* 2001 *J. Appl. Phys.* **90** 3843
[70] Rettner C T, Anders S, Baglin J E E, Thomson T and Terris B D 2002 *Appl. Phys. Lett.* **80** 279
[71] Parekh V *et al* 2007 *J. Appl. Phys.* **101** 083904
[72] Fontana R E Jr and Zolla H G 2006 Method and apparatus for oxidizing conductive redeposition in TMR sensors *Patent* 7148072
[73] Moritz J *et al* 2002 *IEEE Trans. Magn.* **38** 1731
[74] Hellwig O *et al* 2008 *Appl. Phys. Lett.* **93** 192501
[75] Hellwig O *et al* 2009 *Appl. Phys. Lett.* **95** 232505
[76] Persson A, Riddar F, Nguyen H, Ericson F and Thornell G 2011 *IEEE Trans. Magn.* **47** 151
[77] Fassbender J and McCord J 2008 *J. Magn. Magn. Mater.* **320** 579
[78] Chappert C *et al* 1998 *Science* **280** 1919
[79] Stanescu D *et al* 2008 *J. Appl. Phys.* **103** 07B529
[80] Fassbender J *et al* 2006 *Phys. Rev.* B **73** 184410
[81] French R H and Tran H V 2009 *Ann. Rev. Mater. Res.* **39** 93
[82] Lu C and Lipson R 2009 *Laser Photon. Rev.* **4** 568
[83] Zhu M and McMichael R D 2010 *J. Appl. Phys.* **107** 103908
[84] Pardavi-Horvath M *et al* 2008 *J. Appl. Phys.* **103** 07D516
[85] Savas T A, Farhoud M, Smith H I, Hwang M and Ross C A 1999 *J. Appl. Phys.* **85** 6160
[86] Hamley I W 2003 *Nanotechnology* **14** R39
[87] Sachan M *et al* 2008 *J. Phys. D: Appl. Phys.* **41** 134001
[88] Hogg C, Majetich S and Bain J 2010 *IEEE Trans. Magn.* **46** 2307
[89] Hellwig O *et al* 2010 *Appl. Phys. Lett.* **96** 052511
[90] Cheng J Y, Mayes A M and Ross C A 2004 *Nature Mater.* **3** 823
[91] Ruiz R *et al* 2008 *Science* **321** 936
[92] Foner S 1959 *Rev. Sci. Instrum.* **30** 548
[93] Graham C D 2000 *J. Mater. Sci. Technol.* **16** 97–101
[94] Fagaly R L 2006 *Rev. Sci. Instrum.* **77** 101101
[95] Zijlstra H 1970 *Rev. Sci. Instrum.* **41** 1241
[96] Flanders P J 1988 *J. Appl. Phys.* **63** 3940
[97] Cleuziou J, Wernsdorfer W, Bouchiat V, Ondarcuhu T and Monthioux M 2006 *Nature Nanotechnol.* **1** 53
[98] Troeman A *et al* 2007 *Nano Lett.* **7** 2152
[99] Finkler A *et al* 2010 *Nano Lett.* **10** 1046
[100] Chatraphom S, Fleet E F and Wellstood F C 2000 *Appl. Phys. Lett.* **76** 2304
[101] Ebert H 1996 *Rep. Prog. Phys.* **59** 1665
[102] Qiu Z Q and Bader S D 2000 *Rev. Sci. Instrum.* **71** 1243
[103] Berger A and Pufall M R 1997 *Appl. Phys. Lett.* **71** 965
[104] Schneider M L *et al* 2007 *J. Appl. Phys.* **102** 103909
[105] Grimsditch M and Vavassori P 2004 *J. Phys.: Conden. Matter* **16** R275
[106] Hall E H 1879 *Am. J. Math.* **2** 287
[107] Smith A W 1910 *Phys. Rev.* **30** 1
[108] Pugh E M, Rostoker N and Schindler A 1950 *Phys. Rev.* **80** 688
[109] Karplus R and Luttinger J M 1954 *Phys. Rev.* **95** 1154
[110] Smit J 1955 *Physica* **21** 877
[111] Berger L 1970 *Phys. Rev.* B **2** 4559
[112] Gerber A *et al* 2004 *Phys. Rev.* B **69** 134422
[113] Onoda S, Sugimoto N and Nagaosa N 2006 *Phys. Rev. Lett.* **97** 126602
[114] Pugh E M and Rostoker N 1953 *Rev. Mod. Phys.* **25** 151
[115] Smit J 1958 *Physica* **24** 39
[116] Sangiao S *et al* 2009 *Phys. Rev.* B **79** 014431
[117] Tian Y, Ye L and Jin X 2009 *Phys. Rev. Lett.* **103** 087206
[118] Rosenblatt D, Karpovski M and Gerber A 2010 *Appl. Phys. Lett.* **96** 022512
[119] Luttinger J M 1958 *Phys. Rev.* **112** 739
[120] Nozières P and Lewiner C 1973 *J. Phys. (Paris)* **34** 15
[121] Gerber A *et al* 2004 *Phys. Rev.* B **69** 224403
[122] Kikuchi N, Okamoto S, Kitakami O, Shimada Y and Fukamichi K 2003 *Appl. Phys. Lett.* **82** 4313
[123] Belmeguenai M, Devolder T, Chappert C and Mathet V 2004 *J. Magn. Magn. Mater.* **272–276** E1657
[124] Alexandrou M *et al* 2010 *J. Appl. Phys.* **108** 043920
[125] Hoffmann H 1964 *J. Appl. Phys.* **35** 1790
[126] Heyderman L J, Chapman J N and Parkin S S P 1994 *J. Magn. Magn. Mater.* **138** 344
[127] Volkov V V, Zhu Y and Malac M 2004 *Phil. Mag.* **84** 2607
[128] Lau J W, Budruk A, Nuhfer N T and Graef M D Image comparison between aberration-corrected and conventional Lorentz microscopy, Unpublished
[129] Lau J W, Schofield M A and Zhu Y 2007 *Ultramicroscopy* **107** 396
[130] Williams D B and Carter C B 2004 *Transmission Electron Microscopy: A Textbook for Materials Science* 1st edn (Berlin: Springer)
[131] Uhlig T, Heumann M and Zweck J 2003 *Ultramicroscopy* **94** 193
[132] Bostanjoglo O, Elschner R, Mao Z, Nink T and Weingärtner M 2000 *Ultramicroscopy* **81** 141
[133] King W E *et al* 2005 *J. Appl. Phys.* **97** 111101
[134] Cowley J M 1969 *Appl. Phys. Lett.* **15** 58
[135] Zeitler E and Thomson M G R 1970 *OPTIK* **31** 258
[136] Zeitler E and Thomson M G R 1970 *OPTIK* **31** 359
[137] Chapman J N and Darlingt E H 1974 *J. Phys. E: Sci. Instrum.* **7** 181
[138] Chapman J N, Batson P E, Waddell E M and Ferrier R P 1978 *Ultramicroscopy* **3** 203
[139] Chapman J N 1984 *J. Phys. D: Appl. Phys.* **17** 623
[140] Sekiguchi T, Watanabe D and Tsuno K 1985 *Japan J. Appl. Phys.* **24** 1229
[141] Dekkers N H and Lang H 1974 *OPTIK* **41** 452
[142] Tsuno K, Inoue M and Ueno K 1989 *Mater. Sci. Eng.* B **3** 403
[143] Kirk K J, McVitie S, Chapman J N and Wilkinson C D W 2001 *J. Appl. Phys.* **89** 7174
[144] Cowley J M 1992 *Ultramicroscopy* **41** 335
[145] Möllenstedt G and Düker H 1956 *Z. Phys.* A **145** 377
[146] Aharonov Y and Bohm D 1959 *Phys. Rev.* **115** 485
[147] McCartney M R and Smith D J 2007 *Ann. Rev. Mater. Res.* **37** 729
[148] Völkl E, Allard L F and Joy D C (ed) 1999 *Introduction to Electron Holography* (Berlin: Springer) chapter 4
[149] Geiger D, Lichte H, Linck M and Lehmann M 2008 *Microsc. Microanal.* **14** (1) 68
[150] Voelkl E and Tang D 2010 *Ultramicroscopy* **110** 447
[151] de Ruijter W and Weiss J 1993 *Ultramicroscopy* **50** 269
[152] Harscher A, Lang G and Lichte H 1995 *Ultramicroscopy* **58** 79
[153] Lichte H, Linck M, Geiger D and Lehmann M 2010 *Microsc. Microanal.* **16** 434
[154] Yamamoto K *et al* 2008 *Appl. Phys. Lett.* **93** 082502
[155] Gao Y, Bao Y, Pakhomov A B, Shindo D and Krishnan K M 2006 *Phys. Rev. Lett.* **96** 137205
[156] Snoeck E *et al* 2008 *Nano Lett.* **8** 4293
[157] Teague M R 1983 *J. Opt. Soc. Am.* **73** 1434
[158] Paganin D and Nugent K A 1998 *Phys. Rev. Lett.* **80** 2586
[159] Beleggia M, Schofield M, Volkov V and Zhu Y 2004 *Ultramicroscopy* **102** 37
[160] Twitchett A C, Dunin-Borkowski R E and Midgley P A 2006 *Phil. Mag.* **86** 5805
[161] Latychevskaia T, Formanek P, Koch C and Lubk A 2010 *Ultramicroscopy* **110** 472
[162] Schattschneider P *et al* 2006 *Nature* **441** 486
[163] Schattschneider P, Ennen I, Löffler S, Stöger-Pollach M and Verbeeck J 2010 *J. Appl. Phys.* **107** 09D311
[164] Chrobok G and Hofmann M 1976 *Phys. Lett.* A **57** 257

[165] Unguris J *et al* 1982 *Phys. Rev. Lett.* **49** 1047
[166] Koike K and Hayakawa K 1984 *Japan. J. Appl. Phys.* **23** L187
[167] Mott N F 1929 *Proc. R. Soc. Lond.* A **124** 425
[168] Kessler J 1985 *Polarized Electrons* (Berlin: Springer)
[169] Chung S, McMichael R, Pierce D and Unguris J 2010 *Phys. Rev.* B **81** 024410
[170] Bauer E 2001 *AIP Conf. Proc.* **570** 965
[171] Bauer E 1994 *Rep. Prog. Phys.* **57** 895
[172] Klein C, Ramchal R, Farle M and Schmid A K 2006 *Surf. Interface Anal.* **38** 1550
[173] Duden T and Bauer E 1998 *J. Electron Microsc.* **47** 379
[174] Sander D 2004 *J. Phys.: Conden. Matter* **16** R603
[175] Funk T, Deb A, George S, Wang H and Cramer S 2005 *Coord. Chem. Rev.* **249** 3
[176] Vogel J *et al* 2003 *Appl. Phys. Lett.* **82** 2299
[177] Kuksov A 2004 *J. Appl. Phys.* **95** 6530
[178] Kaiser A, Wiemann C, Cramm S and Schneider C M 2009 *J. Phys.: Conden. Matter* **21** 314008
[179] Yacoot A and Koenders L 2008 *J. Phys. D: Appl. Phys.* **41** 103001
[180] Hopkins P F, Moreland J, Malhotra S S and Liou S H 1996 *J. Appl. Phys.* **79** 6448
[181] Liou S H, Malhotra S S, Moreland J and Hopkins P F 1997 *Appl. Phys. Lett.* **70** 135
[182] Hartmann U 1999 *Ann. Rev. Mater. Sci.* **29** 53
[183] Skidmore G D and Dahlberg E D 1997 *Appl. Phys. Lett.* **71** 3293
[184] Chen I *et al* 2008 *Nanotechnology* **19** 075501
[185] Rippard W H and Buhrman R A 1999 *Appl. Phys. Lett.* **75** 1001
[186] Rippard W H and Buhrman R A 2000 *Phys. Rev. Lett.* **84** 971
[187] Rippard W H *et al* 2000 *Appl. Phys. Lett.* **77** 1357
[188] Polder D 1949 *Phil. Mag.* **40** 99
[189] Craik D J 1975 *Magnetic Oxides* vol 2 (London: Wiley) chapter 10
[190] Heinrich B, Cochran J F and Hasegawa R 1985 *J. Appl. Phys.* **57** 3690
[191] Celinski Z and Heinrich B 1991 *J. Appl. Phys.* **70** 5935
[192] McMichael R D, Twisselmann D J and Kunz A 2003 *Phys. Rev. Lett.* **90** 227601
[193] Schloemann E 1992 *IEEE Trans. Magn.* **28** 3300
[194] McMichael R D and Krivosik P 2004 *IEEE Trans. Magn.* **40** 2
[195] Shaw J M, Geiss R and Russek S 2006 *Appl. Phys. Lett.* **89** 212503
[196] Hurben M J and Patton C E 1998 *J. Appl. Phys.* **83** 4344
[197] McMichael R D, Stiles M D, Chen P J and Egelhoff W F 1998 *Phys. Rev.* B **58** 8605
[198] Arias R and Mills D L 1999 *Phys. Rev.* B **60** 7395
[199] Rezende S M, Azevedo A, Lucena M A and de Aguiar F M 2001 *Phys. Rev.* B **63** 214418
[200] Sparks M, Loudon R and Kittel C 1961 *Phys. Rev.* **122** 791
[201] Dobin A Y and Victora R H 2003 *Phys. Rev. Lett.* **90** 167203
[202] Gurevich A G and Melkov G A 1996 *Magnetization Oscillations and Waves* 1 edn (Boca Raton, FL: CRC-Press)
[203] McMichael R D and Stiles M D 2005 *J. Appl. Phys.* **97** 10J901
[204] Gerardin O, Gall H L, Donahue M J and Vukadinovic N 2001 *J. Appl. Phys.* **89** 7012
[205] Grimsditch M, Leaf G K, Kaper H G, Karpeev D A and Camley R E 2004 *Phys. Rev.* B **69** 174428
[206] Grimsditch M *et al* 2004 *Phys. Rev.* B **70** 054409
[207] Jung S, Ketterson J B and Chandrasekhar V 2002 *Phys. Rev.* B **66** 132405
[208] Shaw J M, Silva T J, Schneider M L and McMichael R D 2009 *Phys. Rev.* B **79** 184404
[209] Griffiths J H E 1946 *Nature* **158** 670
[210] Pechan M J *et al* 2006 *J. Appl. Phys.* **99** 08C702
[211] Maranville B B *et al* 2006 *J. Appl. Phys.* **99** 08C703
[212] McMichael R D, Ross C A and Chuang V P 2008 *J. Appl. Phys.* **103** 07C505
[213] Maranville B B, McMichael R D and Abraham D W 2007 *Appl. Phys. Lett.* **90** 232504
[214] Neudecker I *et al* 2006 *J. Magn. Magn. Mater.* **307** 148
[215] Kalarickal S S *et al* 2006 *J. Appl. Phys.* **99** 093909
[216] Buchanan K S *et al* 2006 *J. Appl. Phys.* **99** 08C707
[217] Buchanan K S, Grimsditch M, Fradin F Y, Bader S D and Novosad V 2007 *Phys. Rev. Lett.* **99** 267201
[218] Neudecker I *et al* 2006 *Phys. Rev.* B **73** 134426
[219] Keatley P S *et al* 2008 *Phys. Rev.* B **78** 214412
[220] Barman A *et al* 2006 *Nano Lett.* **6** 2939
[221] van Kampen M *et al* 2002 *Phys. Rev. Lett.* **88** 227201
[222] Freeman M R, Brady M J and Smyth J 1992 *Appl. Phys. Lett.* **60** 2555
[223] Wang D *et al* 2005 *IEEE Trans. Nanotechnol.* **4** 460
[224] Liu Z G, Sydora R D and Freeman M R 2008 *Phys. Rev.* B **77** 174410
[225] Park J P, Eames P, Engebretson D M, Berezovsky J and Crowell P A 2002 *Phys. Rev. Lett.* **89** 277201
[226] Beaurepaire E, Merle J, Daunois A and Bigot J 1996 *Phys. Rev. Lett.* **76** 4250
[227] Barman A *et al* 2007 *Appl. Phys. Lett.* **90** 202504
[228] Qureshi N *et al* 2005 *Nano Lett.* **5** 1413
[229] Wang S *et al* 2007 *Appl. Phys. Lett.* **90** 252504
[230] Compton R L and Crowell P A 2006 *Phys. Rev. Lett.* **97** 137202
[231] Koopmans B *et al* 2010 *Nature Mater.* **9** 259
[232] Hohlfeld J *et al* 2001 *Phys. Rev.* B **65** 012413
[233] Johnson W L, Kim S A, Russek S E and Kabos P 2005 *Appl. Phys. Lett.* **86** 102507
[234] Carlotti G and Gubbiotti G 2002 *J. Phys.: Condens. Matter* **14** 8199
[235] Sandercock J R 1982 *Light Scattering in Solids* vol 3 ed M Cardona and G Guntherodt (Berlin: Springer) p 173
[236] Hillebrands B 2000 *Light Scattering* ed M Cardona and Guntherodt (Berlin: Springer) pp 174–269
[237] Gubbiotti G, Madami M, Tacchi S, Carlotti G and Okuno T 2006 *J. Appl. Phys.* **99** 08C701
[238] Giovannini L *et al* 2004 *Phys. Rev.* B **70** 172404
[239] Grimsditch M *et al* 2006 *Phys. Rev. Lett.* **96** 047401
[240] Lin C S *et al* 2010 *J. Appl. Phys.* **108** 114305
[241] Nembach H T *et al* 2011 *Phys. Rev.* B **83** 094427
[242] Schultheiss H *et al* 2008 *Phys. Rev. Lett.* **100** 047204
[243] Demidov V E *et al* 2010 *Phys. Rev. Lett.* **104** 217203
[244] Gubbiotti G *et al* 2009 *J. Appl. Phys.* **105** 07D521
[245] Jersch J *et al* 2010 *Appl. Phys. Lett.* **97** 152502
[246] Kubota H *et al* 2008 *Nature Phys.* **4** 37
[247] Sankey J C *et al* 2006 *Phys. Rev. Lett.* **96** 227601
[248] Fuchs G *et al* 2007 *Appl. Phys. Lett.* **91** 062507
[249] Wang C *et al* 2009 *Phys. Rev.* B **79** 224416
[250] Mewes T *et al* 2006 *Phys. Rev.* B **74** 144424
[251] Obukhov Y *et al* 2008 *Phys. Rev. Lett.* **100** 197601
[252] Klein O *et al* 2008 *Phys. Rev.* B **78** 144410
[253] Degen C L, Poggio M, Mamin H J, Rettner C T and Rugar D 2009 *Proc. Natl Acad. Sci.* **106** 1313
[254] Imtiaz A and Anlage S M 2006 *J. Appl. Phys.* **100** 044304
[255] An T, Ohnishi N, Eguchi T, Hasegawa Y and Kabos P 2010 *IEEE Magn. Lett.* **1** 3500104
[256] Keavney D J, Cheng X M and Buchanan K S 2009 *Appl. Phys. Lett.* **94** 172506
[257] Acremann Y *et al* 2006 *Phys. Rev. Lett.* **96** 217202
[258] Bryan M T, Fry P W, Fischer P J and Allwood D A 2008 *J. Appl. Phys.* **103** 07D909
[259] Uhlírcaron V *et al* 2010 *Phys. Rev.* B **81** 224418
[260] Moore T *et al* 2010 *J. Magn. Magn. Mater.* **322** 1347
[261] Stamm C *et al* 2007 *Nature Mater.* **6** 740
[262] Carva K, Legut D and Oppeneer P M 2009 *Europhys. Lett.* **86** 57002

[263] Schoenlein R W *et al* 2000 *Science* **287** 2237
[264] Gutt C *et al* 2009 *Phys. Rev.* B **79** 212406
[265] Schlotter W F *et al* 2007 *Opt. Lett.* **32** 3110
[266] Berlasso R *et al* 2006 *Phys. Rev.* B **73** 115101
[267] La-O-Vorakiat C *et al* 2009 *Phys. Rev. Lett.* **103** 257402
[268] Eisebitt S, Lörgen M, Eberhardt W, Lüning J and Stöhr J 2005 *Appl. Phys.* A **80** 921
[269] Murnane M M and Miao J 2009 *Nature* **460** 1088
[270] Berkowitz A and Meiklejohn W 1975 *IEEE Trans. Magn.* **11** 996
[271] Victora R H 1989 *Phys. Rev. Lett.* **63** 457
[272] Heindl R, Rippard W H, Russek S E, Pufall M R and Kos A B 2011 *J. Appl. Phys.* **109** 073910
[273] Heindl R, Rippard W H, Russek S E and Kos A B 2011 *Phys. Rev.* B **83** 054430
[274] Bauer M, Fassbender J, Hillebrands B and Stamps R L 2000 *Phys. Rev.* B **61** 3410
[275] Kaka S and Russek S E 2002 *Appl. Phys. Lett.* **80** 2958
[276] Hillebrands B and Ounadjela K (ed) 2003 High speed switching and rotational dynamics in small magnetic thin film devices *Spin Dynamics in Confined Magnetic Structures* vol II (Berlin: Springer) pp 93–154
[277] Gerrits T, van den Berg H A M, Hohlfeld J, Bar L and Rasing T 2002 *Nature* **418** 509
[278] Rave W and Hubert A 2000 *IEEE Trans. Magn.* **36** 3886
[279] Brown W F 1959 *J. Phys. Radium* **20** 4
[280] Lederman M, O'Barr R and Schultz S 1995 *IEEE Trans. Magn.* **31** 3793
[281] Zhu J, Zheng Y and Prinz G A 2000 *J. Appl. Phys.* **87** 6668
[282] Beleggia M *et al* 2006 *J. Magn. Magn. Mater.* **301** 131
[283] Taniuchi T, Oshima M, Akinaga H and Ono K 2005 *J. Appl. Phys.* **97** 10J904
[284] Mironov V *et al* 2007 *J. Magn. Magn. Mater.* **312** 153
[285] Jain S, Ren Y, Adeyeye A O and Singh N 2009 *Phys. Rev.* B **80** 132401
[286] Waeyenberge B V *et al* 2006 *Nature* **444** 461
[287] Hertel R, Gliga S, Fähnle M and Schneider C M 2007 *Phys. Rev. Lett.* **98** 117201
[288] Yamada K, Kasai S, Nakatani Y, Kobayashi K and Ono T 2008 *Appl. Phys. Lett.* **93** 152502
[289] Heindl R *et al* 2008 *Appl. Phys. Lett.* **92** 262504
[290] Korsten M 1943 *Grundlagen einer theorie der ferromagnetischen hysterese und der koorzitivkraft* S. Hirzel
[291] Fidler J and Kronmüller H 1979 *Phys. Status Solidi* A **56** 545
[292] Durst K and Kronmüller H 1987 *J. Magn. Magn. Mater.* **68** 63
[293] Kirk K J *et al* 2001 *J. Phys. D: Appl. Phys.* **34** 160
[294] Stoner E C and Wohlfarth E P 1948 *Phil. Trans. R. Soc. Lond.* A **240** 599
[295] Sharrock M P 1994 *J. Appl. Phys.* **76** 6413
[296] Sharrock M P 1999 *IEEE Trans. Magn.* **35** 4414
[297] Bean C P and Livingston J D 1959 *J. Appl. Phys.* **30** S120
[298] Chikazumi S 1997 *Physics of Ferromagnetism* (Oxford: Oxford University Press)
[299] Kneller E and Hawig R 1991 *IEEE Trans. Magn.* **27** 3588
[300] Fullerton E E, Jiang J S, Grimsditch M, Sowers C H and Bader S D 1998 *Phys. Rev.* B **58** 12193
[301] Thiele J, Maat S and Fullerton E E 2003 *Appl. Phys. Lett.* **82** 2859
[302] Suess D 2006 *Appl. Phys. Lett.* **89** 113105
[303] Ruigrok J J M, Coehoorn R, Cumpson S R and Kesteren H W 2000 *J. Appl. Phys.* **87** 5398
[304] Richter H J 2009 *J. Magn. Magn. Mater.* **321** 467
[305] Fassbender J *et al* 2009 *New J. Phys.* **11** 125002
[306] Ozatay O *et al* 2008 *Nature Mater.* **7** 567
[307] Schrag B D *et al* 2000 *Appl. Phys. Lett.* **77** 2373
[308] Dittrich R *et al* 2005 *J. Appl. Phys.* **97** 10J705
[309] Shaw J M *et al* 2009 *Phys. Rev.* B **80** 184419
[310] Engel B N, England C D, Vanleeuwen R A, Wiedmann M H and Falco C M 1991 *Phys. Rev. Lett.* **67** 1910
[311] Naik V M *et al* 1998 *J. Appl. Phys.* **84** 3273
[312] Sbiaa R *et al* 2009 *J. Appl. Phys.* **106** 023906
[313] Kubo T *et al* 2006 *J. Appl. Phys.* **99** 08G911
[314] Hinata S, Yanagisawa R, Saito S and Takahashi M 2009 *J. Appl. Phys.* **105** 07B718
[315] Yuan H and Laughlin D E 2009 *IEEE Trans. Magn.* **45** 3569
[316] Takahashi Y, Tanahashi K and Hosoe Y 2002 *J. Appl. Phys.* **91** 8022
[317] Shaw J M, Nembach H T and Silva T J 2010 *J. Appl. Phys.* **108** 093922
[318] Abraham M C *et al* 2001 *J. Appl. Phys.* **89** 5667
[319] Jang H, Eames P, Dahlberg E D, Farhoud M and Ross C A 2005 *Appl. Phys. Lett.* **86** 023102
[320] Belle B D *et al* 2008 *IEEE Trans. Magn.* **44** 3468
[321] Smith D T *et al* 2009 *IEEE Trans. Magn.* **45** 3554
[322] Aharoni A 1998 *J. Appl. Phys.* **83** 3432
[323] Chunsheng E, Parekh V, Ruchhoeft P, Khizroev S and Litvinov D 2008 *J. Appl. Phys.* **103** 063904
[324] Hellwig O *et al* 2007 *Appl. Phys. Lett.* **90** 162516
[325] Krone P, Makarov D, Schrefl T and Albrecht M 2009 *J. Appl. Phys.* **106** 103913
[326] Hauet T *et al* 2009 *Appl. Phys. Lett.* **95** 262504
[327] Mangin S *et al* 2006 *Nature Mater.* **5** 210
[328] Xiao J, Zangwill A and Stiles M D 2004 *Phys. Rev.* B **70** 172405
[329] Kent A, Ozyilmaz B and del Barco E 2004 *Appl. Phys. Lett.* **84** 3897
[330] Seki T, Mitani S, Yakushiji K and Takanashi K 2006 *Appl. Phys. Lett.* **89** 172504
[331] Huai Y, Pakala M, Diao Z and Ding Y 2005 *IEEE Trans. Magn.* **41** 2621
[332] Meng H, Wang J and Wang J 2006 *Appl. Phys. Lett.* **88** 082504
[333] Ristoiu D *et al* 2000 *Europhys. Lett.* **49** 624
[334] Raphael M *et al* 2002 *Phys. Rev.* B **66** 104429
[335] Miura Y, Nagao K and Shirai M 2004 *Phys. Rev.* B **69** 144413
[336] Kammerer S, Thomas A, Hutten A and Reiss G 2004 *Appl. Phys. Lett.* **85** 79
[337] Sakuraba Y *et al* 2005 *Japan. J. Appl. Phys.* **44** L1100
[338] Tezuka N, Ikeda N, Sugimoto S and Inomata K 2006 *Appl. Phys. Lett.* **89** 252508
[339] Marukame T *et al* 2007 *Appl. Phys. Lett.* **90** 012508
[340] Shan R *et al* 2009 *Phys. Rev. Lett.* **102** 246601
[341] Law R, Tan E, Sbiaa R, Liew T and Chong T 2009 *Appl. Phys. Lett.* **94** 062516
[342] Diao Z *et al* 2007 *Appl. Phys. Lett.* **90** 132508
[343] Tserkovnyak Y, Brataas A and Bauer G E W 2003 *Phys. Rev.* B **67** 140404
[344] Nagasaka N *et al* 2006 *Fujitsu Sci. Tech. J.* **42** 149
[345] Maat S, Carey M J and Childress J R 2007 *J. Appl. Phys.* **101** 093905
[346] Katada H, Nakamoto K, Hoshiya H, Hoshino K and Yoshida N 2006 *IEEE Trans. Magn.* **42** 2450
[347] Nakamoto K *et al* 2008 *IEEE Trans. Magn.* **44** 95
[348] Shiimoto M, Katada H, Nakamoto K, Hoshiya H and Das S 2008 *IEEE Trans. Magn.* **44** 3605
[349] Kodama K *et al* 2009 *J. Appl. Phys.* **105** 07E905
[350] Bailey W, Kabos P, Mancoff F and Russek S 2001 *IEEE Trans. Magn.* **37** 1749
[351] Reidy S G, Cheng L and Bailey W E 2003 *Appl. Phys. Lett.* **82** 1254
[352] Maat S, Smith N, Carey M J and Childress J R 2008 *Appl. Phys. Lett.* **93** 103506
[353] Childress J *et al* 2006 *IEEE Trans. Magn.* **42** 2444
[354] Smith N, Maat S, Carey M J and Childress J R 2008 *Phys. Rev. Lett.* **101** 247205